Detection of Single-Molecule Optical Absorption at Room Temperature and Mechanistic Study of Transcriptional Bursting

Detection of Single-Molecule Optical Absorption at Room Temperature and Mechanistic Study of Transcriptional Bursting

A dissertation presented

by

Shasha Chong

to

The Department of Chemistry and Chemical Biology

in partial fulfillment of the requirements

for the degree of

Doctor of Philosophy

in the subject of

Chemistry

Harvard University

Cambridge, Massachusetts

April 2014

Dissertation Advisor: Professor Xiaoliang Sunney Xie Shasha Chong

Detection of Single-Molecule Optical Absorption at Room Temperature and Mechanistic Study of Transcriptional Bursting

Abstract

Advances in optical imaging techniques have allowed quantitative studies of many biological systems. This dissertation elaborates on our efforts in both developing novel imaging modalities based on detection of optical absorption and applying high-sensitivity fluorescence microscopy to the study of biology.

Although fluorescence is the most widely used optical contrast mechanism in biological studies because of its background-free detection, many intracellular molecules are intrinsically non-fluorescent and difficult to label without disturbing their natural functions. Therefore, label-free imaging methods based on contrast mechanisms other than fluorescence are highly desirable. In the first part of this dissertation, we explore new methods for sensitive detection of optical absorption. Chapter 2 describes stimulated emission microscopy and two-photon excited photothermal microscopy. We demonstrate label-free imaging of non-fluorescent biological chromophores with high sensitivity and three-dimensional optical sectioning capability. In Chapter 3, we introduce ground-state depletion microscopy and demonstrate room-temperature detection of the absorption signal from a single molecule. This measurement represents the ultimate detection sensitivity of nonlinear optical spectroscopy at room temperature.

In the second part of my thesis, I focus on transcription of DNA. Transcription is the first step in gene expression and essential for all cell functions. Recent experiments have shown that

transcription of highly expressed genes occurs in stochastic bursts. But the origin of such ubiquitous phenomenon was unknown. We investigate the mechanism in bacteria through a series of *in vitro* and live-cell experiments based on high-sensitivity fluorescence microscopy. Chapter 4 describes a novel high-throughput *in vitro* single-molecule assay to follow real-time transcription on individual DNA templates. Using this assay, we show in Chapter 5 that positive supercoiling buildup on a DNA segment by transcription slows down transcription elongation and eventually stops transcription initiation. Transcription can be resumed upon gyrase binding to the DNA segment. Furthermore, using single-cell mRNA counting fluorescence *in situ* hybridization (FISH) assay, we find the extent of transcriptional bursting depends on the intracellular gyrase concentration. Together, these findings prove that transcriptional bursting of highly expressed genes in bacteria is primarily caused by reversible gyrase dissociation from and rebinding to a DNA segment, changing the supercoiling level of the segment.

Contents

Acknowledgements

I would like to express my deepest gratitude to my advisor, Professor Sunney Xie, for his insightful guidance, encouragement, patience, and providing me with an excellent atmosphere for doing research. Sunney is a very courageous researcher. I truly admire his incredible drive to new science and painstaking efforts to make the impossible possible. I feel lucky to have such a passionate scientist as my advisor in graduate school.

I am deeply grateful to my graduate committee members, Professors Charles Lieber and Xiaowei Zhuang for giving me not only critical and constructive comments on my research projects, but also precious advice on the method and attitude to conduct research in general.

Before joining the Xie Group, the bulk of my research experience was in computational chemistry, and I had a lot to learn about conducting experiments. I am indebted to many group members who have long since patiently taught me, including Drs. Wei Min, Gary Holtom, Sangjin Kim, Sijia Lu, Brian Saar, Christian Freudiger and Erik Bröströmer.

My contributions to the label-free imaging of biological chromophores described in Chapter 2 were made under Wei, Sijia and Gary's mentorship, who started the project and taught me how to build lasers and microscopes. Wei continued to work closely with me on the detection of room-temperature single-molecule optical absorption described in Chapter 3, and kept providing me with valuable advice even after moving to New York. I also thank Drs. Maarten Roeffaers, Peter Sims and Peijun Cong for helpful discussions on these projects.

It was Sangjin and Erik who introduced me to *in vitro* single-molecule assays based on fluorescence imaging. As an expert in single-molecule biophysics, Sangjin shared with me priceless experience in experimental design and troubleshooting. Our discussions continued after she moved to Connecticut.

The mechanistic study of transcriptional bursting was done in close collaboration with Chongyi Chen, another graduate student in the Xie Group from the MCB program. Chongyi is a talented biologist and great team worker. In the development of the *in vitro* single-molecule transcription assay described in Chapter 4, I benefited tremendously not only from our daily discussions, but also his making DNA templates for transcription and conducting ensemble controls for RNA polymerase activities. In the investigation of the mechanism of transcriptional bursting described in Chapter 5, Chongyi conducted all the live-cell experiments. Along the way, we were lucky to have Professor Hao Ge, a talented mathematician from Peking University in China, join us and build a model to enable quantitative descriptions of transcriptional bursting based on the live-cell data, which made our story complete. I thank Drs. Rahul Roy, Minbiao Ji, Christof Gebhardt, Katsuyuki Shiroguchi, Steve Mao, Chenghang Zong, Long Cai, Gene-Wei Li, and Paul Choi for helpful discussions on this project. I also appreciate Dr. Lin Song for maintaining our labs so well. Nothing was possible without her considerate and diligent work.

I would like to thank Professors Xiaowei Zhuang and Charles Lieber for allowing me to use instruments in their labs, Jiang He, Eileen Sun, Bryan Harada and Dr. Ruobo Zhou in the Zhuang Group and Drs. Jinlin Huang, Ping Xie, Kathleen Ledyard and Xiaojie Duan in the Lieber Group for sharing with me materials and providing advice on my experiments from time to time.

There are several people who provided me with support that was not directly related to particular experiments. I could always count on Peter, Brian, Rahul, Katsu, Wei, Christian, Minbiao, Steve, Winston Zhao, Drs. Lingjie Kong, Dan Fu and Frank Lu to hear me out. I also thank Teri Howard, Larry Valles, Tracey Schaal, Drs. Allen Aloise and Kathleen Ledyard for their encouragement and help throughout my years in the graduate school. I should not forget to mention Evans Pierre and Kimsy Maurissant, the security officers of the CCB department, who

kindly provided walking escorts to me after many of my late night experiments. I'm indebted to many others who have helped me during my study at Harvard, the transportation department, health services, international office, etc. Even though I do not know the names of all the responsible individuals, their contributions should not be neglected.

I am blessed with a very loving family. My parents, Xinling Huang and Daming Chong, have supported me in every possible way unconditionally and unwaveringly. I cannot imagine doing any of this without them. I humbly dedicate this work to them.

Citation to Previously Published Work

Chapter 2 has been previously published with minor changes as the following papers:

Min, Wei*; Lu, Sijia*; Chong, Shasha; Roy, Rahul; Holtom, Gary R.; Xie, X. Sunney "Imaging chromophores with undetectable fluorescence by stimulated emission microscopy" *Nature*, **461**, 1105-1109 (2009).

Lu, Sijia; Min, Wei; Chong, Shasha; Holtom, Gary R.; Xie, X. Sunney "Label-free imaging of heme proteins with two-photon excited photothermal lens microscopy" *Applied Physics Letters*, **96**, 113701 (2010).

Chapter 3 has been previously published with minor changes as the following paper:

Chong, Shasha*; Min, Wei*; Xie, X. Sunney "Ground-State Depletion Microscopy: Detection Sensitivity of Single-Molecule Optical Absorption at Room Temperature" *J. Phys. Chem. Lett*. **1**, 3316-3322 (2010).

Chapter 4 and 5 have been included with minor changes in the following paper:

Chong, Shasha*; Chen, Chongyi*; Ge, Hao; Xie, X. Sunney "Mechanism of Transcriptional Bursting in Bacteria" *Cell* (in press).

*: Equal-contribution authors

Chapter 1

Introduction

1.1 A Technical Introduction

Microscopy is the central technique throughout my dissertation research. I have developed microscopy to detect optical absorption with single-molecule sensitivity, and used fluorescence microscopes to monitor DNA transcription at the single-molecule level. In this introductory chapter, I will provide background on relevant types of microscopy including pump-probe and fluorescence.

1.2 Pump-probe optical microscopy

Pump-probe microscopy is discussed in Chapter 2 and 3 of this dissertation. Pump-probe spectroscopy has been widely employed to study the time-dependent ultrafast phenomena in chemical physics (Fleming, 1986; Yajima et al., 1988). By using the pump pulse to excite the molecule of interest and the subsequent probe pulse to interrogate the transient excited states on a scanning microscope, pump-probe microscopy allows imaging of non-fluorescent chromophores with high sensitivity and specificity.

Figure 1.1 shows a generic excitation and detection scheme of pump-probe microscopy. Normally, pump and probe beams are ultrafast (femtosecond or picosecond) pulsed lasers in order to capture the transient intermediates for non-fluorescent chromophores, though continuous-wave (CW) lasers are sometimes used when the excited state is reasonably long-lived. The pump and probe pulse trains are temporally synchronized (with an adjustable time delay) and spatially combined before collinearly propagate into an inverted microscope. Both

beams are focused to a common focal spot in the sample by a microscope objective. The time delay between the pump pulse and probe pulse is often necessary to allow for dynamic evolution of the transient molecular states.

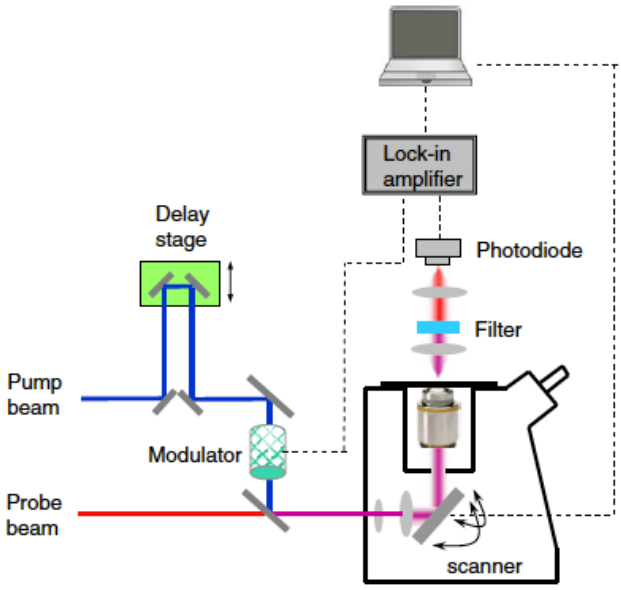

Figure 1.1 Apparatus of pump-probe microscopy.
An optical delay stage is used to control the relative timing between the pump and probe pulses (Wei and Min, 2012).

Before entering the objective, the pump beam intensity is modulated at a frequency *f* higher than 1 MHz by an acoustic or electric optical modulator while the probe beam is not modulated. After passing through the sample, the transmitted probe beam is collected and detected by a photodiode while the pump beam is blocked by a filter. The photodiode signal is demodulated by a lock-in amplifier to extract the modulation depth at the frequency *f* for each pixel. By scanning the combined pump/probe beams or sample stage point-by-point, a 3D image can be constructed.

The high-frequency modulation scheme is a crucial technical element for achieving high detection sensitivity in pump-probe microscopy. Laser intensity noise occurs primarily at low frequencies (from DC to kHz), as shown in Figure 1.2A. As *f* increases to above MHz, the laser intensity noise approaches the quantum shot noise floor, which is always present due to the

stochastic arrival of photons at the photodetector. Thus, the narrowband high-frequency modulation transfer scheme allows shot-noise-limited detection sensitivity by effectively circumventing laser intensity fluctuations and the intensity variation of a transmitted laser beam that is scanned across a heterogeneous sample, both of which occur at low frequencies.

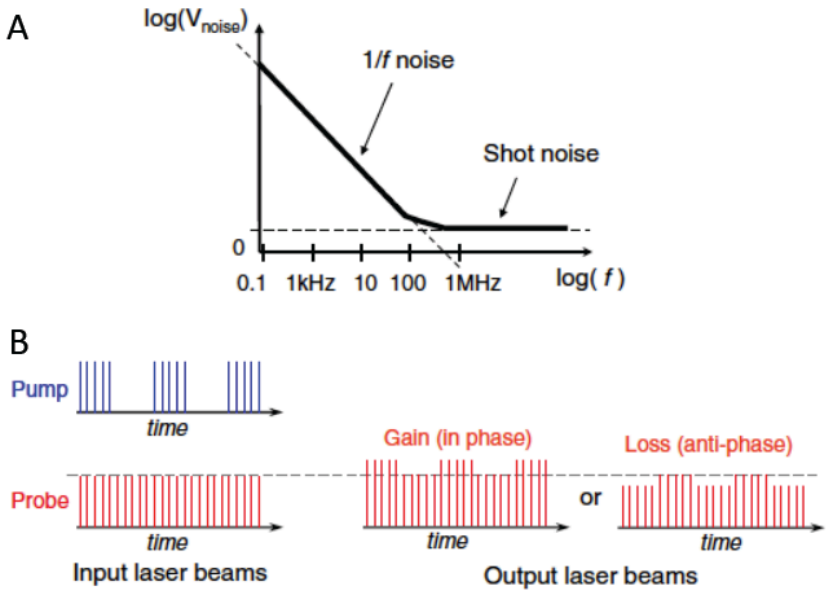

Figure 1.2 Principle of high-frequency modulation scheme.

(A) Noise spectrum (log-log plot) of a typical laser source as a function of frequency *f*. In the low-frequency range (from DC to kHz), the noise is called 1/*f* noise. In the higher-frequency range, the noise approaches the flat floor of shot noise. (B) Temporal modulation behavior of the pump and probe pulse trains before and after interacting with samples (Wei and Min, 2012).

Temporal modulation behaviors of the pulse trains before and after interacting with the sample are illustrated in Figure 1.2B. Depending on the nature of light-molecule interactions, the resulting modulation of probe beam is either in phase or antiphase with the modulation of pump beam. The light-molecule interactions that have been used as the contrast mechanism in pump-probe microscopy include excited state absorption (Fu et al., 2008; Fu et al., 2007a; Fu et al., 2007b), stimulated emission (Min et al., 2009) and ground state depletion (Chong et al., 2010), the latter two are discussed in this dissertation. In addition, the high-frequency phase-sensitive detection scheme has been applied in stimulated Raman scattering (SRS) microscopy (Freudiger

et al., 2008). Photothermal microscopy uses a similar detection scheme as pump-probe microscopy, except that the modulation frequency is lower (~100 kHz in this work), as it takes time for the thermal gradient to build up in the sample after excitation due to a finite thermal conductivity.

1.3 Fluorescence Microscopy

Fluorescence microscopy is used in Chapter 4 and 5 of this dissertation. In principle, fluorescence is background-free, therefore it is often the method of choice when a high sensitivity is required in the applications. Using high quantum efficiency photodetectors, fluorescence microscopy can even detect the very small signal from a single fluorophore. In reality, the sensitivity of fluorescence microscopy may be affected by sources of background including Rayleigh and Raman scattering as well as autofluorescence from the sample and optical components.

Single molecule optical detection at room temperature dates back to 1976 when Hirschfeld reported the use of an optical microscope to reduce probe volume, hence background signal (Hirschfeld, 1976). He was able to detect individual immobilized protein molecules labeled with multiple fluorophores, demonstrating high sensitivity fluorescence measurements. Orrit and Bernard reported the first detection of single fluorophores at cryogenic temperatures in 1990 (Orrit and Bernard, 1990). However, in order for single molecule spectroscopy to be applicable to most problems of chemical or biological interest, the detection of single fluorophores at room temperature was needed.

In 1993, Betzig and Chichester showed that single fluorophores could indeed be imaged a room temperature using near field scanning optical microscopy (Betzig and Chichester, 1993), where laser light is passed through a sub-wavelength aperture. Not only is very low-background,

high-sensitivity fluorescence imaging achieved with this technique at room temperature, but this method also affords super-resolution imaging beyond the classical diffraction limit. Near field single-molecule imaging at room temperature yielded information on the spatial orientation and temporal dynamics of single molecules (Betzig and Chichester, 1993; Xie and Dunn, 1994).

Though a seminal contribution, near-field single molecule imaging had limited applications because of the complexity and perturbation of the near-field probes, and was soon superseded by far-field single molecule imaging. In 1990, Shera et al. demonstrated the far-field detection of single fluorophores in solution at room temperature (Shera et al., 1990). Soon after that, far-field single molecule imaging was demonstrated with total internal reflection (Funatsu et al., 1995) and confocal microscopy (Macklin et al., 1996). These advances gave single molecule fluorescence spectroscopy the potential to be a powerful biophysical tool, particularly for enzymology (Funatsu et al., 1995; Lu et al., 1998; Vale et al., 1996).

Today, high sensitivity fluorescence measurements can be achieved much more easily because of several commercially available products. First, a wide variety of optical filters and dichroics based on thin-film interference coatings are available, the high quality ones are able to reject laser scattering by many orders of magnitude and have spectrally selective throughputs that exceed 95%.

Secondly, high numerical aperture, infinity-corrected objective lenses are commercially available. Numerical apertures of over 1.2 are desirable for high light-collection efficiency and probe volume reduction. An infinity corrected objective is designed to collimate the rays of an image that emerge from its back aperture to infinity such that a second lens (called a tube lens) is required for finite image formation onto a detector. This configuration has great practical convenience, because multiple optical components can be placed in the microscope between the

tube lens and the back aperture of the objective without concern for substantial aberrations.

Third, the use of lasers improves the sensitivity of fluorescence measurements because they not only have very narrow spectra, making it easy to avoid background from scattering, but also they can deliver high power densities to a sample.

Last but the most important element in high-sensitivity fluorescence microscope is high quantum efficiency photodetectors. Avalanche photodiode (APD) and photomultiplier tube (PMT) lack spatial discrimination, which are commonly used detectors in confocal fluorescence microscopes. Both devices employ a photosensitive surface that captures incident photons and generates electronic charges that are sensed and amplified. The current state-of-the-art area photodetector is the electron multiplying charge coupled device or EM-CCD camera, which consists of a dense matrix of photodiodes incorporating charge storage regions. Modern back-illuminated EM-CCD cameras have visible quantum efficiencies that are greater than 90%. Much of the progress in high sensitivity fluorescence imaging and single molecule biophysics is due to EM-CCD camera technology.

Figure 1.3 depicts three fluorescence microscopes used in this dissertation. The epifluorescence microscope depicted in Figure 1.3A would produce wide field illumination at the sample. Typically, an illumination area of tens to hundreds of microns is formed with the laser beam slightly diverging out of the objective. In this configuration, the sample is uniformly illuminated and fluorescence emission is collected through the same objective lens that delivers excitation light. For molecules immobilized on the surface of a coverslip, wide field illumination can be very sensitive. Single fluorescent proteins can be detected in live bacterial cells using a well-equipped wide field fluorescence microscope (Yu et al., 2006), even when a relatively high time resolution is required (Elf et al., 2007). However, high background levels can be

problematic for this imaging modality because the entire sample depth is illuminated.

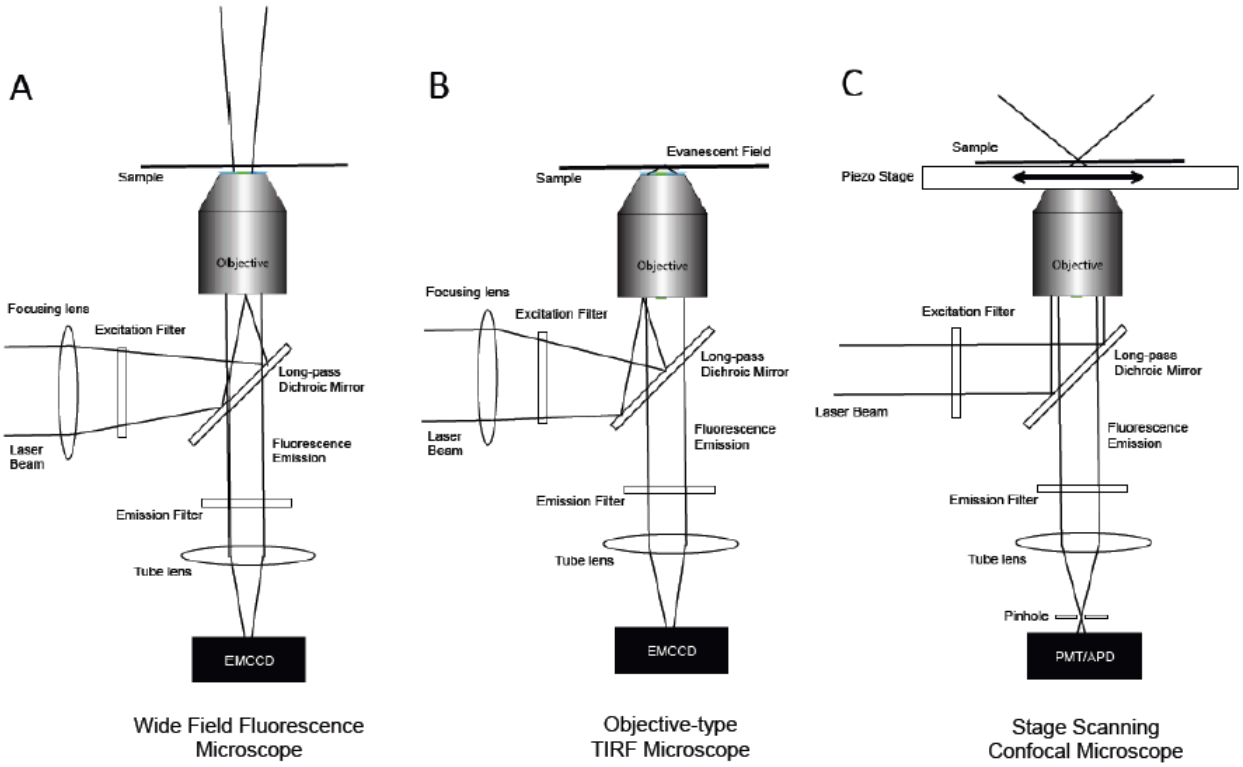

Figure 1.3 Schematic diagrams of fluorescence microscopes.

(A) Epifluorescence, wide field microscope. (B) Objective-type total internal reflection fluorescence (TIRF) microscope. (C) Stage-scanning confocal microscope.

For imaging conducted near the glass-water interface of the sample, total internal reflection fluorescence (TIRF) microscopy can be applied to dramatically reduce the probe volume of an epifluorescence microscope. TIRF imaging can be accomplished with either a prism or a high numerical aperture objective (Funatsu et al., 1995; Tokunaga et al., 1997). The objective-type TIRF microscope shown in Figure 1.3B is relevant to this dissertation.

Total internal reflection is an optical phenomenon that can be employed to observe events occurring at boundaries. When light strikes the interface between two optical media of different refractive indices, the light incident at an angle greater than the critical angle undergoes total reflection. The critical angle $\theta(c)$ is given by the following equation:

$$\theta(c) = \sin^{-1}(n(2)/n(1)), \text{ where } n(1) > n(2)$$

$n(1)$ and $n(2)$ are the refractive indices of the substrate and the sample, respectively. To achieve total internal reflection illumination using a microscope objective at the substrate-sample interface, the numerical aperture of the objective must be greater than the refractive index of the sample. Beyond the angle of total reflection, the electromagnetic field of the incoming/reflected light still extends into the z direction. The strength of this field, often termed the evanescent wave, decreases exponentially with a decay constant of 100-200 nm. Only the portion of the sample within the evanescent field can be excited to emit fluorescence that is consequently seen or recorded, which results in a dramatically reduced probe volume compared with wide field illumination.

In the fluorescence microscope discussed in this dissertation, the substrate is a glass coverslip with a refractive index of about 1.5 and the sample is an aqueous solution with an index of 1.33-1.35. Hence, it is possible to achieve objective-type total internal reflection with a numerical aperture of 1.4. Most modern TIRF objectives have numerical apertures of 1.45-1.49. One can easily build an epifluorescence microscope capable of both wide field and objective-type TIRF from a commercial inverted microscope by constructing a periscope with a focusing lens behind the microscope that is mounted on a translation stage. A collimated beam can be aligned to pass through the focusing lens which, in the wide field case, focuses the beam onto the back aperture of the objective. For TIRF, one can translate the periscope such that the beam is focused onto the outer edge of the objective back aperture and emerges from the objective front aperture above the critical angle (Figure 1.3B). As long as the back-reflected laser beam is efficiently reflected, an objective-type TIRF microscope allows single molecule imaging near the glass-water interface even in the presence of nanomolar fluorophore concentrations (Blainey et al., 2006).

In a confocal fluorescence microscope as depicted in Figure 1.3C, instead of focusing the incoming laser beam onto the back aperture of the objective, one sends a collimated beam in the objective, which is focused to a tight spot in the sample. The probe volume of a confocal microscope is very small. Confocal microscopes usually employ point detectors, and include a pinhole in the detection path conjugate to the focal plane of the objective to reject out-of-focus fluorescence (Lu, 2005). The combination of a tightly focused excitation beam and a confocal pinhole allows for three-dimensional fluorescence imaging.

Because of the diffraction-limited illumination area, a confocal microscope requires some form of scanning in order to build up an image. In the simplest case, the sample can be scanned relative to a stationary focus using a high-precision piezo stage (Figure 1.3C). Stage-scanning confocal microscopes provide highly uniform illumination and excellent sensitivity at relative low imaging speeds. When high-speed imaging is required, a laser-scanning confocal microscope is more practical, in which the laser focus is scanned relative to a fixed sample using galvanometer mirrors (Lu, 2005).

1.4 Structure of This Thesis

This Ph.D. thesis covers two topics, both centering single molecule detection. The first topic is the development of imaging techniques based on absorption contrast, which accomplish single-molecule sensitivity at room temperature. The second topic is mechanism of bacterial transcription bursts, which is revealed through a series of *in vitro* and live-cell experiments using single-molecule fluorescence imaging.

Chapter 2 describes the motivation of label-free imaging of chromophores with undetectable fluorescence and introduces the principles of two novel imaging techniques based on absorption contrast with high sensitivity: stimulated emission microscopy and two-photon excited

photothermal microscopy. We demonstrate label-free mapping of the distribution of heme proteins, genetically encodable chromoproteins, and a transdermal drug at the cellular or tissue levels using these microscopies.

Chapter 3 presents ground state depletion microscopy for ultrasensitive detection of absorption contrast. We first image 20 nm gold nanoparticles using this microscopy, then demonstrate detection of the absorption signal from a single chromophore molecule at room temperature with shot-noise limited sensitivity. This measurement represents the ultimate detection sensitivity of nonlinear optical spectroscopy at room temperature.

Chapter 4 describes a novel high-throughput *in vitro* single-molecule assay based on RNA staining that allows real-time monitoring of transcription on individual DNA templates. This assay is capable of measuring the kinetics of transcription initiation, elongation and termination, and should be generally useful for studying many questions in transcription, such as bursting and pausing. In order to help any reader to set up the assay in the laboratory, detailed protocols are provided.

Transcription of highly expressed genes has been shown to occur in stochastic bursts (Golding et al., 2005; Taniguchi et al., 2010). But the origin of such ubiquitous phenomenon was unknown. In Chapter 5, we present the mechanism in bacteria. Using the *in vitro* single-molecule assay described in Chapter 4, we show that positive supercoiling buildup on a DNA segment by transcription slows down transcription elongation and eventually stops transcription initiation. Transcription can be resumed upon gyrase binding to the DNA segment. Furthermore, using single-cell mRNA counting fluorescence *in situ* hybridization (FISH), we show the extent of transcriptional bursting depends on the intracellular gyrase concentration. Together, these findings prove that transcriptional bursting of highly expressed genes in bacteria is primarily

caused by reversible gyrase dissociation from and rebinding to a DNA segment, changing the supercoiling level of the segment.

References

Betzig, E., and Chichester, R.J. (1993). Single Molecules Observed by near-Field Scanning Optical Microscopy. Science *262*, 1422-1425.

Blainey, P.C., van Oijen, A.M., Banerjee, A., Verdine, G.L., and Xie, X.S. (2006). A base-excision DNA-repair protein finds intrahelical lesion bases by fast sliding in contact with DNA. Proc Natl Acad Sci U S A *103*, 5752-5757.

Chong, S.S., Min, W., and Xie, X.S. (2010). Ground-State Depletion Microscopy: Detection Sensitivity of Single-Molecule Optical Absorption at Room Temperature. J Phys Chem Lett *1*, 3316-3322.

Elf, J., Li, G.W., and Xie, X.S. (2007). Probing transcription factor dynamics at the single-molecule level in a living cell. Science *316*, 1191-1194.

Fleming, G.R. (1986). Chemical applications of ultrafast spectroscopy (London: Oxford University Press).

Freudiger, C.W., Min, W., Saar, B.G., Lu, S., Holtom, G.R., He, C.W., Tsai, J.C., Kang, J.X., and Xie, X.S. (2008). Label-Free Biomedical Imaging with High Sensitivity by Stimulated Raman Scattering Microscopy. Science *322*, 1857-1861.

Fu, D., Matthews, T.E., Ye, T., Piletic, I.R., and Warren, W.S. (2008). Label-free in vivo optical imaging of microvasculature and oxygenation level. J Biomed Opt *13*, 040503.

Fu, D., Ye, T., Matthews, T.E., Chen, B.J., Yurtserver, G., and Warren, W.S. (2007a). High-resolution in vivo imaging of blood vessels without labeling. Opt Lett *32*, 2641-2643.

Fu, D., Ye, T., Matthews, T.E., Yurtsever, G., and Warren, W.S. (2007b). Two-color, two-photon, and excited-state absorption microscopy. J Biomed Opt *12*, 054004.

Funatsu, T., Harada, Y., Tokunaga, M., Saito, K., and Yanagida, T. (1995). Imaging of Single Fluorescent Molecules and Individual Atp Turnovers by Single Myosin Molecules in Aqueous-Solution. Nature *374*, 555-559.

Golding, I., Paulsson, J., Zawilski, S.M., and Cox, E.C. (2005). Real-time kinetics of gene activity in individual bacteria. Cell *123*, 1025-1036.

Hirschfeld, T. (1976). Optical Microscopic Observation of Single Small Molecules. Appl Optics *15*, 2965-2966.

Lu, H.P., Xun, L.Y., and Xie, X.S. (1998). Single-molecule enzymatic dynamics. Science *282*, 1877-1882.

Lu, P. (2005). Confocal Scanning Optical Microscopy and Nanotechnology. In Handbook of Microscopy for Nanotechnology, N. Yao, and Z. Wang, eds. (Springer US), pp. 3-24.

Macklin, J.J., Trautman, J.K., Harris, T.D., and Brus, L.E. (1996). Imaging and time-resolved spectroscopy of single molecules at an interface. Science *272*, 255-258.

Min, W., Lu, S.J., Chong, S.S., Roy, R., Holtom, G.R., and Xie, X.S. (2009). Imaging chromophores with undetectable fluorescence by stimulated emission microscopy. Nature *461*, 1105-1109.

Orrit, M., and Bernard, J. (1990). Single Pentacene Molecules Detected by Fluorescence Excitation in a Para-Terphenyl Crystal. Phys Rev Lett *65*, 2716-2719.

Shera, E.B., Seitzinger, N.K., Davis, L.M., Keller, R.A., and Soper, S.A. (1990). Detection of Single Fluorescent Molecules. Chem Phys Lett *174*, 553-557.

Taniguchi, Y., Choi, P.J., Li, G.W., Chen, H., Babu, M., Hearn, J., Emili, A., and Xie, X.S. (2010). Quantifying E. coli proteome and transcriptome with single-molecule sensitivity in single cells. Science *329*, 533-538.

Tokunaga, M., Kitamura, K., Saito, K., Iwane, A.H., and Yanagida, T. (1997). Single molecule imaging of fluorophores and enzymatic reactions achieved by objective-type total internal reflection fluorescence microscopy. Biochem Bioph Res Co *235*, 47-53.

Vale, R.D., Funatsu, T., Pierce, D.W., Romberg, L., Harada, Y., and Yanagida, T. (1996). Direct observation of single kinesin molecules moving along microtubules. Nature *380*, 451-453.

Wei, L., and Min, W. (2012). Pump-probe optical microscopy for imaging nonfluorescent chromophores. Analytical and bioanalytical chemistry *403*, 2197-2202.

Xie, X.S., and Dunn, R.C. (1994). Probing Single-Molecule Dynamics. Science *265*, 361-364.
Yajima, T., Yoshihara, K., Harris, C.B., and Shionoya, S. (1988). Ultrafast phenomena VI. (Springer-Verlag).

Yu, J., Xiao, J., Ren, X., Lao, K., and Xie, X.S. (2006). Probing gene expression in live cells, one protein molecule at a time. Science *311*, 1600-1603.

Chapter 2

Label-free imaging of biological chromophores

Fluorescence, i.e., spontaneous emission, is generally more sensitive than absorption measurement, and is widely used in optical imaging. However, many chromophores, such as hemoglobin and cytochromes, absorb but have undetectable fluorescence because their spontaneous emission is dominated by fast non-radiative decay. Yet the detection of their absorption is difficult under a microscope. In this chapter, we describe two contrast mechanisms for label-free imaging of the non-fluorescent chromophores based on absorption detection. The first contrast mechanism is stimulated emission, which competes effectively with the non-radiative decay to make the chromophores detectable. In a pump–probe experiment, on photo excitation by a pump pulse, the sample is stimulated down to the ground state by a time-delayed probe pulse, the intensity of which is concurrently increased. We extract the miniscule intensity increase with shot-noise-limited sensitivity by using a lock-in amplifier and intensity modulation of the pump beam at MHz frequency. The second contrast mechanism is two-photon excited photothermal effect. A thermal lens scheme and a high-frequency modulation are utilized to enhance the signal-to-noise ratio. In both contrast mechanisms, the signal is generated only at the laser foci owing to the nonlinear dependence on the input intensities, which provides the microscopies intrinsic three-dimensional (3D) optical sectioning capability. We demonstrate label-free high-sensitivity imaging of chromoproteins, cytochromes, drugs for photodynamic therapy and microvascular networks in mouse ear tissue and a zebrafish gill.

2.1 Background

2.1.1 Biological chromophores with undetectable fluorescence

While fluorescence, i.e., spontaneous emission, has long been considered to be the most sensitive contrast mechanism in optical bioimaging, many chromophores absorb but do not have detectable fluorescence, because they have very short-lived excited states and their spontaneous emission rates are much lower than the fast non-radiative decay. As a result, their feeble fluorescence is overwhelmed by backgrounds, such as stray light, solvent Raman scattering, and detector dark counts. However, the distribution and dynamics of many non-fluorescent chromophores, such as heme proteins, are of significant interest in biological and medical research.

Heme proteins like hemoglobins and cytochromes participate in crucial processes like electron and oxygen transport and apoptosis. To be able to image the distribution of heme proteins with high sensitivity could greatly facilitate biomedical studies such as tumor angiogenesis, cerebral oxygen delivery in brain, and apoptosis signaling (Grinvald et al., 1986; Jiang and Wang, 2004; McDonald and Choyke, 2003). In particular, medical applications such as vascular imaging require 3D high spatial resolution down to single capillaries and image contrast generated by endogenous means would be preferable to exogenous contrast agents. Hence, developing label-free non-fluorescence optical imaging techniques to visualize these chromophores in their natural physiological environment is challenging yet rewarding.

2.1.2 Stimulated emission

The phenomenon of stimulated emission was first described by Einstein in 1917 (Einstein, 1917). An atom or molecule in its excited state can be stimulated down to the ground state by an incident light field, resulting in the creation of a new coherent photon identical to those in the

original incident field. This process only occurs when the frequency of the incident field matches the transition energy. Stimulated emission was later used as a fundamental principle for light amplification in the laser (Seigman, 1986). The depopulation aspect of stimulated emission has been used for population dumping from excited states (Hamilton et al., 1986), super-resolution fluorescence (STED) microscopy (Hell and Wichmann, 1994), and fluorescence lifetime imaging (Dong et al., 1995). The light amplification aspect of stimulated emission can be utilized as a contrast mechanism for highly sensitive imaging of chromophores with undetectable fluorescence.

2.1.3 Photothermal microscopy

Photothermal microscopy is an emerging technique to detect absorbing microscopic objects, and is particularly suitable for imaging metal particles (Boyer et al., 2002; Brusnichkin et al., 2007; Cognet et al., 2003). In photothermal microscopy, an excitation laser beam induces optical absorption that generates refractive index gradient due to local heating, which is probed by a second beam through a modulation transfer scheme similar to that in pump-probe experiments (Bialkowski, 1996; Boyer et al., 2002; Brusnichkin et al., 2007; Cognet et al., 2003; Tokeshi et al., 2001). Upon photo-excitation, the spontaneous emission rates of non-fluorescent chromophores are much lower than the fast non-radiative decay, therefore most of the energy absorbed is dissipated as heat, suggesting that the photothermal effect could be another ideal contrast mechanism for sensitive imaging of these chromophores.

2.2 Results and Discussion

2.2.1 Principle of stimulated emission microscopy

We conduct a dual beam experiment in order to interrogate the short-lived excited state by stimulated emission, which can compete with the non-radiative decay under strong enough

stimulating field strength (Figure 2.1). The resulting "amplification" of the stimulation beam can then be detected in the presence of the background signals.

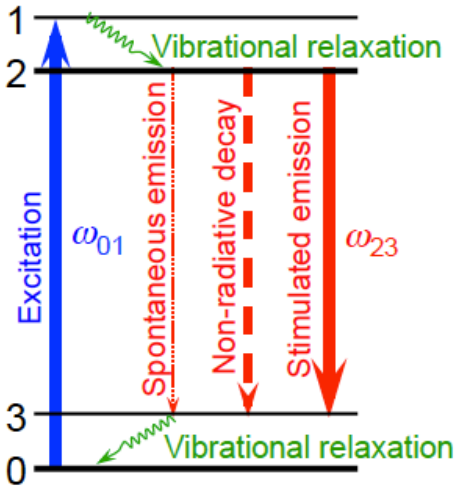

Figure 2.1 Energy diagram of spontaneous emission, non-radiative decay and stimulated emission processes for a typical four-level energy system.

Non-radiative decay dominates spontaneous emission for chromophores with undetectable fluorescence. However, when the stimulation field is designed to have the correct energy and timing, the stimulated emission can compete with non-radiative decay and become the dominating decay pathway.

Considering the optical excitation at frequency ω_{01} (Figure 2.1), the absorption cross section $\sigma_{abs[0\to1]}$ is ~ 10^{-16} cm^2 for a single chromophore at room temperature (Cantor and Schimmel, 1980; Turro, 1991). As shown in Figure 2.2, under a tightly focused laser beam with a beam waist area of S (~ 10^{-9} cm^2), the integrated intensity attenuation of the excitation beam, $\Delta I_E / I_E$, is proportional to the ratio between $\sigma_{abs[0\to1]}$ and S:

$$\Delta I_E / I_E = -N_0 \cdot \sigma_{abs[0\to1]} / S \qquad (2.1)$$

where N_0 is the number of molecules in the ground state. For a single chromophore, $\Delta I_E / I_E$ is on the order of 10^{-7}. Such small attenuation cannot be detected by conventional absorption microscopy. We note that single molecule absorption was previously achieved in cryogenic temperatures using a frequency modulation method (Moerner and Kador, 1989), which is

however difficult to implement at room temperature because of the broad molecular absorption spectrum. Moreover, absorption measurement is often complicated by scattering when imaging biological specimen. Instead of detecting direct absorption, here we detect the stimulated emission followed by the excitation of the molecule.

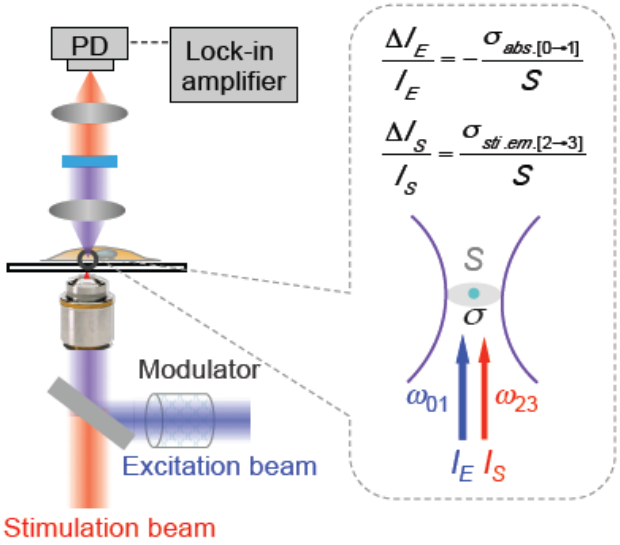

Figure 2.2 Stimulated emission microscopy.

The incident excitation and delayed stimulation pulse trains are spatially overlapped and focused onto the common focal spot in the sample. A modulator switches the intensity of the excitation beam on-and-off at 5 MHz. The spectrally filtered stimulation beam is detected by a large-area photodiode, and demodulated by a lock-in amplifier to create the image contrast while raster scanning the collinear exciting and stimulating beams. The relative energy gain or loss of the stimulation and excitation beam, respectively, for a single chromophore at the laser focus (area of *S*), is given by the equations (inset).

According to Einstein (Einstein, 1917), the molecular cross section $\sigma_{sti.em.}$ for stimulated emission is comparable to σ_{abs}, because of microscopic reversibility. Unlike the absorption that results in attenuation, the stimulation beam will experience an intensity gain after interacting with the molecules

$$\Delta I_S / I_S = +N_2 \cdot \sigma_{sti.em.[2\to3]} / S \quad (2.2)$$

where N_2 is the number of excited molecules transiently probed by the stimulation pulses (Figure 2.2). For a single chromophore, $\Delta I_S / I_S$ is also ~10^{-7}. Without special techniques, such a small signal would be again buried in the noise (~1%) of the stimulation beam.

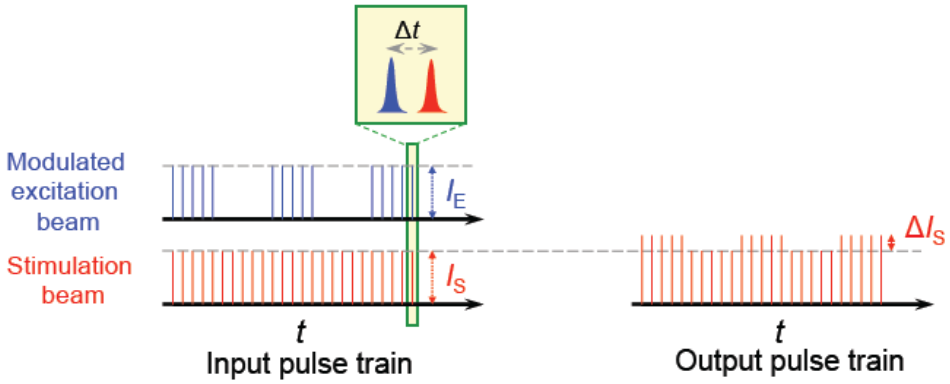

Figure 2.3 Principle of high-frequency modulation.
As the intensity of the excitation beam is modulated on-and-off in time, the corresponding stimulated emission signal is also modulated at the same frequency. The stimulation pulses are made to lag behind the excitation pulses by an appropriate amount Δt .

To overcome this noise problem and promote the advantage of performing stimulated emission, we implemented a high-frequency (>1 MHz) phase-sensitive detection technique. In the scheme shown in Figure 2.2&2.3, the intensity of the excitation beam is modulated at 5 MHz, and this creates a modulation of the stimulated emission signal at the same frequency, because only when the excitation beam is present can the gain of the stimulation beam occur. Such an induced modulation signal can then be sensitively extracted by a lock-in amplifier referenced to this high frequency. In this way, the stimulated emission signal can be detected against the low-frequency laser noise (DC to kHz) with a superior sensitivity. In contrast, it is difficult to implement such modulation scheme for high sensitivity one-beam absorption measurement (Ye et al., 1998).

Specifically, we use a ~200 fs (FWHM) pulse train for excitation, and another ~200 fs pulse train for stimulation. The time delay between these two pulse trains is chosen to be ~300 fs

(Figure 2.3), which is shorter than the excited state lifetime (sub-ps) of the chromophores. This delay also eliminates contributions from other instantaneous optical processes, such as two photon absorption (Fu et al., 2007), cross phase modulation and SRS (Freudiger et al., 2008).

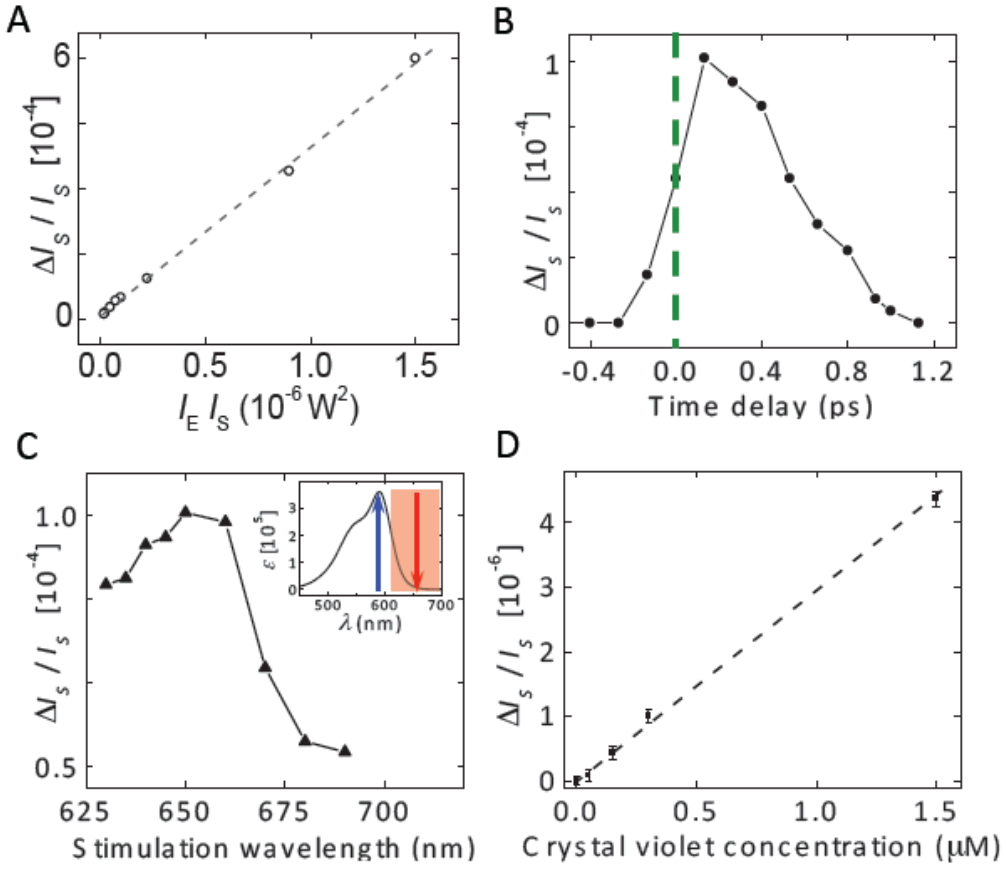

Figure 2.4 Characterizations of stimulated emission microscopy.

(A) Stimulated emission signal from 30 μM crystal violet/water solution is proportional to the product of excitation beam power, I_E, and stimulation beam power, I_S. (B) Stimulated emission signal as a function of time delay between the excitation (590 nm) and the stimulation (660 nm) pulses. The decay of the signal (~ 0.6 ps) reflects the short excited state lifetime. The FWHM of the pulses is ~200 fs. (C) Measured stimulated emission spectrum is in agreement with the reported fluorescence spectrum of crystal violet in glycerol solution (Rittweger et al., 2007). 590 nm excitation is fixed while the stimulation wavelength is scanned by tuning the other OPO wavelength. A time delay of 0.3 ps is used. Inset is the absorption spectrum of crystal violet in water. (D) Stimulated emission signal scales linearly with crystal violet concentration in aqueous solution. Continuous flow of the sample is used to replenish molecules. 590 nm and 660 nm for excitation and stimulation beam, respectively. 0.3 ps time delay is used. Error bars show 1 s.d. of the signals from a 30 sec recording. The detection limit was determined to be 60 nM with a signal-to-noise ratio of 1:1.The excitation and stimulation beam intensities at the focus are 0.2 mW (~0.14 MW/cm^2) and 1 mW (~0.70 MW/cm^2), respectively. For 1 sec time constant at the lock-in amplifier, a relative signal of 10^{-7} for $\Delta I_S / I_S$ can be detected.

We conduct the experiment under a non-saturating condition of the four-level system (Figure 2.1). Under this condition, N_2 in Eq. 2.2 originates from a linear excitation: $N_2 \propto N_0 \cdot I_E \cdot \sigma_{abs[0\to1]}/S$. This relation, together with Eq. 2.2, indicates that the final signal ΔI_S is linearly dependent on both I_E and I_S,

$$\Delta I_S \propto N_0 \cdot I_E \cdot I_S \cdot \left(\sigma_{abs[0\to1]}/S\right)\cdot\left(\sigma_{sti.em.[2\to3]}/S\right) \qquad (2.3)$$

The overall quadratic power dependence, as experimentally demonstrated (Figure 2.4A), would allow 3D optical sectioning, as in many other multi-photon techniques (Denk et al., 1990; Evans and Xie, 2008). Such dependence also confirms the non-saturation condition within the intensity range used. Moreover, it offers, in principle, a spatial resolution of twice as high (in spatial frequency) as in conventional fluorescence microscopy.

Figure 2.4B shows the stimulated emission signal as a function of the time-delay between the excitation and stimulation pulses. In pump-probe experiment, the signal could arise from ground state recovery, excited state absorption or stimulated emission. Ground state recovery is avoided here by the large Stokes shift of stimulation beam from molecular absorption band. Excited state absorption is negligible compared to stimulated emission based on the observed intensity increase of the stimulation beam, consistent with a study of fluorescence quenching in STED microscopy (Rittweger et al., 2007). The initial rise in Figure 2.4B is due to vibrational relaxation from level 1 to level 2 (Figure 2.1), while the subsequent decay indicates the short excited state lifetime (~0.6 ps) of level 2, which underlies the undetectable fluorescence. Such a short lifetime also reduces the probability of going into the triplet state, effectively protecting the molecule from photobleaching. The stimulated emission spectrum (Figure 2.4C), recorded by tuning the wavelength of the stimulated beam, is also in agreement with the reported emission

spectrum of crystal violet in glycerol (Du et al., 1998), where the high viscosity increases the fluorescence quantum yield.

Figure 2.4D shows that the stimulated emission signal depends linearly on analyte concentration, as predicted by Eq. 2.3. This allows straightforward quantitative analysis. The limit of detection is ~60 nM for crystal violet with 1 sec integration time. This sensitivity effectively corresponds to a few (<5) molecules in focus, which has surpassed the detection limit of recently reported for SRS microscopy (Freudiger et al., 2008) by orders of magnitude because of the strong electronic transition. The ultimate sensitivity would be achieved under the condition of saturated excitation but near-saturated stimulation, and is fundamentally determined by the shot noise of the stimulation beam ($\Delta I_S / I_S \sim 10^{-7.5}$ for ~1 mW averaged over 1 sec).

2.2.2 Imaging biological chromophores with stimulated emission microscopy

As the first biological application, we imaged distributions of chromoproteins in live *E. coli* cells. Genetically encodable chromoproteins, such as gtCP (Gurskaya et al., 2001) and cjBlue (Chan et al., 2006), are naturally existing variants of green fluorescent proteins (Zhang et al., 2002), and only absorb light but do not fluoresce. When the gene encoding for gtCP is expressed in *E. coli* cells, tetrameric gtCP can be clearly visualized to reside homogeneously inside cytoplasm by stimulated emission microscopy (Figure 2.5A&B). Similarly, the distribution of another chromoprotein, cjBlue, can be imaged (Figure 2.5C&D). Unlike gtCP that is expressed in most cells, cjBlue is expressed in a fraction of them, as we see from the corresponding transmission image. Therefore, stimulated emission microscopy opens the possibility of visualizing chromoproteins that are not accessible by fluorescence microscopy.

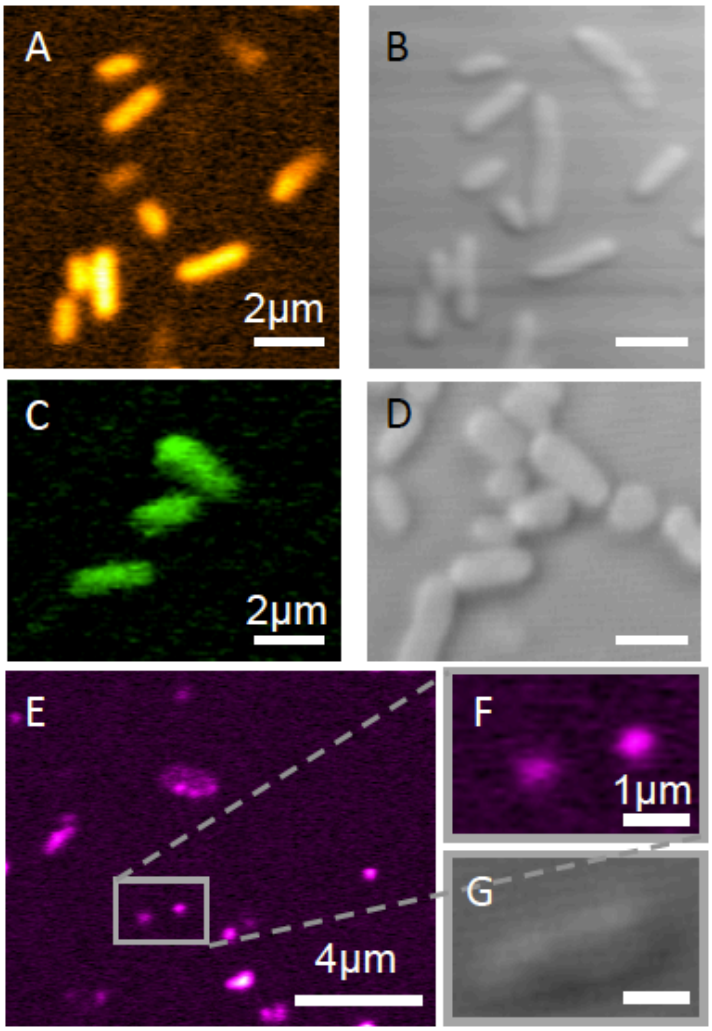

Figure 2.5 Imaging non-fluorescent chromoproteins and chromogenic reporter for gene expression.

Imaging distributions of cytoplasmic chromoproteins gtCP (A) and cjBlue (C) in live *E. coli* cells, respectively, by stimulated emission microscopy. (B) and (D) are the corresponding wide-field transmission images. Plasmids containing the genes encoded for gtCP and cjBLue are transformed into *E. coli*, respectively. Compared to gtCP, cjBlue is expressed less abundantly inside cells. (E) Stimulated emission imaging of the oxidation product (4,4'-dichloro-5,5'-dibromoindigo) resulting from X-gal hydrolysis catalyzed by *β*-galactosidase, the protein encoded by lacZ reporter gene. Indigo accumulation in *E. coli* cells is detected without any lacZ induction. The signal is detected only when both the cells and X-gal are present. Unlike the homogeneous protein images in (A) and (C), indigo product shows inhomogeneous localized distribution inside cells due to its insolubility, as shown in the magnified image (F). The direct transmission image (G) shows the morphology of the same region. gtCP and cjBlue absorb around 580 nm (Gurskaya et al., 2001) and 610 nm (Chan et al., 2006), respectively; X-gal hydrolysis product has a broad absorption around 600~650 nm. In (A) and (C), 590 nm and 660 nm for excitation and stimulation, respectively; in (E) and (F), 600 nm and 680 nm for excitation and stimulation, respectively. The excitation and stimulation beams of 0.1and 0.3mW, respectively, and ~0.3 ps of time delay are used for all the above images. All of the images were taken between 5 sec and 45 sec, depending on the image size.

Next, we show the stimulated emission imaging in live *E. coli* cells of a non-fluorescent indigo reaction product commonly used to assay gene expression. *β*-galactosidase catalyzes the cleavage of the glycosidic linkage of X-gal, a popular chromogenic substrate, eventually forming an indigo product after oxidation (Miller, 1972). The gene encoding *β*-galactosidase, lacZ, is a classic reporter gene. Traditionally, the indigo product has to accumulate in sufficient concentration for its blue color to be visible (Miller, 1972). With stimulated emission, the accumulation of the indigo product can now be monitored in wild-type cells without induction of lacZ (Figure 2.5E-G). The inhomogeneous distribution of indigo product inside individual cells (Figure 2.5E&F) is consistent with the fact that this product is insoluble and tends to form localized precipitates. In contrast, the corresponding transmission image (Figure 2.5G) shows no signs of any color. We note that an assay using a fluorogenic substrate has been recently developed (Cai et al., 2006), but it requires a microfluidics to enclose individual cells because the hydrolysis product there is quickly pumped out by the cell. Hence, stimulated emission microscopy allows monitoring of a product presumed to report basal lacZ gene activity with superb sensitivity.

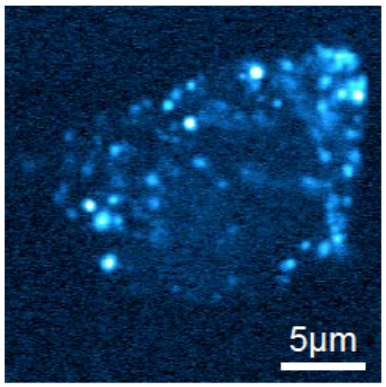

Figure 2.6 TBO distribution in a human embryonic kidney (HEK) 293 cell.
The image was taken one hour after incubating the cell with 10 μM TBO/PBS solution. Local accumulation of the dye is observed inside cytoplasm instead of in the membrane or the nucleus. Color table (also for Figure 2.7): cyan hot. The brightest and darkest colors correspond to ~ 10^{-4} and ~ 10^{-5} of the relative modulation depth, respectively.

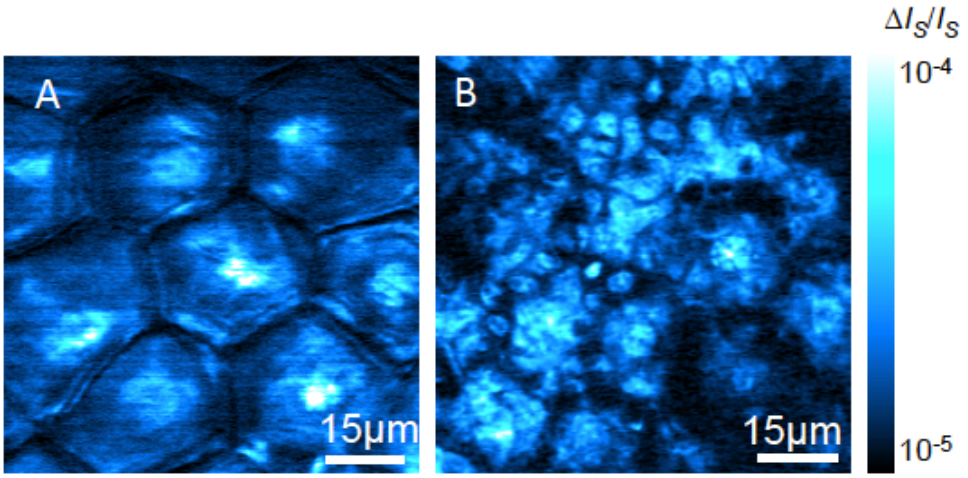

Figure 2.7 Transdermal drug distribution in 3D imaging.

Drug delivery of toluidine blue O (TBO), a drug used as photosensitizer in photodynamic therapy, in a freshly cut mouse ear skin the same area at two different depths, 3 and 25 μm, respectively, 30 min after topical application of 10 μM TBO/PBS solution. At the surface layer (3 μm) of *stratum corneum*, (A) shows TBO is accumulated in the protein phase of the polygonal cells rather than in the lipid-rich intercellular space. At the layer of epidermis (25 μm), (B) shows a rich TBO distribution following the subcellular cytoplasm of nucleated basal keratinocytes. These images support the 'hydrophilic path' as a main pathway for transdermal drug delivery of TBO. 600 nm and 680 nm for excitation and stimulation, respectively. The excitation and stimulation beams have 0.1 and 0.3 mW, respectively, at the focus. ~0.3 ps time delay is used. The color table (cyan hot) shows the magnitude of $\Delta I_S / I_S$.

Monitoring transdermal delivery of non-fluorescent drug with intrinsic 3D optical sectioning is another application. In particular, we show mapping of a cationic thiazine dye toluidine blue O (TBO) at both the cellular and tissue levels. Having a selective affinity for cancer cells *in vivo*, TBO is a photosensitizer in photodynamic therapy (Chelvanayagam and Beazley, 1997; Tremblay et al., 2002). Subcellular localization of TBO is crucial since it influences both the level and the kinetics of apoptosis induction. However, it is difficult to image the true TBO distribution, because its fluorescence is quenched when bound to tissue substrates and only the non-specific stain residue in the tissue retains its native fluorescence (Chelvanayagam and Beazley, 1997). Independent of the complication from fluorescence contrast, stimulated emission microscopy is suitable for this problem. The stimulated emission image of TBO inside the cancer cells after incubation shows its local accumulation (Figure 2.6). When topically applied to skin

tissue, being hydrophilic and water soluble, TBO is enriched in the center of the protein phase of the polygonal *stratum corneum* cells rather than in the intercellular space which is in lipid phase (Figure 2.7A). At a 20 μm deeper depth, TBO displays a rich subcellular distribution in the cytoplasm of epidermis where cellular proliferation actively takes place (Figure 2.7B). These imaging results support the hydrophilic delivery pathway as well as the recent hypothesis of TBO binding to cytoplasmic RNA to initiate apoptosis (Tremblay et al., 2002).

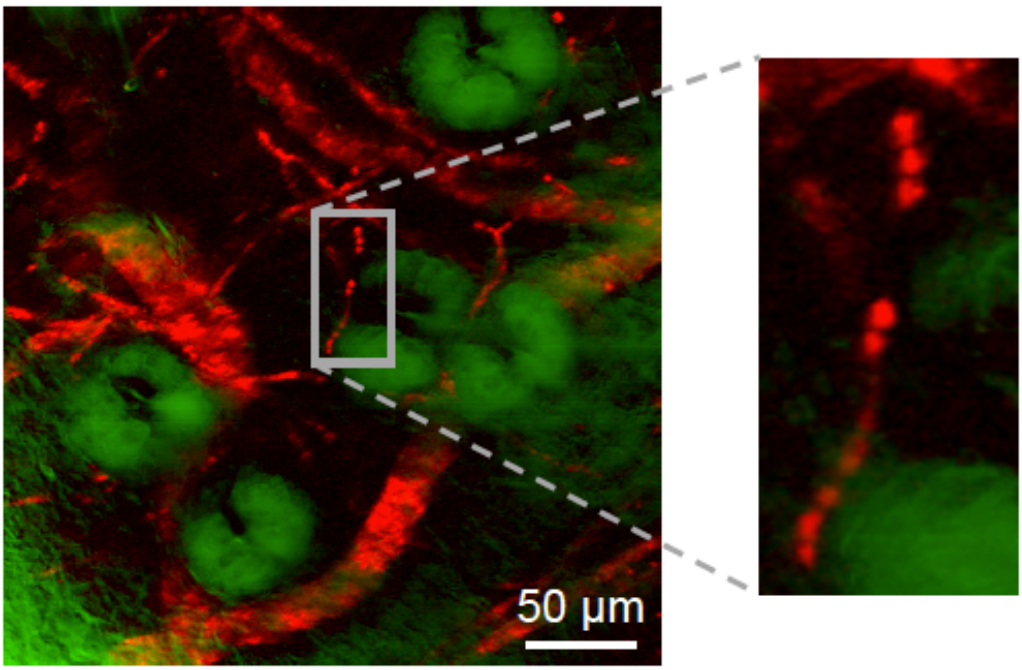

Figure 2.8 *Ex vivo* imaging of microvasculature network of a mouse ear based on endogenous hemoglobin contrast.

Stimulated emission image (red channel, maximum intensity projection) shows the blood vessel network surrounding sebaceous glands (green channel, simultaneously recorded by confocal reflectance). Shown by the zoomed-in image, individual red blood cells are lined up within a single capillary (~5 μm in diameter). 830 nm (~20 mW) and 600 nm (~3 mW) are used for two-photon excitation of Soret band and one-photon stimulated emission of *Q* band of hemoglobin, respectively. Pulse widths of both excitation and stimulation beams are about 0.2 ps with ~0.2 ps time delay between them.

Finally, we demonstrate label-free imaging of microvascular based on endogenous contrast from non-fluorescent hemoglobin. Structure and hemodynamics of blood vessels play a major role in many biomedical processes such as angiogenesis in tumors (McDonald and Choyke, 2003)

and cerebral oxygen delivery in brain (Grinvald et al., 1986; Kleinfeld et al., 1998). However, established techniques such as MRI, CT, PET, ultrasound, photoacoustic tomography (Stein et al., 2009), confocal and two-photon fluorescence microscopy either lack the spatial resolution needed for resolve individual capillaries or require exogenous contrast agents. Here we perform *ex vivo* stimulated emission imaging of the well-developed vascular network from a nude mouse ear, by exciting the Soret band of hemoglobin through efficient two-photon absorption (Clay et al., 2007) and subsequently stimulating the emission from its *Q* band which has longer excited state lifetime than Soret band (Wang et al., 2000). As shown in Figure 2.8, blood vessels (in red) branch and loop around sebaceous glands (in green). In addition, single red blood cells can be clearly seen to reside within individual capillaries (~5 μm in diameter). Two photon absorption has been recently developed to image hemoglobin (Fu et al., 2007). We note that stimulated emission is more sensitive because it involves direct one-photon transition. Furthermore, our new technique offers the prospect of 3D mapping of blood oxygenation level for addressing broad physiological and pathological problems (Grinvald et al., 1986; Kleinfeld et al., 1998; McDonald and Choyke, 2003).

We note that the complexity and cost of the instrument can be much reduced as fiber laser sources are adapted. Stimulated emission microscopy allows imaging of non-fluorescent chromophores with 3D optical sectioning and high sensitivity, and extends the repertoire of reporters for biological imaging beyond fluorophores.

2.2.3 Principle of two-photon excited photothermal microscopy

In previously reported photothermal imaging schemes, a continuous wave laser was used for one-photon excitation, and the local heating was probed by a second laser beam. Here we use two-photon nonlinear excitation by a near infrared (NIR) ultrafast laser to image heme proteins.

This excitation scheme offers a number of useful features. First, as a consequence of the nonlinear intensity dependence, two-photon excitation confines the absorbing volume to the exact focal volume. As shown in the inset of Figure 2.9, compared to the conventional one-photon excitation, the resulting two-photon excited thermal gradient is less "dilute" and much more concentrated along the z- axis, which would significantly enhance the readout signal generated by the probe beam (Denk et al., 1990). Second, compared with one-photon visible excitation, NIR light has much larger penetration depth in scattering tissue and causes much less damage on biological samples (Denk et al., 1990). Third, the intense Soret band (~415 nm) of heme proteins has recently been shown to exhibit a large and specific two-photon absorption cross section near 830 nm (Clay et al., 2007). These desirable features of two-photon excited photothermal microscopy make it possible to image heme proteins in living cells and highly scattering tissues with superb sensitivity.

The schematic of two-photon excited photothermal microscope is depicted in Figure 2.9. A near IR ultrafast laser beam (~200 fs pulse width) at 830 nm with repetition rate of 76 MHz serves as the excitation beam, and a continuous wave laser at 785 nm serves as the probe beam. After spatially combined by a dichroic mirror, these two beams are focused coaxially into the specimen through a microscope objective. After passing the specimen, the beams are collected by a condenser. The excitation beam is blocked by an optical filter, and the probe beam is focused onto a large-area Si photodiode.

A thermal lens detection scheme, which is among the most sensitive methods of the family of photothermal spectroscopy approaches (Bialkowski, 1996; Tokeshi et al., 2001), is adopted in our method to enhance the detection sensitivity. We wish to detect the refractive index gradient generated by the excitation beam. To do so, an iris diaphragm with an adjustable aperture size

and position is installed in front of the detector. Only the central portion of the probe beam instead of the entire beam is allowed to pass through the iris and hit the detector. The final two-photon excited photothermal lens signal is dependent on (Bialkowski, 1996)

$$S \propto \frac{I_{ex}^2 \cdot I_{pr} \cdot \sigma_{2-p} \cdot [c] \cdot \eta_H}{\lambda_{pr} \cdot \kappa} \left(\frac{dn}{dT} \right)_P \qquad (2.4)$$

where I_{ex} and I_{pr} are the intensity of the excitation beam and probe beam, respectively, σ_{2-p} is the two-photon absorption cross section, $[c]$ is the sample concentration, η_H is the yield of heat dissipation, λ_{pr} is the wavelength of the probe beam, κ is the thermal conductivity, and $(dn/dT)_P$ is the refractive index temperature coefficient at constant pressure.

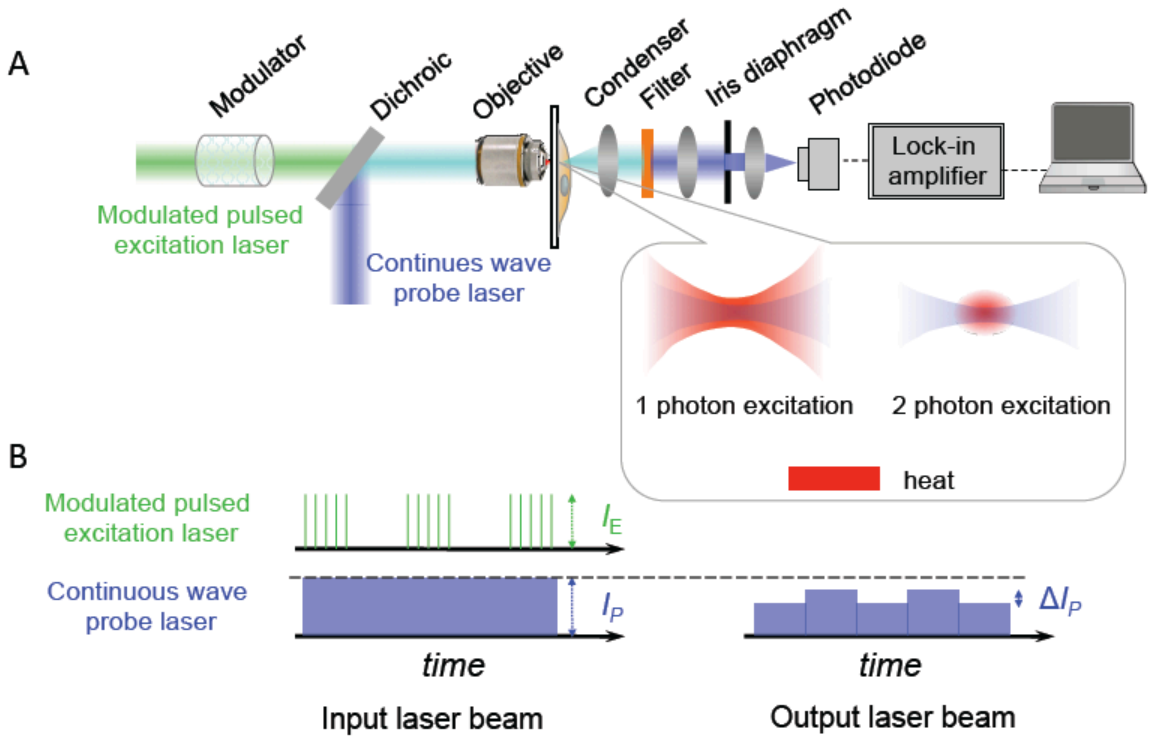

Figure 2.9 Principle of two-photon excited photothermal lens microscopy.

(A) Experimental apparatus. The incident ultrafast excitation (~200 fs at 830 nm) and continuous wave probe beams at 785 nm are spatially overlapped and focused onto the sample. A modulator switches the intensity of the excitation beam on-and-off at ~100kHz. While the collinear excitation and probe beams are raster scanned across the sample, the spectrally filtered probe beam is collected by the condenser-lens pair, de-scanned onto an iris diaphragm with adjustable position and aperture, and is refocused onto a large-area photodiode, and demodulated by a lock-in amplifier to create the image contrast. The inset shows that the thermal gradient (in red) generated by two-photon excitation is spatially more concentrated than that by one-photon excitation, especially along z- axis. (B) Principle of high-frequency modulation. As the intensity of the excitation beam is modulated on-and-off in time, the probe beam intensity on the detector is also modulated at the same frequency, when the iris diaphragm only passes the central portion of the probe beam.

To significantly reduce the detection noise, we implement a high-frequency (>50 kHz) phase-sensitive detection scheme. In the scheme shown in Figure 2.9, the intensity of the excitation beam is modulated by an acoustic-optical modulator, creating a modulation of the photothermal signal at a frequency of our choice. Such an induced modulation signal can then be sensitively extracted by a lock-in amplifier referenced to this modulation frequency.

2.2.4 Imaging heme proteins with two-photon excited photothermal microscopy

We first demonstrate imaging individual red blood cells to characterize a few microscopic parameters. When the iris diaphragm is fully open to collect all the intensity of the forward propagating probe beam, the photothermal image, shown in Figure 2.10A, is essentially blank. However, when the iris is partially closed to block the peripheral portion of the probe beam, the corresponding image clearly reveals individual red blood cells (Figure 2.10B). Such a remarkably sensitive dependence on the collection geometry of the probe beam is a manifestation of the underlying thermal lens effect.

Modulation frequency of the phase sensitive detection is another crucial parameter in photothermal microscopy. As shown in Figure 2.10C, the absolute signal increases as the modulation frequency decreases, because it allows longer time for the thermal gradient to build up. However, the laser noise of the probe beam also starts to increase as the modulation frequency decreases. In addition, in order to reliably demodulate the signal for each pixel, the pixel dwell time, which determines the imaging speed, has to be significantly longer than the modulation period. Therefore, balancing between signal, noise and imaging speed, we choose ~100 kHz modulation frequency for the scanning microscopy.

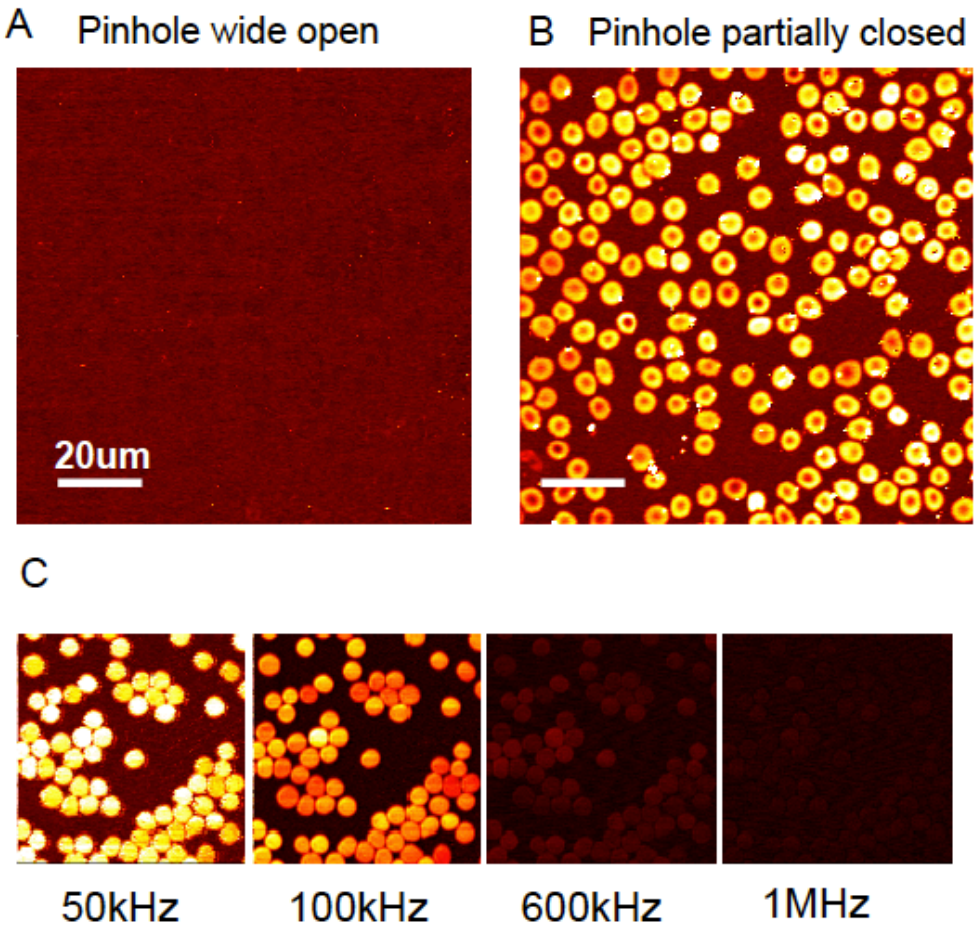

Figure 2.10 Imaging individual red blood cells under different parameters.

(A) When the iris diaphragm is fully open, the photothermal lens signal vanishes. (B) The size and the position of the iris diaphragm is adjusted to let the central portion of the CW probe beam pass through and be detected by the photodiode. The image clearly reveals individual red blood cells with a characteristic toroidal shape. (C) The photothermal signal decreases with increasing modulation frequency from 50 kHz to 1 MHz. To maintain high signal, low noise and reasonably fast imaging speed, the modulator is set at ~100 kHz for all of the following images.

We then demonstrate the application of this microscopy in live cell imaging. Mitochondria contain membrane-bound cytochromes that have important roles in electron transport and controlling of apoptosis. Cytochromes are small protein molecules (~12 kD) containing a heme group, which are difficult to label without affecting their normal physiology. As shown in Figure 2.11A&B, the asymmetric cellular distribution of cytochromes are shown and individual mitochondrion can be clearly resolved. This technique could allow study of fusion-fission mitochondrial dynamics in live cells in a label-free manner (Detmer and Chan, 2007).

Finally, we demonstrate label-free imaging of microvascular network based on the endogenous contrast from hemoglobin. Figure 2.11C shows the image of vascular network from a mouse ear. The capillaries are seen to wrap around the sebaceous glands shown in the transmission image (Figure 2.11D). Furthermore, we perform imaging on a whole organism level. Larval zebrafish is transparent and provides an ideal vertebrate model for cancer progression and angiogenesis, which is readily amenable to genetic and pharmacological screening (Stoletov et al., 2007). Figure 2.11E shows a 3D reconstruction of the blood vessel of a larval zebrafish gill. In contrast its transmission image (Figure 2.11F), the two-photon excited photothermal contrast allows deep penetration in the scattering tissue.

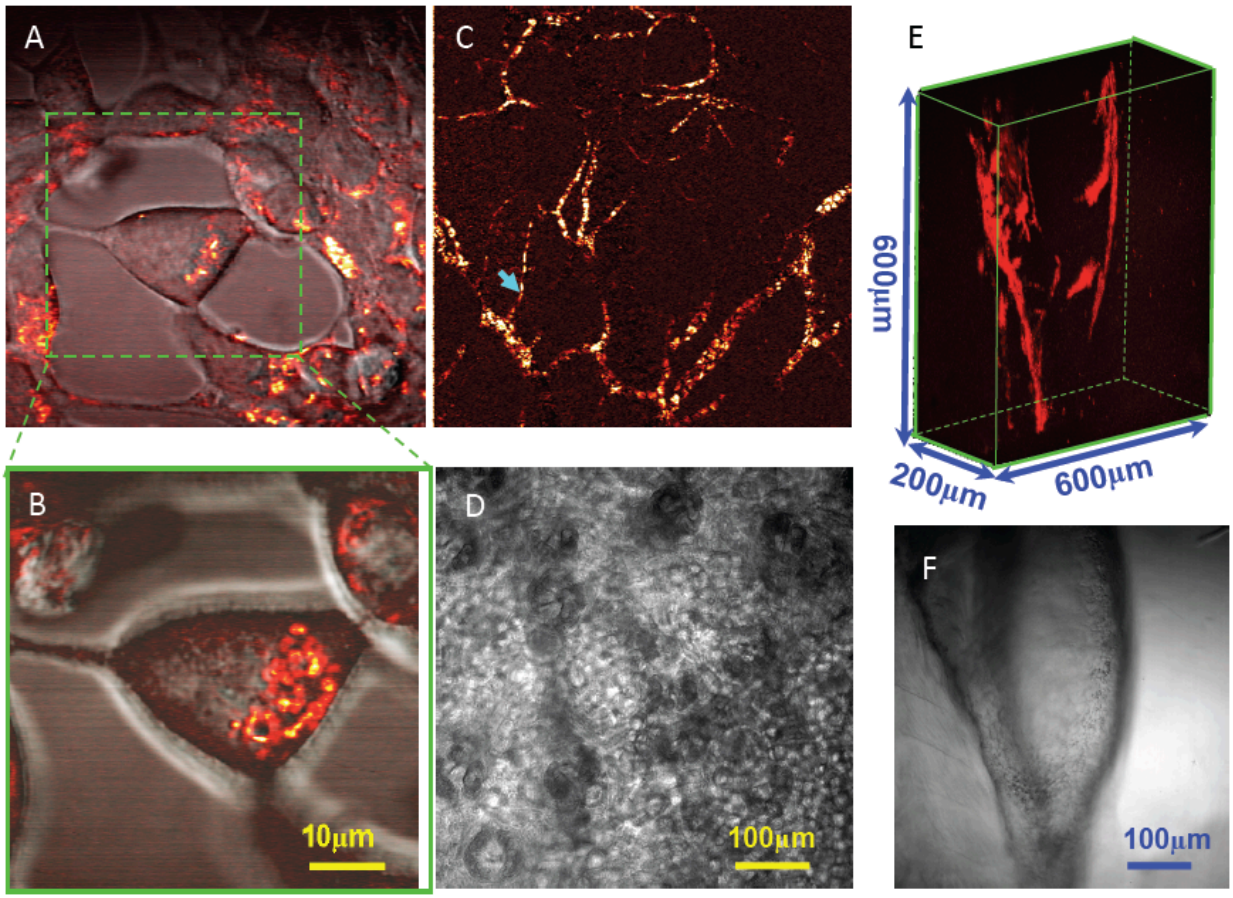

Figure 2.11 Applications of two-photon excited photothermal lens microscopy in heme protein imaging.

(A) Imaging distribution of cytochromes in live HEK-293 cells (red hot), overlapped with a transmission image of the probe beam (gray) (B) In a reduced volume scan of the indicated area in (A), individual mitochondrion can be clearly resolved label-free. (C) Imaging the microvascular network in mouse ear tissue based on hemoglobin contrast. The image shows the blood vessel network surrounding sebaceous glands. Invidual blood cells are shown to be lined up within a single capillary (<5 μm in diameter). (D) Transmission image by the CW probe beam of the same tissue region as in (C). (E) 3-D reconstruction of blood vessel network in zebrafish gill. (F) Transmission image of zebrafish gill by the CW probe beam. In all two-photon excited photothermal imaging experiments, the power of 200 fs 830 nm excitation beam and 785 nm CW probe beam are kept to be ~10 mW and ~20 mW, respectively, at the focus of the objective, with laser modulation frequency at 100 kHz and pixel dwell time ~200 μs.

From the perspective of instrumentation, this microscopy can be readily configured from a standard two-photon fluorescence microscope, which is already equipped with the two-photon excitation source. The only additional elements required are a continuous wave probe laser and a modulator/demodulator. We note that excited state absorption has recently been employed to

image hemoglobin by using two synchronized femtosecond lasers (Fu et al., 2007), which is however technically more complex and expensive.

To summarize, two-photon excited photothermal lens microscopy enables label-free high-resolution imaging of heme protein in live cells, tissues and organisms with intrinsic 3D optical sectioning and high sensitivity. The technique opens up further possibilities of functional imaging of heme proteins such as the oxygenation level of hemoglobin and redox state dynamics of cytochromes both in cellular and tissue/organism levels.

2.3 Materials and Methods

2.3.1 Detailed apparatus of stimulated emission microscopy

10 W solid-state 532 nm green laser (Millennia, Spectral-Physics) was used to pump a Ti-sapphire oscillator (Mira, Coherent) to produce a 2W mode-locked 100 fs 76 MHz pulse train at 830 nm. This pulse train was then split and used to synchronously pump two fs optical parametric oscillators (OPOs) simultaneously: the first OPO's (Mira-OPO basic, Coherent) output wavelength was tuned by tuning the color of the pump Ti-sapphire output (under 830 nm Ti-sapphire pumping, this OPO signal wave is at 1180 nm), and the second OPO (Mira PP-OPO, Coherent) was tuned by adjusting the cavity length of the OPO (the range of the signal wave is between 1100 nm and 1400 nm).

For imaging of chromoproteins, X-gal hydrolysis product and TBO drug distributions, the first OPO output was frequency doubled outside the cavity by a BBO crystal to generate a fs pulse train around 590 nm as the excitation beam, and the second OPO was intra-cavity doubled to generate its second harmonic signal between 550 nm and 700 nm as the stimulation beam.

For imaging blood vessels, a homemade mode locked Yb pump laser and two homemade synchronously pumped OPO were used. A high power Yb laser was built to operate at 75 MHz,

~200 fs, at power levels of 10 W at a wavelength of 1040 nm. More than 60% conversion to the second harmonic generation at 520 nm was routinely achieved with an angel tuned LBO crystal at room temperature (theta = 90 degrees, phi = 13 degrees, 4 mm long, Casix). The doubled 520 nm was then used to synchronously pump two homemade OPOs, which both used temperature tuned 6 mm long LBO crystal. By changing the temperature of the crystal, the signal wave was tunable from 680 nm to 1000 nm, and the idler wave was available at wavelengths from 1080 nm to more than 2000 nm. The signal wave from the first OPO provided 830 nm beam for two photon excitation of the heme, and the idler wave (~1200 nm) from the second OPO was frequency doubled outside the cavity by a BBO crystal to generate a 200 fs pulse train ~600 nm as the stimulation beam.

For experiments with both one-photon and two-photon excitation, the excitation beam and the stimulation beam were spatially overlapped with a dichroic beam splitter. Temporal delay between two excitation and stimulation pulse trains was set with a translation delay-stage and measured with an autocorrelator (APE GmbH). The exact time zero was adjusted by optimizing the coherent anti-Stokes Raman scattering signal around 534 nm generated by the pump beam at 590 nm and Stokes beam at 660 nm.

The excitation beam was modulated by an acousto-optical modulator (AOM) (3080-122, Crystal technology) at 5 MHz which was driven by a square-wave function generator. We note that the AOM crystal added significant chirp to the pulses. To compensate for this, a pulse compressor consisting of a pair of SF11 prisms (Thorlabs) was built into the excitation beam path to control its pulse width.

Excitation and stimulation beams were coupled into a modified laser scanning inverted microscope (IX71, FV300, Olympus). The beam size was matched to fill the back-aperture of

objective. A 60X 1.2 N.A. objective (UPlanSApo, water, Olympus) was used for excitation, and a 20X 0.95 N.A. long-working distance objective (XLUMPlanFI, water, Olympus) was used as a condenser. Another lens was used to image the scanning mirrors onto a silicon amplified photo-diode (PDA36A, Thorlabs) to avoid beam movement during laser scanning. Two high OD bandpass filters (HG650/45X, Chroma Technology; Brightline fluorescence filter 655/40, Semrock) were used together to block the excitation beam completely and only transmit the stimulation beam. For imaging blood vessels, high OD filters (3RD800SP and 3RD760SP, Omega Optical) were used together to block the two-photon excitation beam completely.

The output of the photodiode was bandpass filtered (15542, DC-48MHz low-pass filter, Mini-Circuits) to suppress the strong signal at the pulsing repetition rate (76 MHz), and then terminated with 50 Ω. A high-frequency lock-in amplifier (SR844, Stanford Research) was used to demodulate the stimulated emission signal. The analog on phase component x-output of the lock-in amplifier was fed into the A/D converter of the microscope input. The time constant was set for 1 sec and 100 μs under spectroscopy and microscopy experiments, respectively. Images were acquired with a pixel dwell time of 190 μs.

2.3.2 Detailed apparatus of two photon excited photothermal microscopy

The two-photon excitation beam for heme proteins (200 fs 830 nm laser) was generated using the same method as in stimulated emission microscopy. The power of the excitation beam at the focus was reduced to less than 10mW to avoid photodamage. The excitation beam and the cw probe laser beam (785 nm, Sacher Lasertechnik, TEC510-785) were spatially overlapped using a dichroic beam mirror. The excitation beam was modulated by an acoustio-opitcal modulator (AOM) (model 3080-122, Crystal technology) at 100 kHz driven by a square-wave function generator.

Excitation and probe beams were coupled into a modified laser scanning inverted microscope (IX71, FV300, Olympus). The beam size was adjusted to fill the back-aperture of the objective. A 60X 1.2 N.A long-working distance objective (UPlanSApo, water, Olympus) was used for excitation for all cell imaging (red blood cells and HEK-293 cells); A 20X 0.75 N.A objective (UPlanSApo, air, Olympus) was used for excitation for all tissue imaging (mouse ear vessels and the zebrafish gill). A 20X 0.95 N.A. long-working distance objective (XLUMPlanFI, water, Olympus) was used as the condenser. Another lens after the condenser was used to collect the transmitted probe beams onto a silicon amplified photodiode (PDA36A, Thorlabs) during laser scanning. Two high-OD lowpass filters (3RD800SP, Omega) were used together to block the excitation beam completely and only transmit the probe beam. An iris diaphram with an adjustable aperture was mounted on a two dimensional translational stage and placed in the probe beam path.

The output of the photodiode was lowpass filtered (DC-1.9MHz, Mini-circuits) and terminated into 50 Ω. A high-frequency lock-in amplifer (SR844, Stanford Rserach) was used to demodulate the photothermal signal. The analog on phase component x-output of the lock-in amplifier was fed into the A/D converter of the microscope input. Time constant was 100 μs for all the imaging experiments. 200 μs pixel dwell time was used in collecting all the images. It took ~13 seconds for a 256-pixel-and-256-pixel image.

2.3.3 Stimulated emission spectrum

High purity crystal violet powder was used as purchased (Sigma-Aldrich). Aqueous solutions were prepared with deionized water. The absorption spectrum was taken under a spectrophotometer (DU 800, Beckman Coulter). The absolute concentrations of crystal violet in the solutions were determined through their absorbance at 590 nm. In order to measure

stimulated emission spectroscopy, we built a flow-cell from two No.1 coverslips and a spacer (~130 μm) to allow quick concentration exchange without moving the sample position or focusing depth inside the sample.

2.3.4 Bacterial genetic constructs

Chromoprotein gtCP was expressed in the DH10B *E. coli* using pQE30 expression vector without induction. After cell growth in LB medium at 37 °C to A_{600} of 0.6, the culture was moved to 22°C shaker for 24-36 hrs to ensure complete maturation of the chromophore. cjBLUE was overexpressed from a pRSETB vector in BL21(DE3) *E. coli* cells. After growth in LB at 37 °C, expression was induced with 1 mM IPTG at A_{600} of 0.6 and moved to 22 °C shaker for 36-48 hrs. Wild-type *E. coli* cells were incubated with 50 μM X-gal solution in 37ºC for 30 min, and then concentrated and sandwiched between two No. 1 coverslips. No inducer for *lacZ* gene was added.

2.3.5 Sample preparation for mammalian cell imaging

Human embryonic kidney (HEK) 293 cell line was obtained from American Type Culture Collection (ATCC, Rockville), HEK 293 cells were maintained in Dulbecco's Modified Eagle's Medium (ATCC) supplemented with 10% fetal bovine serum (ATCC) at 37 ºC in a humidified 5% CO_2 air incubator. Cells were cultured on uncoated glass bottom dishes (P35G-1.0-14-C, MatTek Cooperation).

Toluidine blue O (TBO) was used as purchased (Sigma-Aldrich). The HEK 293 cells were incubated in 10 μM TBO in phosphate buffer saline (21-040-CV, Mediatech) for one hour before being imaged for TBO drug distribution. In order to image cytochromes in HEK 293 cells, the growth medium was replaced with phosphate buffer saline during imaging to avoid autofluorescence from the growth medium.

2.3.6 Sample preparation for animal tissue imaging

Mouse skin tissue from wild-type white mice was obtained from Harvard Mouse Facility. Thin ear was harvested immediately after sacrificing the mouse. In order to image the micro-vascular network in mouse ear tissue based on hemoglobin contrast, the fresh ear was sandwiched between two No.1 coverslips with a drop of water on top. In order to image drug distribution in the skin, ~25 μl of 10 μM TBO in phosphate buffer saline was pipetted onto a 5X5 mm area on the skin surface, incubated at 37 ºC with saturating humidity for one hour. The whole ear tissue was then placed between two No. 1 coverslips for imaging.

Zebrafish ruby mutant was obtained from Harvard MCB Zebrafish Facility. The larval zebrafish was euthanized 7 days after fertilization. Immediately after euthanization, the fish was trapped in methyl cellulose and sandwiched between two No.1 coverslips with a drop of water on top for imaging. The fish was placed with one side facing the objective.

References

Bialkowski, S.E. (1996). Photothermal Spectroscopy Methods for Chemical Analysis (John Wiley & Sons).

Boyer, D., Tamarat, P., Maali, A., Lounis, B., and Orrit, M. (2002). Photothermal imaging of nanometer-sized metal particles among scatterers. Science *297*, 1160-1163.

Brusnichkin, A.V., Nedosekin, D.A., Proskurnin, M.A., and Zharov, V.P. (2007). Photothermal lens detection of gold nanoparticles: Theory and experiments. Appl Spectrosc *61*, 1191-1201.

Cai, L., Friedman, N., and Xie, X.S. (2006). Stochastic protein expression in individual cells at the single molecule level. Nature *440*, 358-362.

Cantor, C.R., and Schimmel, P.R. (1980). Biophysical Chemistry (W.H. Freeman).

Chan, M.C.Y., Karasawa, S., Mizuno, H., Bosanac, I., Ho, D., Prive, G.G., Miyawaki, A., and Ikura, M. (2006). Structural characterization of a blue chromoprotein and its yellow mutant from the sea anemone Cnidopus japonicus. J Biol Chem *281*, 37813-37819.

Chelvanayagam, D.K., and Beazley, L.D. (1997). Toluidine blue-O is a Nissl bright-field counterstain for lipophilic fluorescent tracers Di-ASP, DiI and DiO. J Neurosci Meth *72*, 49-55.

Clay, G.O., Schaffer, C.B., and Kleinfeld, D. (2007). Large two-photon absorptivity of hemoglobin in the infrared range of 780-880 nm. Journal of Chemical Physics *126*.

Cognet, L., Tardin, C., Boyer, D., Choquet, D., Tamarat, P., and Lounis, B. (2003). Single metallic nanoparticle imaging for protein detection in cells. Proc Natl Acad Sci USA *100*, 11350-11355.

Denk, W., Strickler, J.H., and Webb, W.W. (1990). Two-photon laser scanning fluorescence microscopy. Science *248*, 73-76.

Detmer, S.A., and Chan, D.C. (2007). Functions and dysfunctions of mitochondrial dynamics. Nat Rev Mol Cell Biol *8*, 870-879.

Dong, C.Y., So, P.T.C., French, T., and Gratton, E. (1995). Fluorescence lifetime imaging by asynchronous pump-probe microscopy. Biophys J *69*, 2234-2242.

Du, H., Fuh, R.C.A., Li, J.Z., Corkan, L.A., and Lindsey, J.S. (1998). PhotochemCAD: A computer-aided design and research tool in photochemistry. Photochem Photobiol *68*, 141-142.
Einstein, A. (1917). On the quantum theory of radiation. Phys Z *18*, 121-128.

Evans, C.L., and Xie, X.S. (2008). Coherent Anti-Stokes Raman Scattering Microscopy: Chemical Imaging for Biology and Medicine. Annu Rev Anal Chem *1*, 883-909.

Freudiger, C.W., Min, W., Saar, B.G., Lu, S., Holtom, G.R., He, C.W., Tsai, J.C., Kang, J.X., and Xie, X.S. (2008). Label-Free Biomedical Imaging with High Sensitivity by Stimulated Raman Scattering Microscopy. Science *322*, 1857-1861.

Fu, D., Ye, T., Matthews, T.E., Chen, B.J., Yurtserver, G., and Warren, W.S. (2007). High-resolution in vivo imaging of blood vessels without labeling. Opt Lett *32*, 2641-2643.

Grinvald, A., Lieke, E., Frostig, R.D., Gilbert, C.D., and Wiesel, T.N. (1986). Functional Architecture of Cortex Revealed by Optical Imaging of Intrinsic Signals. Nature *324*, 361-364.

Gurskaya, N.G., Fradkov, A.F., Terskikh, A., Matz, M.V., Labas, Y.A., Martynov, V.I., Yanushevich, Y.G., Lukyanov, K.A., and Lukyanov, S.A. (2001). GFP-like chromoproteins as a source of far-red fluorescent proteins. FEBS Lett *507*, 16-20.

Hamilton, C.E., Kinsey, J.L., and Field, R.W. (1986). Stimulated-Emission Pumping - New Methods in Spectroscopy and Molecular-Dynamics. Annu Rev Phys Chem *37*, 493-524.

Hell, S.W., and Wichmann, J. (1994). Breaking the Diffraction Resolution Limit by Stimulated-Emission - Stimulated-Emission-Depletion Fluorescence Microscopy. Opt Lett *19*, 780-782.

Jiang, X.J., and Wang, X.D. (2004). Cytochrome C-mediated apoptosis. Annu Rev Biochem *73*, 87-106.

Kleinfeld, D., Mitra, P.P., Helmchen, F., and Denk, W. (1998). Fluctuations and stimulus-induced changes in blood flow observed in individual capillaries in layers 2 through 4 of rat neocortex. Proc Natl Acad Sci USA *95*, 15741-15746.

McDonald, D.M., and Choyke, P.L. (2003). Imaging of angiogenesis: from microscope to clinic. Nat Med *9*, 713-725.

Miller, J.H. (1972). Experiments in Molecular Genetics (New York: Cold Spring Harbor Laboratory).

Moerner, W.E., and Kador, L. (1989). Optical-Detection and Spectroscopy of Single Molecules in a Solid. Phys Rev Lett *62*, 2535-2538.

Rittweger, E., Rankin, B.R., Westphal, V., and Hell, S.W. (2007). Fluorescence depletion mechanisms in super-resolving STED microscopy. Chem Phys Lett *442*, 483-487.

Seigman, A.E. (1986). Lasers (University Science Books).

Stein, E.W., Maslov, K., and Wang, L.V. (2009). Noninvasive, in vivo imaging of blood-oxygenation dynamics within the mouse brain using photoacoustic microscopy. J Biomed Opt *14*, 020502.

Stoletov, K., Montel, V., Lester, R.D., Gonias, S.L., and Klemke, R. (2007). High-resolution imaging of the dynamic tumor cell-vascular interface in transparent zebrafish. Proc Natl Acad Sci USA *104*, 17406-17411.

Tokeshi, M., Uchida, M., Hibara, A., Sawada, T., and Kitamori, T. (2001). Determination of Subyoctomole Amounts of Nonfluorescent Molecules Using a Thermal Lens Microscope: Subsingle-Molecule Determination. Anal Chem *73*, 2112-2116.

Tremblay, J.F., Dussault, S., Viau, G., Gad, F., Boushira, M., and Bissonnette, R. (2002). Photodynamic therapy with toluidine blue in Jurkat cells: cytotoxicity, subcellular localization and apoptosis induction. Photoch Photobio Sci *1*, 852-856.

Turro, N.J. (1991). Modern Molecular Photochemistry (University Science Books).

Wang, W., Ye, X., Demidov, A.A., Rosca, F., Sjodin, T., Cao, W.X., Sheeran, M., and Champion, P.M. (2000). Femtosecond multicolor pump-probe spectroscopy of ferrous cytochrome c. J Phys Chem B *104*, 10789-10801.

Ye, J., Ma, L.S., and Hall, J.L. (1998). Ultrasensitive detections in atomic and molecular physics: demonstration in molecular overtone spectroscopy. J Opt Soc Am B *15*, 6-15.

Zhang, J., Campbell, R.E., Ting, A.Y., and Tsien, R.Y. (2002). Creating new fluorescent probes for cell biology. Nat Rev Mol Cell Bio *3*, 906-918.

Chapter 3

Detection of single-molecule optical absorption at room temperature with ground-state depletion microscopy

Optical studies of single molecules in ambient environments, which have led to broad applications, are primarily based on fluorescence detection. Direct detection of optical absorption with single-molecule sensitivity at room temperature is difficult because absorption is not a background-free measurement and is often complicated by sample scattering. In this chapter, we present ground-state depletion microscopy for ultrasensitive detection of absorption contrast. We image 20 nm gold nanoparticles as an initial demonstration of this microscopy. We then demonstrate the detection of an absorption signal from a single chromophore molecule at room temperature. This is accomplished by using two tightly focused collinear continuous-wave laser beams at different wavelengths, both within a molecular absorption band, one of which is intensity modulated at a high frequency (>MHz). The transmission of the other beam is found to be modulated at the same frequency due to ground-state depletion. The signal of single chromophore molecules scanned across the common laser foci can be detected with shot-noise limited sensitivity. This measurement represents the ultimate detection sensitivity of nonlinear optical spectroscopy at room temperature.

3.1 Background

Single molecule optical detection, imaging and spectroscopy have made an impact on many disciplines (Moerner and Orrit, 1999; Selvin and Ha, 2008; Weiss, 1999; Xie et al., 2008; Xie and Trautman, 1998). In particular, room temperature optical detection of single molecules has been applied extensively to biological research (Selvin and Ha, 2008; Weiss, 1999; Xie et al., 2008). Single molecule optical detection at room temperature dates back to 1976 when Hirschfeld reported the use of an optical microscope to reduce probe volume, hence background signal (Hirschfeld, 1976). He was able to detect individual immobilized protein molecules labeled with tens of fluorophores, demonstrating a single-molecule line-scan image. Similar use of optical microscopes finally allowed single fluorophore sensitivity at room temperature in 1990 (Rigler and Widengren, 1990; Shera et al., 1990). It has remained the method of choice for detecting and imaging single molecules in ambient environments until the present.

Among methods subsequently emerged, the first single chromophore detection was achieved by optical absorption measurement at 1.6 K with a sophisticated frequency modulation scheme in 1989 (Moerner and Kador, 1989). This measurement relied on the large absorption cross-section of the zero-phonon line. It was soon followed by fluorescence detection via excitation at the zero-phonon lines, which offered much higher sensitivity by virtue of background free emission detection (Orrit and Bernard, 1990). These methods, however, were limited only to cryogenic temperatures at which zero phonon lines exist for a handful of molecules.

Imaging of single fluorophores at room temperature was first accomplished with near-field microscopy in 1993 (Betzig and Chichester, 1993). Though a seminal contribution, near-field single molecule imaging had limited applications because of the complexity and perturbation of

the near-field probes, and was soon superseded by far-field single molecule imaging with total internal reflection (Funatsu et al., 1995) and confocal microscopy (Macklin et al., 1996).

Surface enhanced Raman scattering is capable of detecting single molecules (Kneipp et al., 1997; Nie and Emery, 1997), but it requires close contact of molecules with a metal nanostructure, which is difficult to control. High sensitivity measurements towards single molecule spectroscopy have been attempted with other contrast besides fluorescence and Raman scattering, including interferometry (Hwang et al., 2006; Kukura et al., 2009), stimulated emission (Min et al., 2009), photothermal (Boyer et al., 2002; Uchiyama et al., 2000) and direct absorption measurement (Kukura et al., 2010). The photothermal method has recently reached single molecule sensitivity, however, glycerol has to be used in order to reduce heat conductivity and increase the refractive index change induced by single molecule light absorption (Gaiduk et al., 2010a). The direct absorption method has been recently demonstrated single molecule sensitivity (Kukura et al., 2010). By careful selection of the sample substrate, the authors avoided the major complication of sample scattering for direct absorption measurements. We seek a different approach for detection of single-molecule optical absorption at room temperature.

Recently several nonlinear optical imaging techniques including stimulated Raman scattering microscopy (Freudiger et al., 2008), two-photon absorption microscopy (Fu et al., 2007a) and stimulated emission microscopy (Min et al., 2009) have been developed for imaging non-fluorescent species. The nonlinearity of these techniques allows 3D optical sectioning. The techniques use two pulse laser trains of different wavelengths, which coincide in the sample. The first beam is intensity modulated at a high frequency (>MHz), while the second beam is monitored by a photodetector via phase sensitive detection with a lock-in amplifier. As a result of nonlinear interactions between the two laser beams and the sample, the transmission of the

second beam is modulated at the same frequency as the first beam. The high-frequency modulation transfer method effectively circumvents laser intensity fluctuations and the intensity variation of a transmitted laser beam that is scanned across a heterogeneous sample, both of which occur at low frequencies (DC to kHz). Here we demonstrate ground-state depletion microscopy with continuous wave (CW) lasers, which offers single-molecule sensitivity for detection of optical absorption, and is free from sample scattering complications.

3.2 Results and Discussion

3.2.1 Principle of ground-state depletion microscopy

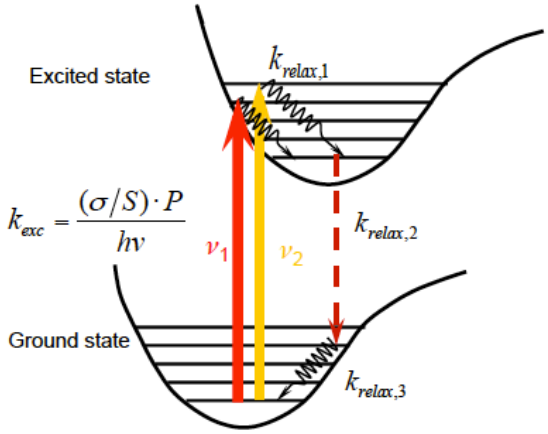

Figure 3.1 Energy diagram for optical absorption, excited state relaxation and ground-state depletion of a molecule.

Laser fields ν_1 and ν_2 are both on resonance with the absorption of the molecule. One beam affects the absorption of the other beam by depleting the ground state of the molecule.

Consider a ground state and an excited state of a molecule (Figure 3.1), the power of the incident beam P is attenuated by the single molecule at the laser focus by approximately (see Methods and Materials for derivation)

$$\Delta P = \frac{k_{relax}\cdot(\sigma/S)\cdot P}{k_{relax} + (\sigma/h\nu S)\cdot P} \tag{3.1}$$

where k_{relax} is the $k_{relax,2}$ (Figure 3.1), which is the rate constant of the rate-limiting step in the sequential relaxation process from the vibronic states prepared by the optical excitation to the lowest vibrational level in the ground electronic state, hv is the photon energy, σ is the absorption cross-section for a single chromophore (~ 10^{-16} cm^2 at room temperature), and S is the beam waist area (~10^{-9} cm^2). The relative light attenuation, $\Delta P/P$, is no more than 10^{-7}~10^{-6} for a single molecule at room temperature. Conventional single-beam absorption microscopy cannot detect such a small attenuation, as it would be buried in the laser intensity noise (~1%). Moreover, Rayleigh scattering due to the inhomogeneous refractive index of the sample also contributes to the attenuation, the magnitude of which is highly sample-dependent.

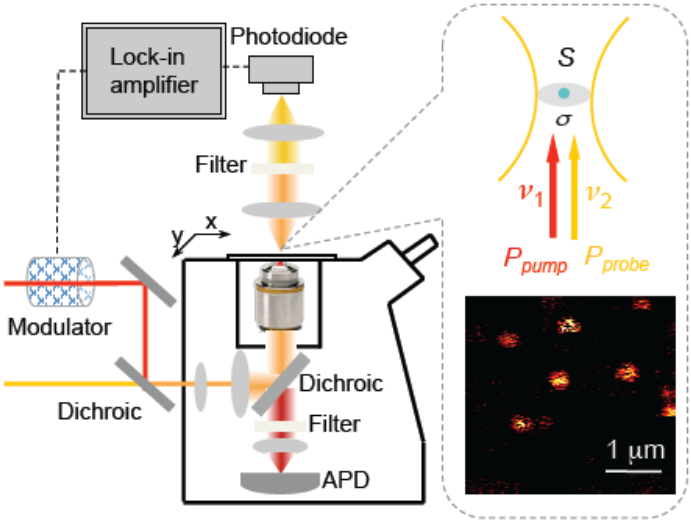

Figure 3.2 Experimental setup for the simultaneous ground-state depletion and epi-fluorescence detection.

The inset indicates single molecule absorption cross section σ and the cross section of a tightly focused laser beam *S*. It also shows a fluorescence image of single molecule Atto647N embedded in PMMA.

We employ the modulation transfer detection scheme to measure ground-state depletion in a pump-probe experiment (Figures 3.1&3.2). Two CW lasers, a pump beam at frequency ν_1 and a probe beam at frequency ν_2, are both on resonance with the same absorption band of the

molecule. The incident power levels of pump and probe beams, P_{pump} and P_{probe}, are adjusted to be near the saturation intensity of the absorption transition. We modulate the incident intensity of the pump beam ν_1 at 1.75 MHz, and keep the incident intensity of the probe beam ν_2 constant (Figure 3.3). The collinearly propagating pump and probe beams are focused to a common spot. The sample is scanned across the fixed laser foci with a piezoelectric scanning stage (Figure 3.2). After passing through the sample, the transmitted probe beam is detected by a photodiode while the pump beam is blocked by a filter. The photodiode signal is demodulated by a lock-in amplifier to create the ground-state depletion contrast. The modulation depth of the transmitted probe beam is,

$$\delta\delta P_{probe} = \frac{2k_{relax}\cdot(\sigma^2/S^2\,h\nu)\cdot P_{pump}P_{probe}}{\left(k_{relax}+(\sigma/h\nu S)\cdot P_{probe}\right)\cdot\left(k_{relax}+(\sigma/h\nu S)\cdot(2P_{pump}+P_{probe})\right)} \qquad (3.2)$$

(see Methods and Materials for derivation). For simplicity, in Eq. 3.2 we use the absorption cross-section σ and laser frequency ν that correspond to the average of pump and probe wavelengths, which are on resonance with the same molecular absorption band. We note this is an approximation due to the difference between pump and probe wavelengths and the existence of laser line width.

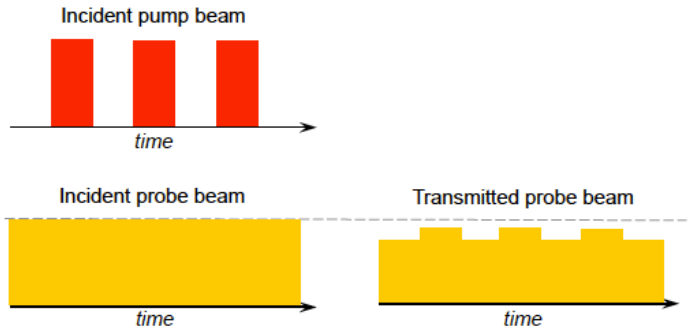

Figure 3.3 Schematic diagram of modulation transfer based on ground-state depletion.
As the intensity of the pump beam is modulated on and off over time, the probe beam is also modulated at the same frequency.

3.2.2 Imaging gold nanoparticles with ground-state depletion microscopy

As an initial demonstration of ground-state depletion microscopy, we imaged individual 20 nm gold nanoparticles dispersed on a glass surface (Figure 3.4), whose absorption spectrum is shown in Figure 3.5 with the pump and probe wavelengths labeled. The power level at focus was 450 μW for each beam. The pixel dwell time was 6.5 ms and the time constant of the lock-in amplifier was set as 3 ms. Figure 3.6 shows the diffraction-limited intensity profile for a single nanoparticle in the inset image, which reveals a signal of $\delta\delta P/P \sim 0.5\times10^{-4}$, where P refers to the probe beam power at the photodiode. We assign the signal detected to ground-state depletion.

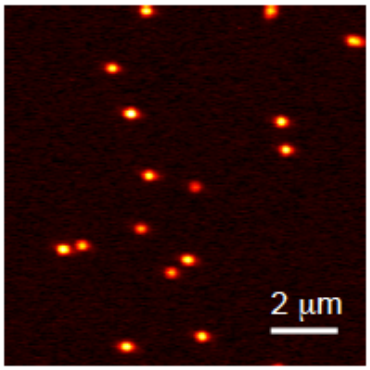

Figure 3.4 Ground-state depletion imaging of single 20 nm gold nanoparticles.

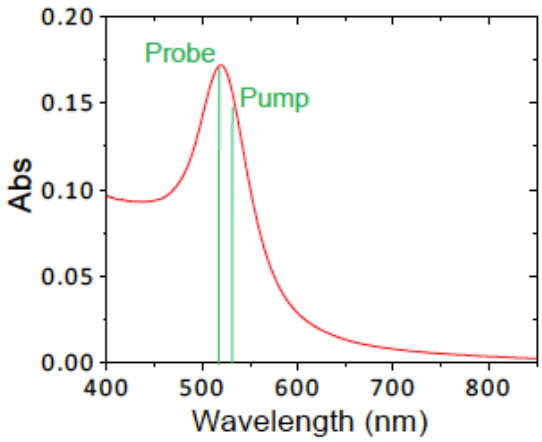

Figure 3.5 Ensemble absorption spectrum of 20 nm gold nanoparticles in aqueous solution. The wavelengths of pump beam (532 nm) and probe beam (520 nm) are indicated.

This assignment is supported by a calculation of the ground-state depletion signal for a single gold nanoparticle. The absorption cross section of a 20 nm gold nanoparticle at its plasmon resonance is ~4×10^{-12} cm^2 (Berciaud et al., 2006). Time-resolved measurement shows that the bleached ground state recovers sequentially through a fast electron-phonon relaxation (1~4 ps) (Ahmadi et al., 1996; Hodak et al., 1998) and a slow phonon-phonon relaxation (~100 ps) (Hodak et al., 1998). The ground state recovery kinetics has been shown to be biexponential with the slow component having ~10% weight (Ahmadi et al., 1996). Under the condition of our continuous wave excitation, the signal $\delta\delta P/P$ for a single gold nanoparticle is estimated to be ~1×10^{-4} (see Methods and Materials for the calculation). This theoretical estimation is comparable to our measured signal of $\delta\delta P/P \sim 0.5\times 10^{-4}$ (Figure 3.6).

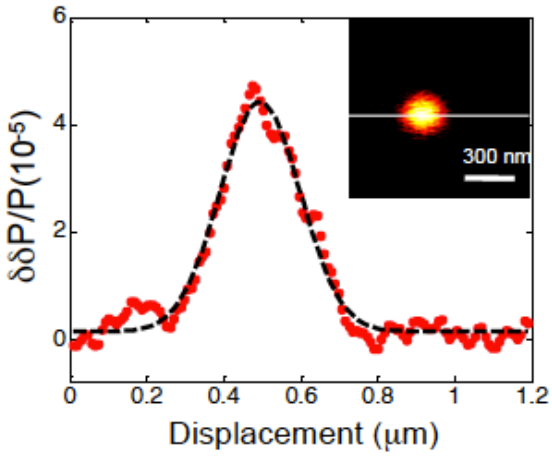

Figure 3.6 Signal intensity profile of a single nanoparticle.
The inset is the ground-state depletion image of the nanoparticle whose signal intensity profile is plotted. The lateral position of is indicated in the x-axis.

An alternative explanation for the observed contrast is the photothermal effect, which has been used to image single gold nanoparticles (Berciaud et al., 2006; Gaiduk et al., 2010b). It gives rise to refractive index variation at the laser foci, which could change the transmission of the probe beam while the pump beam is modulated, causing an apparent modulation transfer. However, the photothermal effect is known to increase with a decreasing modulation frequency

due to more heat accumulated (Berciaud et al., 2006). We found instead that our signal level is independent of modulation frequency (see Methods and Materials). In addition, the thermal lens, when measured with modulation transfer, usually exhibits a 180° signal phase change as the position of the laser focus is scanned in the longitudinal direction (Fu et al., 2008; Mian et al., 2002). We found the signal is always in phase with the pump beam in a z-scan experiment. For these reasons, photothermal effects cannot explain the data in Figure 3.4&3.6.

3.2.3 Detection of optical absorption from a single molecule at room temperature

For detecting single molecule absorption, we use an organic dye Atto647N whose absorption spectrum is shown in Figure 3.7. Wavelengths for pump and probe are 642 nm and 633 nm respectively. Epifluorescence emitted by the molecule is collected in a confocal mode.

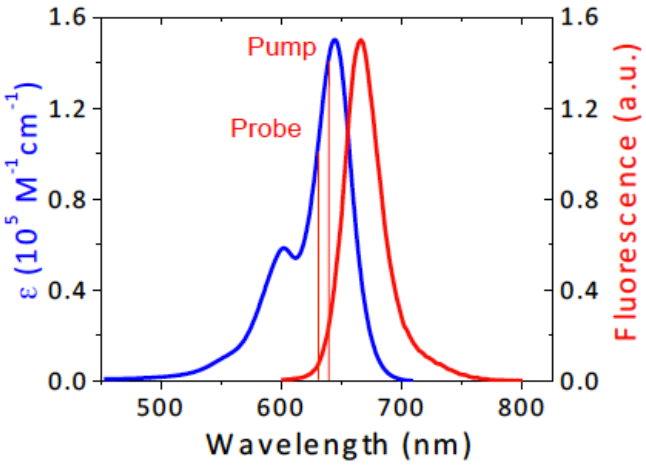

Figure 3.7 Ensemble absorption and emission spectra of Atto647N in pH 7 aqueous solution. The wavelengths of pump and probe beams are indicated.

The power dependence and sensitivity of ground-state depletion microscopy were characterized with an aqueous solution of Atto647N in pH 7 phosphate buffer. At low excitation intensity, Eq. 3.2 approaches

$$\delta\delta P = \frac{(2\sigma^2 / S^2 h\nu)\cdot P_{pump} P_{probe}}{k_{relax}}. \qquad (3.3)$$

The inset of Figure 3.8 shows the signal from an ensemble is linearly dependent on the product of pump and probe beam powers at low excitation intensities, consistent with Eq. 3.3. However, above saturation intensities, the linear curve becomes sublinear (Figure 3.8). Note that the overall quadratic power dependence under non-saturating conditions would allow 3D optical sectioning, as in many other multiphoton techniques (Denk et al., 1990; Min et al., 2009).

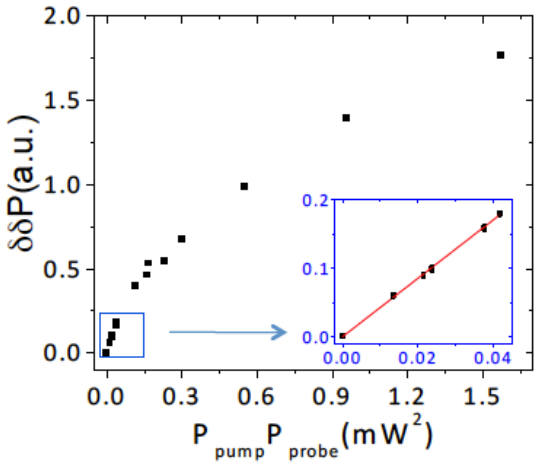

Figure 3.8 Ground depletion signal from aqueous solution of Atto647N as a function of the product of pump and probe beam power.

The concentration of Atto647N is 0.84 μM. The blue frame indicates the linear portion of the function. The inset is zoom-in of the blue frame.

Figure 3.9 shows that the ground-state depletion signal depends linearly on the concentration of Atto647N solution. This allows straightforward quantitative analysis. The best sensitivity is achieved under the condition that both pump and probe beams have near-saturation intensity levels, in our case, 350 μW for each beam at the focus. All further measurements were conducted at this power level. The detection limit is 9 nM with 1s integration time, which corresponds to 0.2 molecule in the probe volume (~3×10^{-17} liter) (Diaspro et al., 2005). The corresponding modulation depth, $\delta\delta P/P$, of a single Atto647N molecule is ~1.4×10^{-7}. Note that the P in

$\delta\delta P/P$ indicates the probe beam power at the photodiode. This measured result agrees with its theoretical value ~1.2×10^{-7} based on Eq. 3.2 (see Methods and Materials for the calculation).

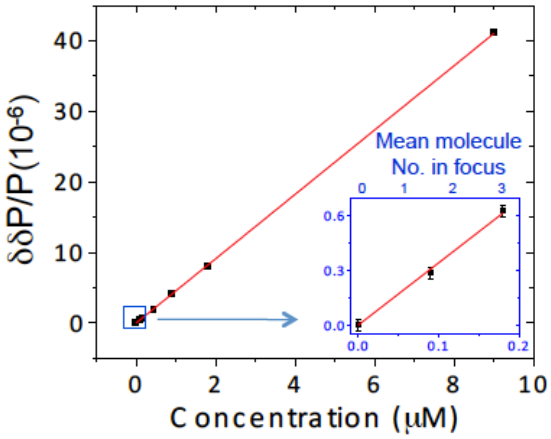

Figure 3.9 Ground-state depletion signal as a function of concentration of aqueous Atto647N solution.

The power level is 350 μW for each beam. The blue frame indicates the data points at lowest concentrations. The inset is zoom-in of the blue frame, with concentrations labeled at the bottom and estimated mean molecule numbers in the probe volume labeled at the top. Error bars are for 1s integration time, indicating that single-molecule sensitivity is reachable.

The inset of Figure 3.2 depicts a fluorescence image of single-molecule Atto647N embedded in PMMA matrix. The blinking of fluorescence and one-step photobleaching clearly proves that the spot is from a single molecule. Lateral line scans across the maximum of the diffraction-limited spot were repeated, the ground-state depletion and epifluorescence signals were recorded simultaneously. The time constant of the lock-in amplifier was 30 ms.

Figures 3.10A-D show the simultaneous line-scan signals of fluorescence and absorption of two single molecules. For Molecule A, the fluorescence line scan signal as a function of time is shown in the inset of Figure 3.10A. It survived for 45 line scans before photobleaching (longer than the average survival lines of a single molecule, see Methods and Materials). The red plots in Figures 3.10A&B show the average of 45 fluorescence and absorption line-scan signals before Molecule A was photobleached. The lateral position of the peak value $\delta\delta P/P$ ~1.4×10^{-7}

coincides with the peak position in the single molecule fluorescence line scan. This demonstrates the single-molecule sensitivity of the ground-state depletion microscope. The blue plot in Figure 3.10B shows that after Molecule A was photobleached, the average of 45 absorption line-scan signals vanished. The detection of the absorption signal is shot-noise limited because the noise in Figure 3.10B is consistent with the estimated normalized shot noise $\Delta P/P \sim 3\times10^{-8}$ at the probe beam power used (see Methods and Materials for the calculation). Similar data for another molecule is shown in Figures 3.10C&D.

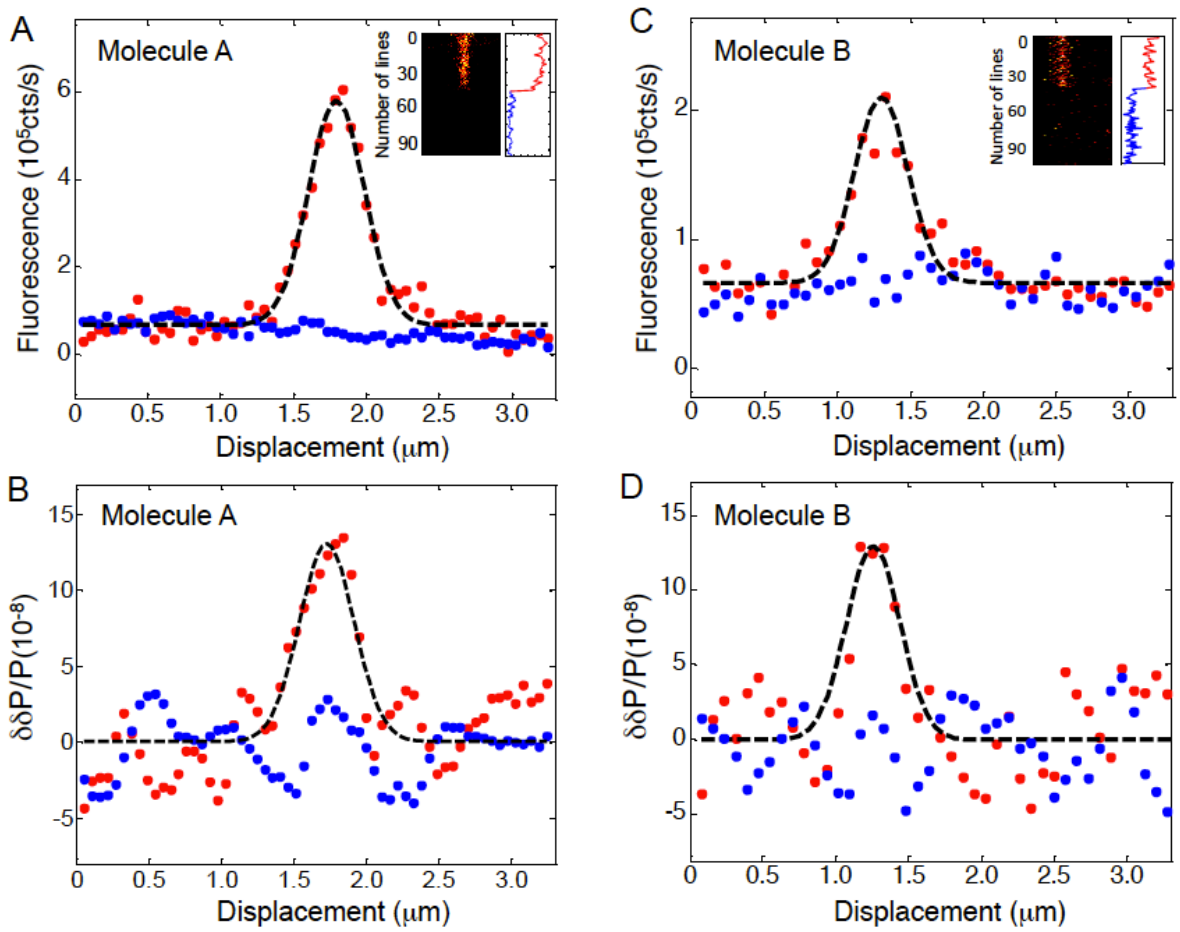

Figure 3.10 Fluorescence and absorption line scans of individual immobilized Atto647N molecules.

(A) Fluorescence line scans for Molecule A, averaged from the inset before (red) and after (blue) photobleaching. The inset is the fluorescence image constructed from repeated line scans across Molecule A and the corresponding fluorescence intensity trajectory. The molecule is photobleached after 45 line scans (39 ms per pixel). (B) Absorption line scans for Molecule A, averaged before (red) and after (blue) photobleaching, simultaneously recorded with (A). (C) Fluorescence line scans for Molecule B, averaged from inset before (red) and after (blue) photobleaching. The inset is the fluorescence image constructed from repeated line scans across Molecule B and the corresponding fluorescence intensity trajectory. The molecule is photobleached after 44 line scans (78 ms per pixel). (D) Absorption line scans for Molecule B, averaged before (red) and after (blue) photobleaching, simultaneously recorded with (C).

We note that ground-state depletion is not the only possible modulation transfer mechanism that could exist in such a pump-probe experiment. Excited-state absorption, stimulated emission and photothermal effects might also cause intensity modulation of the probe beam. We were able to exclude excited-state absorption as the underlying mechanism by finding that our signal is in

phase with the pump beam, since there is a 180^{o} phase difference between the excited-state absorption signal and the pump beam modulation (Fu et al., 2007b).

Stimulated emission would have the same phase as the ground-state depletion signal on the lock-in amplifier (Min et al., 2009). However, the probe wavelength is chosen to be shorter than the pump wavelength and is at the far edge of the emission spectra (Figure 3.7). We expect the contribution of stimulated emission to the modulation depth of the transmitted probe beam to be ~4%, which is estimated from the ratio of the stimulated emission cross-section at the probe wavelength to the absorption cross-section.

Our observed modulation transfer signal could also originate from the photothermal effect. Again, we exclude this by finding that our signal level is independent of modulation frequency for Atto647N detection and that the signal is always in phase with the pump beam in a z-scan experiment (see Methods and Materials).

In Figure 3.11 we report the distribution of absorption signal from 130 molecules that survive more than 20 line scans. The single-molecule absorption signals $\delta\delta P/P$ are found to range from 4×10^{-8} to 2.6×10^{-7}, with a mean of 1.1×10^{-7}. This agrees well with the theoretical value expected from Eq. 3.2 (Figure 3.11). The variation of $\delta\delta P/P$ can be explained by the random orientation of absorption dipole moments and the inhomogeneity of the single-molecule absorption spectrum.

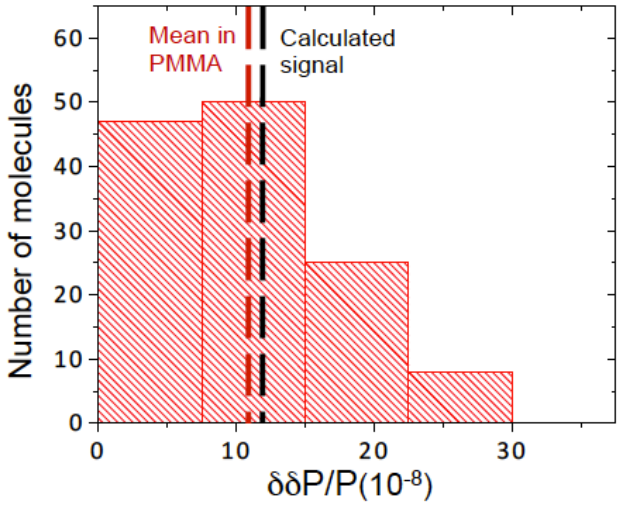

Figure 3.11 Occurrence of absorption signals from 130 single Atto647N molecules.
The mean is close to the theoretical value expected from Eq. 3.2.

3.3 Conclusion

The phenomena of ground-state depletion or nonlinear saturation spectroscopy have previously been used for achieving super resolution in fluorescence microscopy (Gustafsson, 2005; Hell and Kroug, 1995). Here we employ it in a different way to provide a high-sensitivity contrast mechanism based on optical absorption, which is free from the complication of Rayleigh scattering of the sample. In conclusion, a high-frequency dual-beam modulation transfer scheme allows the ultimate sensitivity of nonlinear optical microscopy based on saturation spectroscopy: the detection of single-molecule absorption signal at room temperature.

The detection of single-molecule absorption signal in the current work requires a few seconds of integration, which cannot yet satisfy the temporal resolution that is usually needed for detecting biological events at the single-molecule level. Nevertheless, with further improvement of its detection sensitivity, single-molecule absorption microscopy may be promising to open a new chapter of single-molecule biophysics, which is label-free.

3.4 Materials and Methods

3.4.1 Detailed apparatus of ground-state depletion microscopy

For detection of 20 nm gold nanoparticles, a solid-state laser (Laser Quantum, Ventus VIS 532) at 532 nm is used as the pump beam and a line of an Argon-Krypton laser (MellesGriot, 643-AP-A01) at 520 nm is used as the probe beam. The polarizations of both lasers are parallel with each other. The intensity of the pump beam is modulated by an acoustic optical modulator (AOM, Crystal Technology, 3080-197) at 1.75 MHz. After spatially combination with a 50/50 beam splitter, the pump and probe beams collinearly propagate into an inverted microscope (Nikon, TE300). Both beams are focused to a common focal spot in the sample by a microscope objective (Olympus UPLANSAPO 100X, N.A.=1.4). After passing through the sample, the transmitted probe beam is collected by another objective (Olympus TIRF, oil, 60X, N.A.=1.45). While the pump beam is blocked by two bandpass filters (Semrock, FF01-520/15-25 and Chroma, ET510/25), the probe beam is detected by a photodiode (Thorlabs, PDA36A) operated at 10dB gain with a bandwidth of 0 ~ 5.5 MHz. The output of the photodiode is filtered through a low pass filter (Mini Circuit, BLP-1.9+) before demodulation by a lock-in amplifier (Stanford Research Systems, SR844) to create the ground-state depletion contrast.

The single gold nanoparticle samples are prepared by spin-coating a gold colloid (Sigma-Aldrich, G1652) onto cleaned No.1 microscope cover slips. A thin layer of polyvinyl alcohol (Aldrich, MW 31,000-50,000) is coated on top of the nanoparticles for blocking immersion oil and index-matching to maximize the collection efficiency of the probe beam into the detector. The sample is scanned across the fixed laser foci with a piezoelectric stage (Mad City Labs, Nano-H100) in x-y dimension. A modified Nanoscope IIIA controller (Digital Instruments) is used for controlling the scanning stage and generating images by acquiring signals from the in-

phase component output of the lock-in amplifier.

For detection of Atto647N molecules, a solid-state laser (CrystaLaser, DL640-050) at 642 nm is used as the pump beam and a HeNe laser (Coherent, 31-2082-000) at 633 nm is used as the probe beam. The polarizations of both lasers are parallel with each other. The intensity of the pump beam is modulated at 1.75 MHz by the same AOM as for the nanoparticle detection. The pump and probe beams are spatially combined with a dichroic mirror (Chroma, Q646LP-BS) and collinearly propagate into the same microscope as above. The scheme of generating ground-state depletion signal is the same with the nanoparticle detection, except that the pump beam is blocked by a narrow bandpass filter (Semrock, LL01-633-12.5) while the probe beam is detected by the photodiode. Epi-fluorescence emitted by the molecules is spectrally filtered and collected by an avalanche photodiode (APD) (Perkin Elmer, SPCM-CD2801) in a confocal mode. The APD counts is read and converted to an analog signal by a gated photon counter (Stanford Research Systems, SR400). The Nanoscope IIIA controller is used for both generating fluorescence images by acquiring signals from the photon counter and recording ground-state depletion signals.

The single-molecule samples are prepared by spin-coating a 50 picomolar solution of Atto647N (Sigma-Aldrich, 04507) molecules (diluted into a poly(methyl methacrylate) matrix, 3% by mass PMMA, Polysciences, MW 75,000) onto cleaned No.1 microscope cover slips. A thin layer of polyvinyl alcohol is coated on top of the PMMA layer.

3.4.2 Equations for modulation depth of the transmitted probe beam

Considering only the ground state and the first excited state of a chromophore, the power attenuation by the single molecule under a tightly focused laser beam is the product of the power

that hits the molecular absorption cross-section and the probability that the molecule stays in the ground state.

Assuming the excitation field in the beam waist is uniform, the power that hits the molecular absorption cross-section is $(\sigma/S)\cdot P$, where σ is the absorption cross-section for a single chromophore, S is the beam waist area, and P is the incident power. The probability that the molecule stays in the ground state is determined by the rate of excitation and relaxation. The rate of excitation,

$$k_{exc} = \frac{(\sigma/S)\cdot P}{h\nu}, \tag{3.4}$$

where $h\nu$ is the photon energy. And the rate of relaxation,

$$k_{relax} = \tau^{-1}, \tag{3.5}$$

where τ is the excited state lifetime of the molecule. Considering a time scale that is much longer than a photo cycle, the transition between ground state and the excited state reaches a steady state, and the probability for the molecule to be at ground state is

$$p_{ground} = \frac{k_{relax}}{k_{relax} + k_{exc}} = \frac{k_{relax}}{k_{relax} + (\sigma / h\nu S)\cdot P}, \tag{3.6}$$

Therefore the power attenuation is,

$$\Delta P = p_{ground}(\sigma / S)\cdot P = \frac{k_{relax}\cdot(\sigma / S)\cdot P}{k_{relax} + (\sigma / h\nu S)\cdot P}, \tag{3.7}$$

which is Eq. 3.1.

Assume that the incident power levels of pump beam and probe beam are P_{pump} and P_{probe}, respectively. In the ground-state depletion microscopy, while the intensity of pump beam ν_1 is modulated, the probe beam ν_2 is always present interacting with the molecule. When the pump beam ν_1 is blocked, the probe beam ν_2 is absorbed by certain amount,

$$\Delta P_{off} = \frac{k_{relax} \cdot (\sigma / S) \cdot P_{probe}}{k_{relax} + (\sigma / h\nu S) \cdot P_{probe}} \tag{3.8}$$

In contrast, when both ν_1 and ν_2 are exciting the molecule, the attenuation at the probe beam wavelength ν_2 will be

$$\Delta P_{on} = \frac{k_{relax} \cdot (\sigma / S) \cdot P_{probe}}{k_{relax} + (\sigma / h\nu S) \cdot (2P_{pump} + P_{probe})} \tag{3.9}$$

Note that here we assume the difference in σ and $h\nu$ is negligible for ν_1 and ν_2. There is a factor of 2 in front of P_{pump} because the incident power of the pump beam when it is modulated on- is twice that of the average, assuming 100% modulation depth for the pump beam.

It is evident that, because the ground state population is depleted more when both ν_1 and ν_2 are present, the corresponding attenuation of the probe beam will be less compared to the case where the pump beam is blocked

$$\Delta P_{off} > \Delta P_{on} \tag{3.10}$$

Therefore, the switching between pump beam on- and pump beam off- will create a modulation depth, $\delta\delta P_{probe}$,

$$\delta\delta P_{probe} \equiv \Delta P_{off} - \Delta P_{on} = \frac{2k_{relax} \cdot (\sigma^2 / S^2\, h\nu) \cdot P_{pump} P_{probe}}{\left(k_{relax} + (\sigma / h\nu S) \cdot P_{probe}\right) \cdot \left(k_{relax} + (\sigma / h\nu S) \cdot (2P_{pump} + P_{probe})\right)} \tag{3.11}$$

which is Eq. 3.2.

3.4.3 Estimate of the ground-state depletion signal from a single gold nanoparticle

The absorption cross section of a 20 nm gold nanoparticle at its plasmon resonance is ~4×10^{-12} cm^2 (Berciaud et al., 2006). It has been shown that after excitation by subpicosecond laser pulses, the kinetics of the recovering plasmon band is biexponential (Ahmadi et al., 1996). The bleached ground state A recovers through a fast electron-phonon relaxation mechanism (1~4 ps)

(Ahmadi et al., 1996; Hodak et al., 1998), and a slow phonon-phonon relaxation mechanism (~100ps) (Hodak et al., 1998).

$$B \xrightarrow{k_1} C \xrightarrow{k_2} A$$

The rate constants for the fast relaxation (B to C) and the slow relaxation (C to A) are k_1 and k_2 respectively. We first calculate the temporal behavior of the absorption at the plasmon band by the gold nanoparticle after excitation by an ultrafast laser pulse.

Let states A and C have absorption cross sections σ_A and σ_C respectively, and assume that the absorption of B is negligible. Let p_A, p_B and p_C represent the probabilities that the gold nanoparticle is in state A, B, and C, respectively. The absorbance of the nanoparticle,

$$\text{Abs} \propto p_A\sigma_A + p_C\sigma_C \qquad (3.12)$$

At time zero,

$$p_{B,t=0} = 1 \qquad (3.13)$$

In the infinite time limit,

$$p_{A,t=\infty} = 1 \qquad (3.14)$$

At arbitrary time t, we have

$$p_A + p_B + p_C = 1 \qquad (3.15)$$

$$\frac{dp_C}{dt} = k_1 p_B - k_2 p_C \qquad (3.16)$$

$$\frac{dp_A}{dt} = k_2 p_C \qquad (3.17)$$

The system of differential equations (Eq. 3.13 to 3.17) can be solved as

$$p_C = \frac{k_1}{k_2 - k_1}(e^{-k_1 t} - e^{-k_2 t}) \qquad (3.18)$$

$$p_A = 1 - \frac{k_2}{k_2 - k_1} e^{-k_1 t} - \frac{k_1}{k_1 - k_2} e^{-k_2 t} \qquad (3.19)$$

Substitute Eq. 3.18 and Eq. 3.19 into Eq. 3.12, the absorbance of the nanoparticle can be rearranged as

$$\text{Abs} \propto \sigma_A + \frac{k_2\sigma_A - k_1\sigma_C}{k_1 - k_2} e^{-k_1 t} + \frac{k_1(\sigma_C - \sigma_A)}{k_1 - k_2} e^{-k_2 t} \qquad (3.20)$$

Note that $k_1 \gg k_2$. When $\sigma_C < \sigma_A$ and $\frac{k_2}{k_1} < \frac{\sigma_C}{\sigma_A}$, the absorbance as a function of time is biexponential, consistent with the measured kinetics of plasmon band recovery (Ahmadi et al., 1996).

According to Eq. 3.20, the amplitudes of the fast and slow components in the biexponential kinetics of the plasmon band recovery are proportional to $\frac{k_2\sigma_A - k_1\sigma_C}{k_1 - k_2}$ and $\frac{k_1(\sigma_C - \sigma_A)}{k_1 - k_2}$, respectively.

The ratio of the amplitudes of the fast component and slow component was reported to be 1.5 using 380 nm excitation light, and 9 using 600 nm excitation light (Ahmadi et al., 1996). We assume the ratio as 9 for the excitation wavelength that we use (532 nm and 520 nm).

$$\frac{\frac{k_2\sigma_A - k_1\sigma_C}{k_1 - k_2}}{\frac{k_1(\sigma_C - \sigma_A)}{k_1 - k_2}} = \frac{k_2\sigma_A - k_1\sigma_C}{k_1(\sigma_C - \sigma_A)} = 9 \qquad (3.21)$$

According to (Hodak et al., 1998), $k_1 \approx \frac{1}{4\times10^{-12} s} = 2.5\times10^{11} s^{-1}$ and $k_2 \approx \frac{1}{100\times10^{-12} s} = 10^{10} s^{-1}$, therefore we have $\sigma_C = 0.9\sigma_A$.

We next calculate the power of the incident laser beam that is attenuated by a gold nanoparticle in a one beam CW experiment with the following kinetic scheme:

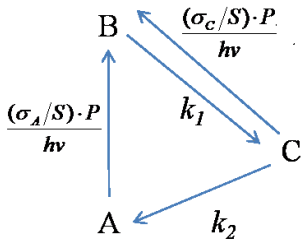

Figure 3.12 Kinetic scheme for contineous wave optical excitation and excited state relaxation of a gold nanoparticle.

Under continuous excitation, the probabilities of the three states of the gold nanoparticle reach a steady state. Therefore we have,

$$p_A + p_B + p_C = 1 \tag{3.22}$$

$$\frac{dp_A}{dt} = k_2 p_C - \frac{(\sigma_A / S)P}{h\nu} p_A = 0 \tag{3.23}$$

$$\frac{dp_B}{dt} = \frac{(\sigma_A / S)P}{h\nu} p_A - k_1 p_B + \frac{(\sigma_C / S)P}{h\nu} p_C = 0 \tag{3.24}$$

This system of the equations (Eq. 3.22 to Eq. 3.24) can be solved as

$$p_A = \frac{1}{1 + \frac{(\sigma_A / S)P}{k_1 h\nu} + \frac{(\sigma_A / S)P}{k_2 h\nu} + \frac{(\sigma_A / S)(\sigma_C / S)P^2}{k_1 k_2 (h\nu)^2}} \tag{3.25}$$

$$p_B = \frac{\frac{(\sigma_A / S)P}{k_1 h\nu} + \frac{(\sigma_A / S)(\sigma_C / S)P^2}{k_1 k_2 (h\nu)^2}}{1 + \frac{(\sigma_A / S)P}{k_1 h\nu} + \frac{(\sigma_A / S)P}{k_2 h\nu} + \frac{(\sigma_A / S)(\sigma_C / S)P^2}{k_1 k_2 (h\nu)^2}} \tag{3.26}$$

$$p_C = \frac{\frac{(\sigma_A / S)P}{k_2 h\nu}}{1 + \frac{(\sigma_A / S)P}{k_1 h\nu} + \frac{(\sigma_A / S)P}{k_2 h\nu} + \frac{(\sigma_A / S)(\sigma_C / S)P^2}{k_1 k_2 (h\nu)^2}} \tag{3.27}$$

The combined power attenuation from states A and C can be written as:

$$\Delta P = p_A(\sigma_A / S)\cdot P + p_C(\sigma_C / S)\cdot P = \frac{(\sigma_A + \frac{\sigma_C(\sigma_A / S)P}{k_2 h\nu})\cdot P / S}{1 + \frac{(\sigma_A / S)P}{k_1 h\nu} + \frac{(\sigma_A / S)P}{k_2 h\nu} + \frac{(\sigma_A / S)(\sigma_C / S)P^2}{k_1 k_2 (h\nu)^2}} \quad (3.28)$$

By substituting $\sigma_C = 0.9\sigma_A$ into Eq. 3.28, we get

$$\Delta P = \frac{(\sigma_A + \frac{0.9\sigma_A(\sigma_A / S)P}{k_2 h\nu})\cdot P / S}{1 + \frac{(\sigma_A / S)P}{k_1 h\nu} + \frac{(\sigma_A / S)P}{k_2 h\nu} + \frac{0.9(\sigma_A / S)^2 P^2}{k_1 k_2 (h\nu)^2}} \quad (3.29)$$

Because $\frac{(\sigma_A / S)P}{k_2 h\nu} \gg \frac{(\sigma_A / S)P}{k_1 h\nu} \gg 1$, Eq. 3.29 can be simplified as

$$\Delta P \approx \frac{\frac{0.9\sigma_A(\sigma_A / S)P}{k_2 h\nu}\cdot P / S}{\frac{(\sigma_A / S)P}{k_2 h\nu} + \frac{0.9(\sigma_A / S)^2 P^2}{k_1 k_2 (h\nu)^2}} = \frac{k_1 \cdot (0.9\sigma_A / S)\cdot P}{k_1 + (0.9\sigma_A / h\nu S)\cdot P} \quad (3.30)$$

We note that single gold nanoparticle result Eq. 3.30 is similar to the single molecule result Eq. 3.7.

In our CW pump-probe experiment, when the pump beam is on, the attenuation of the probe beam by the gold nanoparticle equals

$$\Delta P_{on} = \frac{k_1 \cdot (0.9\sigma_A / S)\cdot P_{probe}}{k_1 + (0.9\sigma_A / h\nu S)\cdot (2P_{pump} + P_{probe})} \quad (3.31)$$

When the pump beam is off, the attenuation of the probe beam equals

$$\Delta P_{off} = \frac{k_1 \cdot (0.9\sigma_A / S)\cdot P_{probe}}{k_1 + (0.9\sigma_A / h\nu S)\cdot P_{probe}} \quad (3.32)$$

The modulation depth of the transmitted probe beam is therefore

$$\frac{\delta\delta P}{P_{probe}} = \frac{\Delta P_{off} - \Delta P_{on}}{P_{probe}} = \frac{2k_1 \cdot (0.81{\sigma_A}^2 / S^2 h\nu)\cdot P_{pump}}{[k_1 + (0.9\sigma_A / h\nu S)\cdot P_{probe}][k_1 + (0.9\sigma_A / h\nu S)\cdot (2P_{pump} + P_{probe})]}$$

Given a beam waist area of:

$$S = \pi r^2 = \pi(\frac{0.61\times\lambda}{2\times N.A.})^2 = \pi(\frac{0.61}{2\times 1.4}\times\frac{(520+532)\times10^{-7}\text{cm}}{2})^2 = 4.12\times10^{-10}(\text{cm}^2)$$

an average photon energy of:

$$h\nu = h\frac{c}{\lambda} = 6.63\times10^{-34}\times\frac{3\times10^8}{(520+530)/2\times10^{-9}} = 3.78\times10^{-19}(J)$$

absorption cross section $\sigma_A = 4\times10^{-12}cm^2$, pump and probe power $P_{probe} = P_{pump} = 450\mu W$, and relaxation rate $k_1 = 2.5\times10^{11}s^{-1}$, the signal can be calculated as

$$\frac{\delta\delta P}{P_{probe}} = \frac{2\times2.5\times10^{11}\times\frac{0.81\times(4\times10^{-12})^2}{3.78\times10^{-19}\times(4.12\times10^{-10})^2}\times450\times10^{-6}}{[2.5\times10^{11}+\frac{0.9\times4\times10^{-12}\times450\times10^{-6}}{3.78\times10^{-19}\times4.12\times10^{-10}}][2.5\times10^{11}+\frac{0.9\times4\times10^{-12}\times1350\times10^{-6}}{3.78\times10^{-19}\times4.12\times10^{-10}}]} = 1\times10^{-4}$$

Figure 3.6 reveals the ground-state depletion signal for a single 20 nm gold nanoparticle is $\delta\delta P/P$ ~0.5×10^{-4}. The theoretical estimate and experimental results reach a reasonable agreement. The difference between them can be explained by the rough estimation of the fast/slow component ratio and relaxation rates that we get from time-resolved spectroscopy which was not conducted under exactly the same experimental conditions as ours (excitation wavelength, solvent for the nanoparticles, etc).

3.4.4 Calculation of the ground-state depletion signal from a single Atto647N molecule

Again, the difference in cross-section σ, *S* and *hν* for wavelengths 633 nm and 647 nm is neglected. The extinction coefficients ε of Atto647N at 633 nm and 642 nm in aqueous solution are,

$$\varepsilon\ (633\text{ nm}) = 116{,}000\ \text{M}^{-1}\cdot\text{cm}^{-1}$$

$$\varepsilon\ (642\text{ nm}) = 148{,}000\ \text{M}^{-1}\cdot\text{cm}^{-1}$$

According to the relation

$$\sigma = 3.82\times10^{-21}\varepsilon \qquad (3.33)$$

where σ is in the unit of cm^2 and ε is in the unit of $M^{-1}\cdot cm^{-1}$, the average absorption cross-section in the spectral region between 633 nm and 647 nm equals to

$$\sigma = 3.82\times10^{-21}\times\frac{(1.16+1.48)\times10^5}{2} = 5.04\times10^{-16}(\mathrm{cm}^2)$$

The beam waist area *S* for a 1.4 N.A. objective, 633 nm and 642 nm wavelengths,

$$S = \pi r^2 = \pi(\frac{0.61\times\lambda}{2\times N.A.})^2 = \pi(\frac{0.61}{2\times1.4}\times\frac{(633+642)\times10^{-7}\mathrm{cm}}{2})^2 = 6.06\times10^{-10}(\mathrm{cm}^2)$$

The average photon energy,

$$h\nu = h\frac{c}{\lambda} = 6.63\times10^{-34}\times\frac{3\times10^8}{(633+642)/2\times10^{-9}} = 3.12\times10^{-19}(J)$$

The relaxation rate of Atto647N,

$$k_{relax} = \tau^{-1} = \frac{1}{3.4\times10^{-9}} = 2.9\times10^8(s^{-1})$$

where τ is the excited state lifetime of Atto647N, which is 3.4 ns (Kolmakov et al., 2010).

The power levels of pump and probe beams,

$$P_{pump} = 350\ \mu\mathrm{W}$$

$$P_{probe} = 350\ \mu\mathrm{W}$$

Substituting σ, *S*, $h\nu$, k_{relax}, P_{pump}, and P_{probe} into Eq. 3.11, the modulation depth transferred by a single molecule,

$$\frac{\delta\delta P}{P} = \frac{2\times2.9\times10^8\times(\frac{5.04\times10^{-16}}{6.06\times10^{-10}})^2\times\frac{350\times10^{-6}}{3.12\times10^{-19}}}{\left(2.9\times10^8+\frac{5.04\times10^{-16}\times350\times10^{-6}}{6.06\times10^{-10}\times3.12\times10^{-19}}\right)\times\left(2.9\times10^8+\frac{5.04\times10^{-16}\times(2\times350+350)\times10^{-6}}{6.06\times10^{-10}\times3.12\times10^{-19}}\right)} = 1.2\times10^{-7}$$

3.4.5 Calculation of shot noise

Assuming 70% collection efficiency, the number of photons that arrive the photodiode during 30 ms integration time for 350 μW incident power at 633 nm,

$$\#\ \text{photon per 30 ms} = \frac{P \cdot t \cdot 0.7}{h\frac{c}{\lambda}} = \frac{350\times10^{-6}\times0.7\times30\times10^{-3}}{6.63\times10^{-34}\times\frac{3\times10^{8}}{633\times10^{-9}}} = 2.34\times10^{13}.$$

Therefore the instant shot noise,

$$\text{shot noise for 30 ms integration} = \frac{1}{\sqrt{2.34\times10^{13}}} = 2.1\times10^{-7}.$$

The instant shot noise can be reduced by averaging the lines that scanned across a molecule. Molecule A in Figure 3.10A survives 45 line scans, the shot noise is reduced to

$$\frac{2.1\times10^{-7}}{\sqrt{45}} = 3.1\times10^{-8}.$$

Molecule B in Figure 3.10C survives 44 line scans, the shot noise is reduced to

$$\frac{2.1\times10^{-7}}{\sqrt{44}} = 3.2\times10^{-8}.$$

3.4.6 Modulation frequency dependence of ground-state depletion signals

Using the ground-state depletion microscope, we imaged single 20 nm gold nanoparticles in a same field of view with modulation frequencies in the range from 750 kHz to 7 MHz. The power level at laser foci for each beam is 450 μW. Figure 3.13 shows that the signal of gold nanoparticles is independent of modulation frequencies.

Using the ground-state depletion microscope, we imaged aggregates of Atto647N in the PMMA matrix with modulation frequencies in the range from 60 kHz to 8 MHz. The power level at laser foci for each beam is 350 μW. We prepared a homogeneous layer of Atto647N molecules by spin-coating a 200 nanomolar solution of Atto647N (diluted into a poly(methyl

methacrylate) matrix, 3% mass PMMA, Polysciences, MW 75,000) onto cleaned No.1 microscope cover slips. A thin layer of polyvinyl alcohol is coated on top of the PMMA layer. To avoid the complication of Atto647N photobleaching, we changed the field of view before imaging at a new modulation frequency. Figure 3.14 shows that the signal of Atto647N aggregates is independent of modulation frequencies.

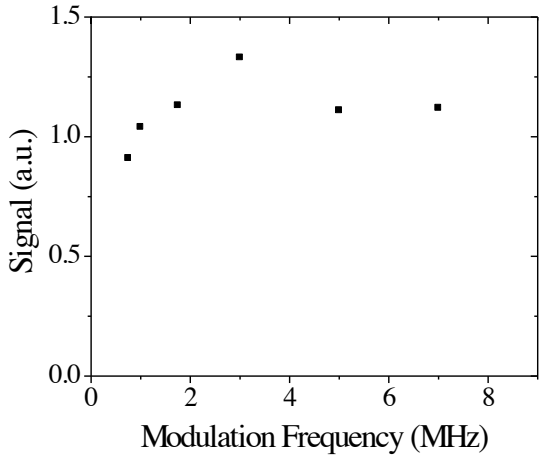

Figure 3.13 Ground-state depletion signal of 20 nm gold nanoparticles measured with different modulation frequencies.

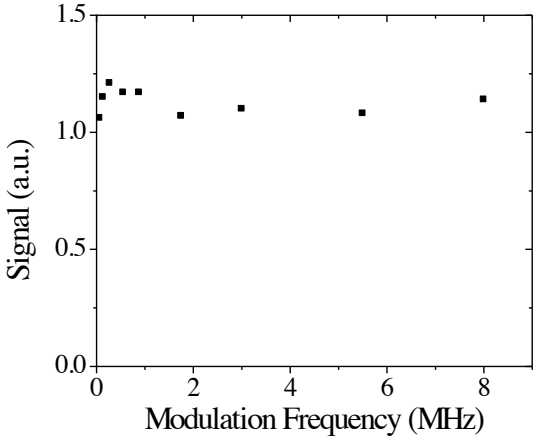

Figure 3.14 Ground-state depletion signal of Atto647N aggregates in PMMA matrix measured with different modulation frequencies.

3.4.7 Detectability of single-molecule ground-state depletion signals

Figure 3.15 shows the number of line scans before single Atto647N molecules photobleach during simultaneous acquisition of fluorescence and ground-state depletion signals. The histogram can be fitted with an exponential decay (black curve). A single Atto647N molecule survives 13 lines on average under our experimental condition. In principle, averaging about 20 line scans are required to reduce noise to allow ground-state depletion signal from a single molecule to be detected. For the 690 molecules as shown in Figure 3.15, 19% of them survive longer than 20 lines. We successfully detected ground-state depletion signal from 54% of these long-lived molecules. The fact that we didn't detect all of the long-lived molecules can be explained by the random orientation of absorption dipole moments and the inhomogeneity of the single-molecule absorption spectrum.

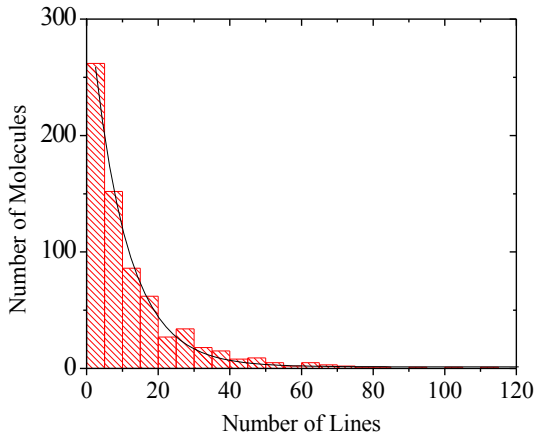

Figure 3.15 Occurrence of number of line scans before photobleaching for 690 single Atto647N molecules.

References

Ahmadi, T.S., Logunov, S.L., and ElSayed, M.A. (1996). Picosecond dynamics of colloidal gold nanoparticles. J Phys Chem-Us *100*, 8053-8056.

Berciaud, S., Lasne, D., Blab, G.A., Cognet, L., and Lounis, B. (2006). Photothermal heterodyne imaging of individual metallic nanoparticles: Theory versus experiment. Phys Rev B *73*, 045424.

Betzig, E., and Chichester, R.J. (1993). Single Molecules Observed by near-Field Scanning Optical Microscopy. Science *262*, 1422-1425.

Boyer, D., Tamarat, P., Maali, A., Lounis, B., and Orrit, M. (2002). Photothermal imaging of nanometer-sized metal particles among scatterers. Science *297*, 1160-1163.

Denk, W., Strickler, J.H., and Webb, W.W. (1990). Two-photon laser scanning fluorescence microscopy. Science *248*, 73-76.

Diaspro, A., Chirico, G., and Collini, M. (2005). Two-photon fluorescence excitation and related techniques in biological microscopy. Q Rev Biophys *38*, 97-166.

Freudiger, C.W., Min, W., Saar, B.G., Lu, S., Holtom, G.R., He, C.W., Tsai, J.C., Kang, J.X., and Xie, X.S. (2008). Label-Free Biomedical Imaging with High Sensitivity by Stimulated Raman Scattering Microscopy. Science *322*, 1857-1861.

Fu, D., Ye, T., Matthews, T.E., Chen, B.J., Yurtserver, G., and Warren, W.S. (2007a). High-resolution in vivo imaging of blood vessels without labeling. Opt Lett *32*, 2641-2643.

Fu, D., Ye, T., Matthews, T.E., Grichnik, J., Hong, L., Simon, J.D., and Warren, W.S. (2008). Probing skin pigmentation changes with transient absorption imaging of eumelanin and pheomelanin. J Biomed Opt *13*, 054036.

Fu, D., Ye, T., Matthews, T.E., Yurtsever, G., and Warren, W.S. (2007b). Two-color, two-photon, and excited-state absorption microscopy. J Biomed Opt *12*, 054004.

Funatsu, T., Harada, Y., Tokunaga, M., Saito, K., and Yanagida, T. (1995). Imaging of Single Fluorescent Molecules and Individual Atp Turnovers by Single Myosin Molecules in Aqueous-Solution. Nature *374*, 555-559.

Gaiduk, A., Yorulmaz, M., Ruijgrok, P.V., and Orrit, M. (2010a). Room-Temperature Detection of a Single Molecule's Absorption by Photothermal Contrast. Science *330*, 353-356.

Gaiduk, A., Ruijgrok, P.V., Yorulmaz, M., and Orrit, M. (2010b). Detection Limits in Photothermal Microscopy. Chem Sci *1*, 343-350.

Gustafsson, M.G.L. (2005). Nonlinear structured-illumination microscopy: Wide-field fluorescence imaging with theoretically unlimited resolution. Proc Natl Acad Sci USA *102*, 13081-13086.

Hell, S.W., and Kroug, M. (1995). Ground-state-depletion fluorscence microscopy: A concept for breaking the diffraction resolution limit. Appl Phys B *60*, 495-497.

Hirschfeld, T. (1976). Optical Microscopic Observation of Single Small Molecules. Appl Optics *15*, 2965-2966.

Hodak, J.H., Martini, I., and Hartland, G.V. (1998). Spectroscopy and dynamics of nanometer-sized noble metal particles. J Phys Chem B *102*, 6958-6967.

Hwang, J., Fejer, M.M., and Moerner, W.E. (2006). Scanning interferometric microscopy for the detection of ultrasmall phase shifts in condensed matter. Phys Rev A *73*, 021802.

Kneipp, K., Wang, Y., Kneipp, H., Perelman, L.T., Itzkan, I., Dasari, R., and Feld, M.S. (1997). Single molecule detection using surface-enhanced Raman scattering (SERS). Phys Rev Lett *78*, 1667-1670.

Kolmakov, K., Belov, V.N., Bierwagen, J., Ringemann, C., Muller, V., Eggeling, C., and Hell, S.W. (2010). Red-Emitting Rhodamine Dyes for Fluorescence Microscopy and Nanoscopy. Chem-Eur J *16*, 158-166.

Kukura, P., Celebrano, M., Renn, A., and Sandoghdar, V. (2009). Imaging a Single Quantum Dot When It Is Dark. Nano Lett *9*, 926-929.

Kukura, P., Celebrano, M., Renn, A., and Sandoghdar, V. (2010). Single-Molecule Sensitivity in Optical Absorption at Room Temperature. J Phys Chem Lett *1*, 3323-3327.

Macklin, J.J., Trautman, J.K., Harris, T.D., and Brus, L.E. (1996). Imaging and time-resolved spectroscopy of single molecules at an interface. Science *272*, 255-258.

Mian, S.M., McGee, S.B., and Melikechi, N. (2002). Experimental and theoretical investigation of thermal lensing effects in mode-locked femtosecond Z-scan experiments. Opt Commun *207*, 339-345.

Min, W., Lu, S.J., Chong, S.S., Roy, R., Holtom, G.R., and Xie, X.S. (2009). Imaging chromophores with undetectable fluorescence by stimulated emission microscopy. Nature *461*, 1105-1109.

Moerner, W.E., and Kador, L. (1989). Optical detection and spectroscopy of single molecules in a solid. Phys Rev Lett *62*, 2535-2538.

Moerner, W.E., and Orrit, M. (1999). Illuminating single molecules in condensed matter. Science *283*, 1670-1676.

Nie, S.M., and Emery, S.R. (1997). Probing single molecules and single nanoparticles by surface-enhanced Raman scattering. Science *275*, 1102-1106.

Orrit, M., and Bernard, J. (1990). Single Pentacene Molecules Detected by Fluorescence Excitation in a Para-Terphenyl Crystal. Phys Rev Lett *65*, 2716-2719.

Rigler, R., and Widengren, J. (1990). Ultrasensitive Detection of Single Molecules by Fluorescence Correlation Spectroscopy. BioScience *3*, 180-183.

Selvin, P.R., and Ha, T. (2008). Single-Molecule Techniques: A Laboratory Manual (Cold Spring Harbor, New York: Cold Spring Harbor Laboratory Press).

Shera, E.B., Seitzinger, N.K., Davis, L.M., Keller, R.A., and Soper, S.A. (1990). Detection of Single Fluorescent Molecules. Chem Phys Lett *174*, 553-557.

Uchiyama, K., Hibara, A., Kimura, H., Sawada, T., and Kitamori, T. (2000). Thermal lens microscope. Jpn J Appl Phys 1 *39*, 5316-5322.

Weiss, S. (1999). Fluorescence spectroscopy of single biomolecules. Science *283*, 1676-1683.
Xie, X.S., Choi, P.J., Li, G.W., Lee, N.K., and Lia, G. (2008). Single-molecule approach to molecular biology in living bacterial cells. Annu Rev Biophys *37*, 417-444.

Xie, X.S., and Trautman, J.K. (1998). Optical studies of single molecules at room temperature. Annu Rev Phys Chem *49*, 441-480.

Chapter 4

A novel single-molecule assay to monitor real-time transcription on individual DNA templates *in vitro*

Transcription, the first step in gene expression, is essential in cell metabolism. The kinetics and mechanisms of transcription have been investigated by a repertoire of single-molecule techniques, including optical and magnetic tweezers, atomic force microscopy, and high-sensitivity fluorescence techniques. However, none of the existing assays allow simultaneous measurements of transcription initiation and elongation rates *in vitro*. To this end, here we describe a novel *in vitro* single-molecule assay that follows real-time transcription on individual DNA templates. The elongation process on templates with any sequence can be monitored for multiple rounds of transcription on each template. This is a high-throughput measurement because hundreds of templates can be monitored simultaneously in one field of view. This assay is capable of measuring transcription initiation, elongation and termination kinetics.

4.1 Background

Essential for all cell functions, transcription, the synthesis of mRNAs from DNA carried out by RNA polymerase (RNApol), is the first step in gene expression. Transcription has been studied *in vitro* at the single-molecule level using a number of techniques based on either mechanical manipulation (Abbondanzieri et al., 2005; Bai et al., 2006; Billingsley et al., 2012; Bustamante et al., 2011; Herbert et al., 2008) or fluorescence imaging (Chakraborty et al., 2012; Friedman and Gelles, 2012; Kapanidis et al., 2006; Revyakin et al., 2012; Tang et al., 2009; Zhang et al., 2014). On one hand, single-molecule manipulation techniques like optical trap and magnetic trap usually have a low throughput, i.e., they observe transcription on one DNA template at a time. On the other hand, existing techniques based on fluorescence imaging require either complex procedures of labeling biomolecules at specific residues (for smFRET), or careful designs of cDNA that probes RNA with a specific sequence. Moreover, these existing *in vitro* single-molecule assays only observe initiation or elongation processes of one round of transcription, making them incapable of measuring transcription initiation rates.

We aim to develop a high-throughput *in vitro* single-molecule assay that monitors multiple rounds of transcription on many individual templates with any sequence in real time. The new assay should be capable of measuring the kinetics of transcription initiation, elongation and termination, and be generally useful for studying many questions in transcription, such as bursting and pausing. As will be shown in Chapter 5, we use this assay to investigate the effects of DNA supercoiling on transcription initiation and elongation, which reveal the mechanism of transcriptional bursting in bacteria.

4.2 Results

4.2.1 A nucleic acid stain that selectively stains RNA

SYTO RNASelect (Life Technologies) is a nucleic acid stain that is non-fluorescent at 530 nm and weakly fluorescent upon binding to DNA, but becomes much brighter upon binding to RNA (Figure 4.1). It has been used to qualitatively measure the distribution of RNA in the presence of DNA in mouse tissues (Kannemeier et al., 2007).

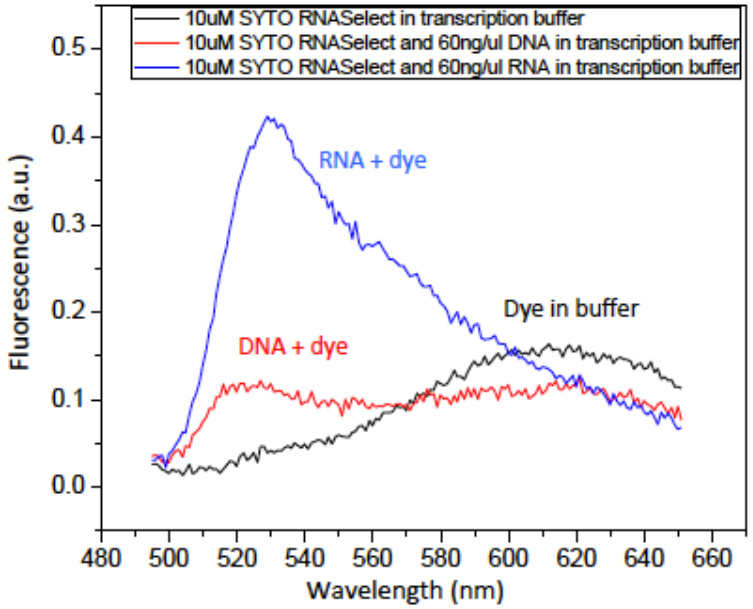

Figure 4.1 Fluorescence emission spectra of SYTO RNASelect solution under 488 nm excitation.

The dye selectively stains RNA and emits fluorescence with a peak at 530 nm. In the absence of nucleic acids, the dye is not fluorescent at 530 nm.

4.2.2 An *in vitro* single-molecule transcription assay based on SYTO RNASelect stain

An Argon laser line at 488 nm was used to excite SYTO RNASelect in a total internal reflection fluorescence (TIRF) microscope. We collected fluorescence at 530 nm and recorded time-lapse movies with a CCD camera. In order to make sure that SYTO RNASelect labels RNA fast enough to allow us to follow transcription elongation in real time, we immobilized 4 kb-long RNA on the flow cell surface, injected 250 nM SYTO RNASelect into the flow cell while monitoring the sample fluorescence with the TIRF microscope. All the fluorescent spots, which

corresponded to the stained RNA molecules, appeared on the surface within a second after the injection (data not shown).

We performed *in vitro* transcription in the presence of 250 nM SYTO RNASelect. On the TIRF microscope, a single nascent mRNA is visible, and its fluorescence intensity increases with the mRNA length. Therefore we were able to track transcription elongation in real time as the nascent mRNA being produced on a surface-tethered DNA template. Transcription activities on up to hundreds of templates in one field of view can be monitored simultaneously (Figure 4.2). We also optimized the transcription buffer to enable T7 and *E. coli* RNApol to work in conjunction with *E. coli* gyrase and Topo I, the latter two enzymes were used in our study of supercoiling effects on transcription initiation and elongation, presented in Chapter 5.

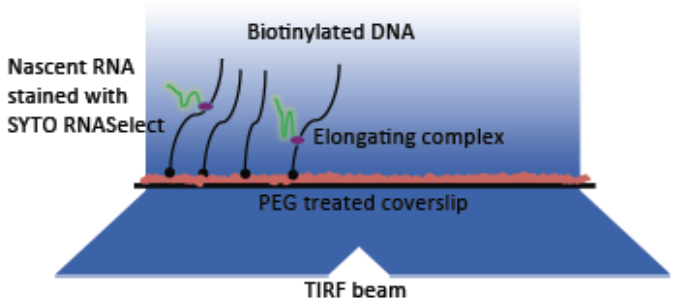

Figure 4.2 Schematic representation of the experimental arrangement (not drawn to scale). In the presence of 250 nM SYTO RNASelect, nascent RNAs are fluorescent under TIRF excitation at 488 nm. With an excitation power density of 0.22 W/cm^2 and an image acquisition time of 5 s, a transcript of 2.3k nucleotides yields a SNR of 1.

As a control, we examined the effect of SYTO RNASelect on the activities of enzymes involved in our system, including T7 RNApol, *E. coli* RNApol, *E. coli* gyrase, and *E. coli* Topo I. None of them were found to be affected by the stain (Figure 4.3-4.5). With sufficiently low laser power and the presence of a fresh oxygen scavenger system, photobleaching of the dye and photocleavage of nucleic acids were negligible (Figure 4.6).

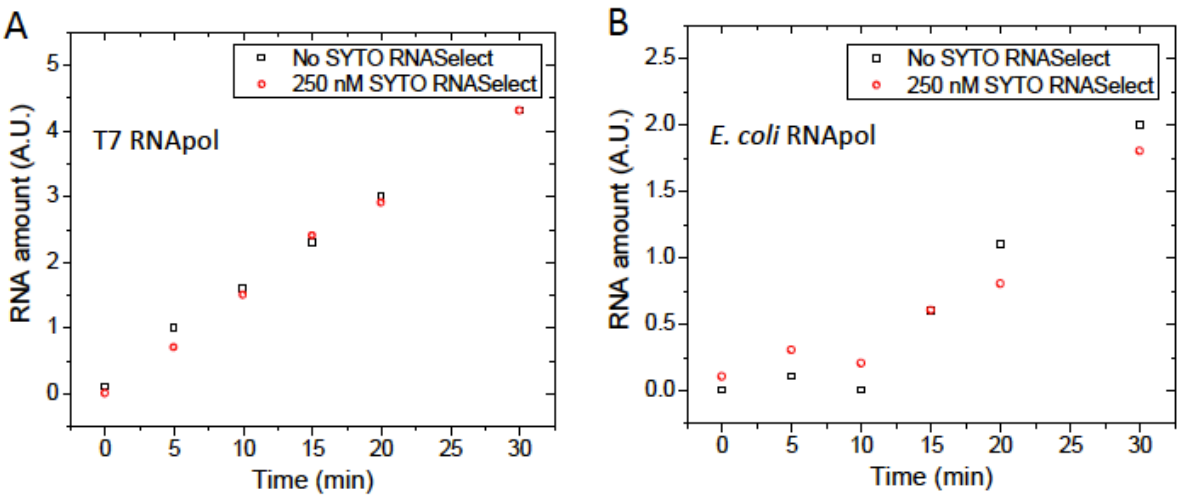

Figure 4.3 SYTO RNASelect does not affect transcription rates of T7 and *E. coli* RNApol.

(A) The amount of mRNA generated by *in vitro* T7 transcription for different time in the absence or presence of 250 nM SYTO RNASelect. The amounts of mRNA were measured by Qubit RNA assay. (B) The amount of mRNA generated by *in vitro E. coli* transcription for different time in the absence or presence of SR.

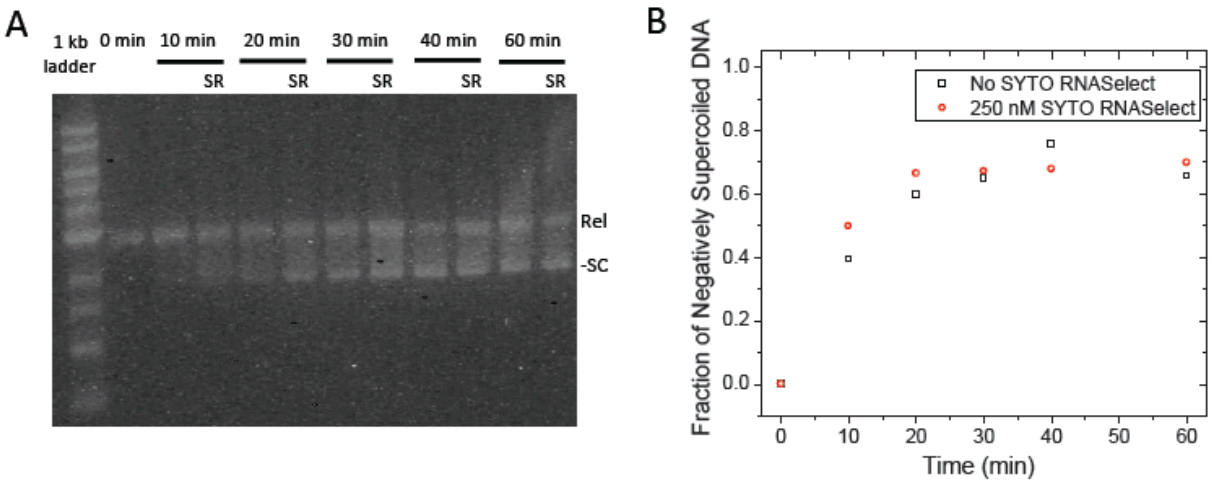

Figure 4.4 SYTO RNASelect does not affect the activity of *E. coli* gyrase.

(A) Time dependence of negative supercoiling of relaxed pUC19 plasmid by *E. coli* gyrase in the absence or presence of 250 nM SYTO RNASelect (SR). The position of relaxed pUC19 (Rel) and its most supercoiled topoisomer (-SC) are marked. (B) The fraction of negatively supercoiled pUC19 in the total amount of pUC19 after gyrase treatment for different time. The amounts of pUC19 were measured from the intensity of bands in (A).

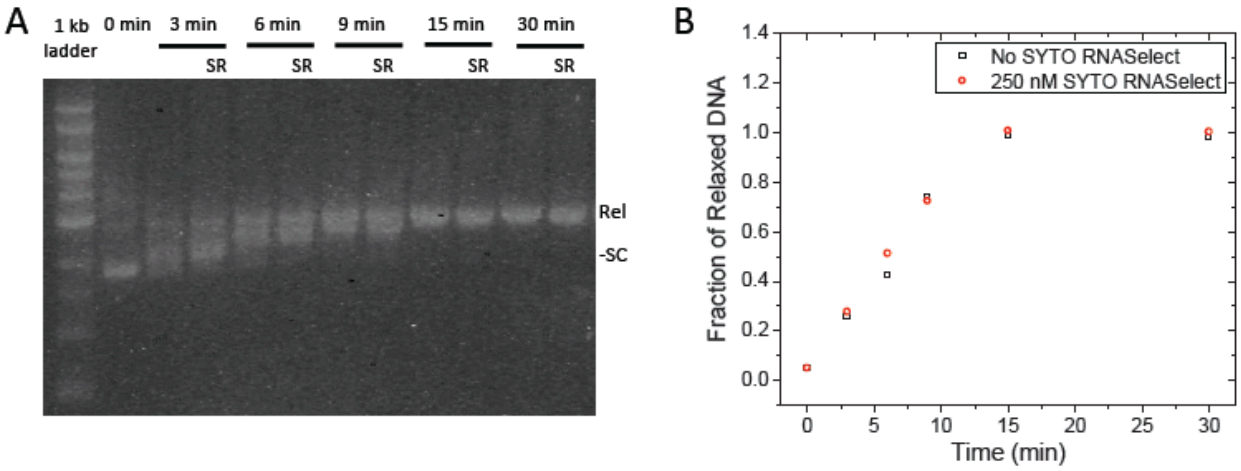

Figure 4.5 SYTO RNASelect does not affect the activity of *E. coli* Topo I.

(A) Time dependence of relaxation of negatively supercoiled pUC19 plasmid by *E. coli* Topo I in the absence or presence of 250 nM SYTO RNASelect (SR). (B) The fraction of relaxed pUC19 in the total amount of pUC19 after Topo I treatment for different time. The amounts of pUC19 were measured from the intensity of bands in (A).

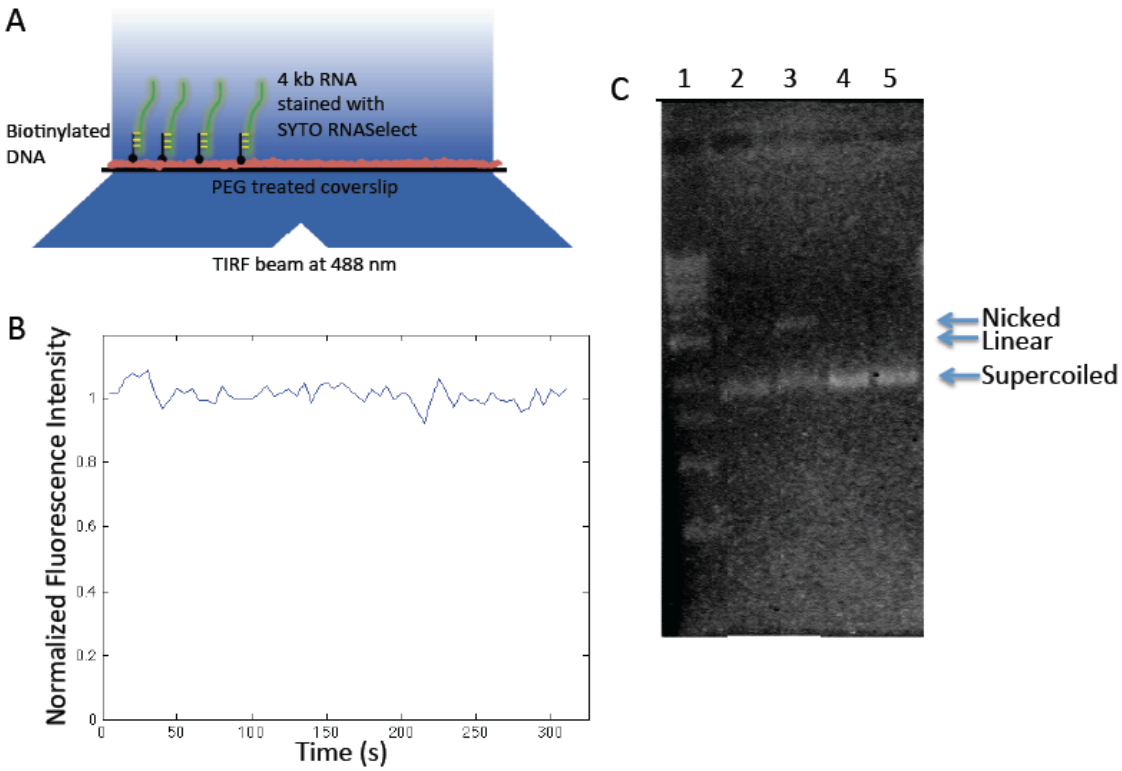

Figure 4.6 Control of dye photobleaching and nucleic acids photocleavage in the *in vitro* single-molecule assay.

(A) Schematic representation of the experimental arrangement for the RNA photobleaching assay (not drawn to scale). (B) Total fluorescence intensity versus time from 67 individual RNA molecules immobilized on the surface. The intensity barely changed over time, indicating negligible photobleaching. (C) Minimal DNA photocleavage occurred in the presence of 250 nM SYTO RNASelect during the time for transcription initiation rate measurement From left to right: 1 kb DNA ladder (lane 1), supercoiled pUC19 DNA after 30 minutes of 488 nm laser illumination at 0.22 W/cm^2 (lane 2) or 7.3 W/cm^2 (lane 3) in the presence of 250 nM SYTO RNASelect, supercoiled pUC19 DNA without any treatment (lane 4), or after 30 minutes of incubation with 250 nM SYTO RNASelect in dark (lane 5). While some pUC19 DNA became nicked after high-power illumination, barely any nick or double-stranded breaks were generated on the DNA after laser illumination at the same power level in the *in vitro* single-molecule assay.

In our single-molecule assay, DNA templates containing a promoter were tethered on the passivated surface of the flow cell through biotin-streptavidin linkage. After we flowed RNApol and NTPs into the flow cell, the fluorescence intensity of some spots in the field of view linearly ramped up due to transcription elongation, followed by abrupt disappearance upon transcription termination (Figure 4.7). "Blinking" of fluorescence occurred when multiple transcripts were produced. As a control, no fluorescence intensity increase was observed under

any of the following conditions: 1) no RNApol in the solution, 2) no NTPs in the solution, 3) no promoter in the DNA template. Full-length transcripts (>12 kb) were generated as confirmed by RNA gel electrophoresis (Figure 4.8).

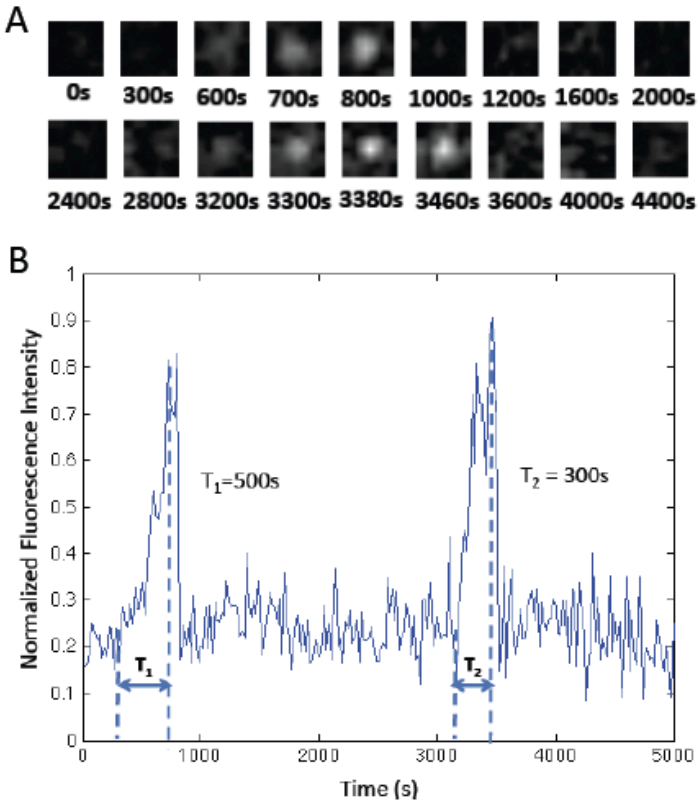

Figure 4.7 Imaging repetitive transcription events on one DNA template.

(A) Time-lapse images of 1.1 μm×1.1 μm sub-field-of-view to monitor T7 transcription on one 12 kb-long template. (B) Intensity versus time trajectory of the DNA template shown in (A). Full transcripts are produced repetitively on the template, with transcription elongation time T_1 = 500 s and T_2 = 300 s, respectively.

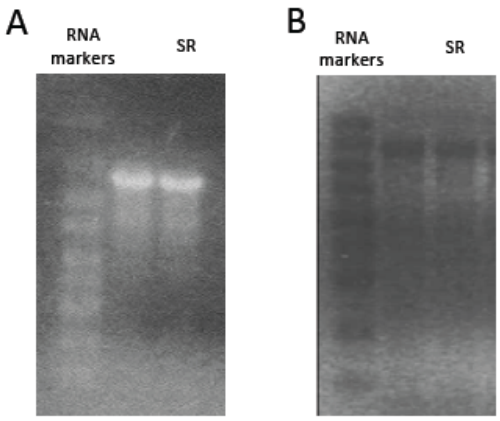

Figure 4.8 SYTO RNASelect does not affect processivity of T7 and *E. coli* RNApol.

(A) T7 transcription in the presence of 250 nM SYTO RNASelect (SR) produced full-length transcripts. From left to right: 0.2-10 kb RNA markers (lane 1), 5.3 kb *lac* operon mRNA produced by T7 transcription in the absence (lane 2), or presence of SR (lane 3). (B) *E. coli* transcription in the presence of 250 nM SYTO RNASelect (SR) produced full-length transcripts. From left to right: 0.2-10 kb RNA markers (lane 1, from Sigma-Aldrich), 5.3 kb *lac* operon mRNA produced by *E. coli* transcription in the absence (lane 2), or presence of SR (lane 3).

4.3 Materials and Methods

4.3.1 SYTO RNASelect fluorescence spectra

The fluorescence emission spectra of SYTO RNASelect were measured under 488 nm excitation (Varian Cary Eclipse Fluorimeter, Agilent Technologies, Santa Clara, CA) in the transcription buffer (40 mM Tris-HCl, pH 8.0, 10 mM $MgCl_2$, 5 mM DTT, 50 mM KCl, 6.5% glycerol and 100 μg/mL BSA) at a dye concentration of 10 μM under three conditions (Figure 4.1): in the absence of nucleic acids, in the presence of 60 ng/μL lambda DNA, or in the presence of 60 ng/μL 4 kb-long RNA prepared from T7 transcription from lambda DNA template.

4.3.2 DNA supercoiling and relaxation assays

The DNA supercoiling reaction mixture (21 μL) contained the following components: 1 unit of *E. coli* gyrase (New England Biolabs), 0.7 μg relaxed pUC19 (New England Biolabs), 1.75 mM

ATP, 0.3 mM C/G/UTP and transcription buffer with or without 250 nM SYTO RNASelect (Life Technologies). The mixture was incubated at 37°C for 10, 20, 30, 40 or 60 min. The reaction was stopped with 4.2 μL of quench buffer (500 mM EDTA). After the reaction, pUC19 was purified (D4004, Zymo Research, Irvine, CA), and its supercoiling level was probed by DNA agarose gel electrophoresis and SYBR Safe (Life Technologies) staining (Figure 4.4A). The fraction of negatively supercoiled pUC19 after each gyrase reaction was measured from the intensity ratio of corresponding bands in the DNA gel image. Figure 4.4B shows the fraction as a function of gyrase reaction time, indicating that 250 nM SYTO RNASelect does not affect the activity of gyrase.

The DNA relaxation assay mixture (12.5 μL) contained the following components: 0.25 unit of *E. coli* Topo I (New England Biolabs, Ipswich, MA), 0.5 μg negatively supercoiled pUC19, 1.75 mM ATP, 0.3 mM C/G/UTP and transcription buffer with or without 250 nM SYTO RNASelect. We note NTPs were not necessary for the Topo I activity. They were present to mimic the condition of the single-molecule transcription assay. The mixture was incubated at 37°C for 3, 6, 9, 15 or 30 min. The reaction was stopped with 1.5 μL of quench buffer (500 mM EDTA). The supercoiling level of the purified pUC19 was examined by DNA agarose gel as in the DNA supercoiling assay (Figure 4.5A). The fraction of relaxed pUC19 after each Topo I reaction was measured from the intensity ratio of corresponding bands in the DNA gel image. Figure 4.5B shows the fraction as a function of Topo I reaction time, indicating that 250 nM SYTO RNASelect does not affect the activity of Topo I.

4.3.3 Ensemble *in vitro* transcription assay

To probe potential SYTO RNASelect dye effect on *in vitro* transcription, an ensemble transcription assay was assembled by mixing T7 RNA polymerase (New England Biolabs) or *E.*

coli RNA polymerase (Epicentre), NTPs, and DNA templates containing corresponding promoter and a 5.3 kb transcribing sequence (*E. coli lac* operon), with or without 250 nM dye addition. RNase Inhibitor, Murine (New England Biolabs) was added to prevent RNA degradation during reaction. The reaction mixture was incubated at 37°C for 2 hrs. Afterwards, the template DNA was removed by TURBO DNase treatment (Life Technologies). The length and amount of the RNA product were probed by formaldehyde-based RNA agarose gel electrophoresis and EtBr straining. Figure 4.8 shows that neither T7 transcription nor *E. coli* transcription was affected by the presence of 250 nM SYTO RNASelect.

To further test potential SYTO RNASelect dye effect on the *in vitro* transcription rate, a real-time transcription assay was carried out with RNA yield measured at 6 time points within the first 30 min of transcription reaction. The ensemble transcription assay recipe was the same as described above, except the final RNA product was purified by RNA purification column (Zymo Research) and quantified by Qubit RNA HS assay (Life Technologies). As shown in Figure 4.3, 250 nM SYTO RNASelect does not affect transcription rates of T7 or *E. coli* RNApol.

4.3.4 Flowcell construction

The *in vitro* single-molecule transcription assay was performed inside a flow cell. For room-temperature experiments, coverslip surface treatment and flow cell construction were performed as previously described (Kim et al., 2007; Kim et al., 2013; Schroeder et al., 2008). The difference in coverslip surface treatment from the pervious procedure is that the PEG polymer solution used for surface functionalization was composed of 100 mg/mL mPEG-Succinimidyl Valerate (MW 5000, Laysan Bio, Inc., Arab, AL), 10 mg/mL SVA-mPEG-SVA (MW 3400, Laysan Bio) and 4 mg/mL biotin-mPEG-SVA (MW 5000, Laysan Bio). Compared with T7

RNApol, the activity of *E. coli* RNApol was found to be more sensitive to the storage condition of functionalized coverslips. Successful performance of *in vitro* single-molecule transcription assay with *E. coli* RNApol required the use of functionalized coverslips that were either freshly prepared or preserved at -80°C in vacuum that was generated by a foodsaver vacuum sealer.

For measurements at 37°C, a flow cell was constructed using a round coverslip (40 mm diameter) with the same surface treatment and a microaqueduct slide originally used in a live-cell micro-observation chamber system (FCS2, Bioptechs, Butler, PA). The flow cell temperature was controlled with the electronic controller in the FCS2 system.

4.3.5 TIRF microscope

An inverted microscope (Olympus IX70, Olympus America Inc., Melville, NY) was used for objective-type total internal reflection (TIR) illumination. A focused beam of 488 nm Argon laser (Innova300C MotoFreD, Coherent, Inc.) was directed at the edge of the back focal plane of a 60x objective lens (numerical aperture 1.45; PlanApo, Olympus) after passing through an excitation filter (L-488-10, Thin Film Imaging Technologies, Inc., Greenfield, MA). Excitation was controlled by a shutter (VS25S2ZM1R1-24, Vincent Associates, Rochester, NY). Fluorescence was collected through the same objective lens. After passing through an emission filter (HQ535/30M, Chroma, Bellows Falls, VT), the fluorescence was imaged on a back-illuminated electron multiplying charge coupled device camera (iXonEM+897, Andor Technology, South Windsor, CT). Typically, a field of view contained 300-600 immobilized DNA templates in ~110×110 μm^2.

4.3.6 Imaging buffer and image acquisition parameters

In order to measure T7 transcription elongation rates at room temperature, 5.3 nM T7 RNApol (New England Biolabs), 1.75 mM ATP, 0.3 mM C/G/UTP, 250 nM SYTO RNASelect and an

O_2-scavenging system (0.1 mg/mL glucose oxidase, 0.023 mg/mL catalase and 8 mg/mL dextrose) were added to 200 μL transcription buffer. To measure *E. coli* transcription elongation rates at 37°C, the reaction mixture was the same as T7 transcription except that it contained 220 nM *E. coli* RNApol (Epicentre Technologies Corp, Chicago, IL) instead of T7 RNApol. Immediately after the mixture was infused into the flow cell containing immobilized DNA templates, a fluorescent movie was recorded under 488 nm laser excitation at 0.22 W/cm^2. Images were taken every 20 seconds for 60-80 minutes with an image acquisition time of 5 seconds.

In order to measure T7 transcription initiation rates at 37°C, the reaction mixture was the same as that for T7 transcription elongation rate measurements except that concentrations of T7 RNApol and C/G/UTP were increased to 36.1 nM and 0.8 mM, respectively. To measure *E. coli* transcription initiation rates at 37°C, 176 nM *E. coli* RNApol, 3 mM A/C/G/UTP, 250 nM SYTO RNASelect and O_2-scavenging system composed of 2.5 mM protocatechuic acid (PCA, from Sigma-Aldrich, St. Louis, MO) and 50 nM protocatechuate-3,4-dioxygenase (PCD, from Sigma-Aldrich) were added to 40 μL transcription buffer. *E. coli* transcription initiation was found to be faster in the presence of the PCA/PCD O_2-scavenging system than in the presence of the glucose oxidase/catalase system. Fluorescent movies were recorded under 488 nm laser excitation at 0.15 W/cm^2. Images were taken every 75 seconds with an image acquisition time of 5 seconds.

4.3.7 Control for photobleaching of SYTO RNASelect stained RNA

Coverslip surface treatment and flow cell construction were performed as previously described (Kim et al., 2013). 4 kb-long RNA was prepared by ensemble *in vitro* T7 transcription. The 3' end of the RNA was hybridized to a 40-mer complementary DNA that contained a single

biotinylated nucleotide. The biotinylated RNA molecules were immobilized on the flowcell surface and stained with 250 nM SYTO RNASelect in the transcription buffer mixed with a fresh glucose oxidase/catalase O_2-scavengingsystem (Figure 4.6A). The fluorescent movie was recorded for 300 seconds under continuous 488nm laser excitation at 0.22 W/cm^2. The acquisition time of each image was 5 seconds. The total illumination time was the same as that of a 1200-second movie for transcription elongation rate measurement, where images were taken every 20 seconds. We note that 1200 seconds is significantly longer than the average time for generating a full transcript of 12 kb. Single RNA molecules appear as individual fluorescent spots in the field of view. The total fluorescence intensity versus time trajectory of 67 individual RNA molecules was extracted from the 300 sec movie (Figure 4.6B), which directly measures photobleaching of stained RNA, if any, during the time of transcription elongation. The O_2-scavenging effect of the PCA/PCD system used in the measurement of *E. coli* transcription initiation rates is comparable to that of the glucose oxidase/catalase system (Aitken et al., 2008).

4.3.8 Control for DNA photocleavage in the presence of SYTO RNASelect

Negatively supercoiled pUC19 DNA was prepared by incubating relaxed pUC19 (New England Biolabs) with *E. coli* gyrase. The sample for the photocleavage assay was a mixture of 5 μg/ml negatively supercoiled pUC19, 250 nM SYTO RNASelect and a fresh glucose oxidase/catalase O_2-scavengingsystem in the transcription buffer, mimicking the condition for the *in vitro* single-molecule transcription assay. The solution was filled in a quartz spectrophotometer cuvette (16.40F-Q-10, Starna Cells, Inc., Atascadero, CA) with three clear windows, two of which are square ones on the opposite sides of the cuvette. A collimated laser beam at 488 nm was aligned with the square windows, which continuously excited the solution at 0.22 W/cm^2 or 7.3 W/cm^2 for 30 minutes. The power density of 0.22 W/cm^2 was used for in the *in vitro* single-molecule

assay. The total illumination time was longer than that for *in vitro* transcription elongation and initiation rate measurements.

After illumination, pUC19 was purified with a DNA purification column (Qiagen). The supercoiling level of the DNA was probed by agarose gel electrophoresis with SYBR Safe strain (Life Technologies), which displays the mobility difference among supercoiled, nicked and linear DNA (Tycon et al., 2012), the latter two are products of DNA photocleavage. Figure 4.6C shows that minimal DNA photocleavage occurred under our experimental conditions.

References

Abbondanzieri, E.A., Greenleaf, W.J., Shaevitz, J.W., Landick, R., and Block, S.M. (2005). Direct observation of base-pair stepping by RNA polymerase. Nature *438*, 460-465.

Aitken, C.E., Marshall, R.A., and Puglisi, J.D. (2008). An oxygen scavenging system for improvement of dye stability in single-molecule fluorescence experiments. Biophys J *94*, 1826-1835.

Bai, L., Santangelo, T.J., and Wang, M.D. (2006). Single-molecule analysis of RNA polymerase transcription. Annu Rev Biophys Biomol Struct *35*, 343-360.

Billingsley, D.J., Bonass, W.A., Crampton, N., Kirkham, J., and Thomson, N.H. (2012). Single-molecule studies of DNA transcription using atomic force microscopy. Phys Biol *9*.

Bustamante, C., Cheng, W., and Meija, Y.X. (2011). Revisiting the central dogma one molecule at a time. Cell *144*, 480-497.

Chakraborty, A., Wang, D., Ebright, Y.W., Korlann, Y., Kortkhonjia, E., Kim, T., Chowdhury, S., Wigneshweraraj, S., Irschik, H., Jansen, R.*, et al.* (2012). Opening and closing of the bacterial RNA polymerase clamp. Science *337*, 591-595.

Friedman, L.J., and Gelles, J. (2012). Mechanism of transcription initiation at an activator-dependent promoter defined by single-molecule observation. Cell *148*, 679-689.

Herbert, K.M., Greenleaf, W.J., and Block, S.M. (2008). Single-molecule studies of RNA polymerase: motoring along. Annu Rev Biochem *77*, 149-176.

Kannemeier, C., Shibamiya, A., Nakazawa, F., Trusheim, H., Ruppert, C., Markart, P., Song, Y., Tzima, E., Kennerknecht, E., Niepmann, M.*, et al.* (2007). Extracellular RNA constitutes a natural procoagulant cofactor in blood coagulation. Proc Natl Acad Sci USA *104*, 6388-6393.

Kapanidis, A.N., Margeat, E., Ho, S.O., Kortkhonjia, E., Weiss, S., and Ebright, R.H. (2006). Initial transcription by RNA polymerase proceeds through a DNA-scrunching mechanism. Science *314*, 1144-1147.

Kim, S., Blainey, P.C., Schroeder, C.M., and Xie, X.S. (2007). Multiplexed single-molecule assay for enzymatic activity on flow-stretched DNA. Nat Methods *4*, 397-399.

Kim, S., Brostromer, E., Xing, D., Jin, J., Chong, S., Ge, H., Wang, S., Gu, C., Yang, L., Gao, Y.Q.*, et al.* (2013). Probing allostery through DNA. Science *339*, 816-819.

Revyakin, A., Zhang, Z.J., Coleman, R.A., Li, Y., Inouye, C., Lucas, J.K., Park, S.R., Chu, S., and Tjian, R. (2012). Transcription initiation by human RNA polymerase II visualized at single-molecule resolution. Gene Dev *26*, 1691-1702.

Schroeder, C.M., Blainey, P.C., Kim, S., and Xie, X.S. (2008). Hydrodynamic Flow-stretching Assay for Single-Molecule Studies of Nucleic Acid-Protein Interactions. In Single-Molecule Techniques: A Laboratory Manual, P.R. Selvin, and T. Ha, eds. (Cold Spring Harbor, New York: Cold Spring Harbor Laboratory Press), pp. 461-492.

Tang, G.Q., Roy, R., Bandwar, R.P., Ha, T., and Patel, S.S. (2009). Real-time observation of the transition from transcription initiation to elongation of the RNA polymerase. Proc Natl Acad Sci U S A *106*, 22175-22180.

Tycon, M.A., Dial, C.F., Faison, K., Melvin, W., and Fecko, C.J. (2012). Quantification of Dye-mediated Photodamage During Single-molecule DNA Imaging. Anal Biochem.

Zhang, Z., Revyakin, A., Grimm, J.B., Lavis, L.D., Tjian, R., and Kadonaga, J.T. (2014). Single-molecule tracking of the transcription cycle by sub-second RNA detection. eLife *3*.

Chapter 5

Mechanism of transcriptional bursting in bacteria

Transcription of highly expressed genes has been shown to occur in stochastic bursts. But the origin of such ubiquitous phenomenon was unknown. In this chapter we present the mechanism in bacteria. Using the *in vitro* single-molecule transcription assay described in Chapter 4, we showed that positive supercoiling buildup on a DNA segment by transcription slows down transcription elongation and eventually stops transcription initiation. Transcription can be resumed upon gyrase binding to the DNA segment. Furthermore, using single-cell mRNA counting fluorescence *in situ* hybridization (FISH), we found the extent of transcriptional bursting depends on the intracellular gyrase concentration. Together, these findings prove that transcriptional bursting of highly expressed genes in bacteria is primarily caused by reversible gyrase dissociation from and rebinding to a DNA segment, changing the supercoiling level of the segment.

5.1 Background

Many recent experiments have shown the general phenomenon that transcription of highly expressed genes occurs in stochastic bursts in bacteria (Golding et al., 2005; So et al., 2011; Taniguchi et al., 2010; Zong et al., 2010) and eukaryotic cells (Suter et al., 2011). A major source of gene expression noise, transcriptional bursting results in cellular diversity of an isogenic population, possibly enhances survival of the population in the face of environmental uncertainty (Kussell and Leibler, 2005; Thattai and van Oudenaarden, 2004; Wolf et al., 2005). Golding and coworkers directly observed transcriptional bursting in real time by using MS2 loops to monitor mRNA production in *E. coli* (Golding et al., 2005). Our group reported a high-throughput single-molecule FISH assay to measure the cellular copy number distribution of a particular mRNA for a large population of isogenic *E. coli* cells (Taniguchi et al., 2010). When mRNAs are generated with a constant flux, one expects a Poisson distribution of mRNAs across the population. Bursting transcription would lead to nonPoissonian distributions. For all the highly expressed *E. coli* genes, we found that the distributions are not Poissonian, with the Fano factor (variance divided by the mean of a given distribution) larger than 1. This indicates the ubiquity of transcriptional bursting in bacteria.

However, the origin of bacterial transcriptional bursting is still unknown. Its stochasticity implies it is a single-molecule behavior: there is only one copy of the gene in the cell. Its universality implies that it cannot be attributed to a specific gene or protein factor. Rather, it must originate from a fundamental and general mechanism pertinent to the chromosomal DNA structure and its influence on transcription regulation.

Recent work showed that *E. coli* nucleoid-associated proteins such as H-NS and Fis can serve as anchoring points and create many topologically constrained loops on the chromosomal

DNA (Hardy and Cozzarelli, 2005; Wang et al., 2011). These DNA loops are 10k base pairs long on average, and the number of loops per cell is ~400 (Postow et al., 2004). Such chromosome structure provides us with a clue to explain the transcriptional bursting phenomenon (Figure 5.1). In such a DNA loop, transcription generates positive supercoiling ahead of the RNApol, and negative supercoiling behind the RNApol (Deng et al., 2004; Liu and Wang, 1987; Samul and Leng, 2007; Tsao et al., 1989; Wu et al., 1988). There exist two major topoisomerases in *E. coli* cells, gyrase and topoisomerase I (Topo I), which release positive and negative supercoiling respectively (Drlica, 1992). It is known that negative supercoiling formed during transcription elongation is rapidly removed by Topo I (Cheng et al., 2003). This is necessary because accumulation of negative supercoiling could lead to the formation of detrimental R-loops, an RNA-DNA hybrid (Drolet, 2006). The activity of gyrase, on the other hand, is not as sufficient to keep up with transcription (Guptasarma, 1996), leading to positive supercoiling accumulation on the DNA loops containing highly transcribed operons (El Hanafi and Bossi, 2000).

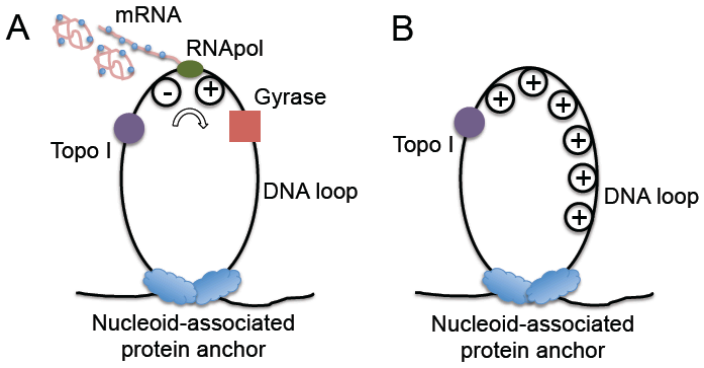

Figure 5.1 Transcription on topologically isolated chromosomal DNA loops.
(A) Gyrase releases positive supercoiling generated by transcription on a DNA loop, and RNApol keeps transcribing the gene. (B) In the absence of gyrase, active transcription on a DNA loop leads to positive supercoiling accumulation, which inhibits further transcription on the particular DNA loop.

It has been found that there are ~500 gyrase molecules per *E. coli* cell (Baker et al., 1987; Higgins et al., 1978; Liu and Wang, 1987), which happens to be roughly the number of topologically constrained DNA loops per chromosome. On average there is one gyrase molecule per DNA loop. When a gyrase molecule reacts on the DNA loop, positive supercoiling is released, and RNApol can keep transcribing the gene ("on" state, Figure 5.1right loop). In the absence of gyrase, positive supercoiling is built up by transcription, possibly slowing down transcription elongation and inhibiting further transcription initiation ("off" state, Figure 5.1left loop).

In this study, through a series of *in vitro* single-molecule and live-cell experiments, we prove that transcriptional bursting of highly expressed genes in bacteria is primarily caused by gyrase dissociation from and reversible binding to a DNA segment, such as a chromosomal loop, which changes the supercoiling level of the DNA segment.

5.2 Results

5.2.1 Positive supercoiling buildup by transcription slows down transcription elongation

We examined the effect of positive supercoiling buildup on transcription elongation *in vitro*. We designed 12 kb-long linear DNA templates with T7 or *E. coli* promoter on the 5' end, and single or multiple biotinylated nucleotides on the 3' end (Figure 5.2). On the single-biotin template, supercoiling cannot accumulate since DNA can rotate around its single linkage to the surface. In contrast, on the multiple-biotin template, DNA cannot rotate around its multiple linkages, thus positive supercoiling can accumulate downstream of the elongation complex when the complex becomes too bulky to freely spiral around the DNA (Liu and Wang, 1987; Tsao et al., 1989). Our calculation revealed that DNA starts to become positively supercoiled when a T7 transcript

longer than 250 nt is synthesized under our experimental condition (see Methods and Materials for the calculation).

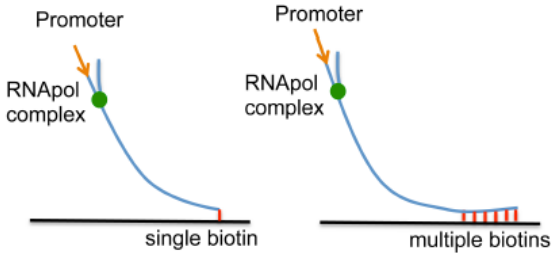

Figure 5.2 Templates for *in vitro* transcription.
The templates contain a T7 or T7A1 promoter and a 12 kb transcribing sequence. The template is anchored to the flow cell surface via either a single or multiple biotin-streptavidin linkages.

We found the average T7 transcription elongation rate is 53.2±3.4 nt/s (0.3mM each NTP, 23 °C) on the single-biotin template, which is consistent with previously reported rates (Skinner et al., 2004). This result further proved that transcription was not affected by the SYTO RNASelect dye. Interestingly, we found the positive supercoiling accumulation on the multiple-biotin template slowed down T7 transcription elongation by 38% (Figure 5.3). However, the elongation rate was recovered when gyrase was added into the system. Figure 5.4 shows the elongation rate as a function of gyrase concentration, reaching the value of the single-biotin template at a saturating gyrase concentration. As a control, we found that gyrase did not affect the elongation rate on the single-biotin template (Figure 5.4), indicating that gyrase play no other role than releasing positive supercoiling. Similarly, with *E. coli* RNApol, we found positive supercoiling accumulation on the multiple-biotin template (Figure 5.2) also slowed down transcription elongation by 47% (Figure 5.5), which is consistent with a recent report based on mechanical manipulation (Ma et al., 2013).

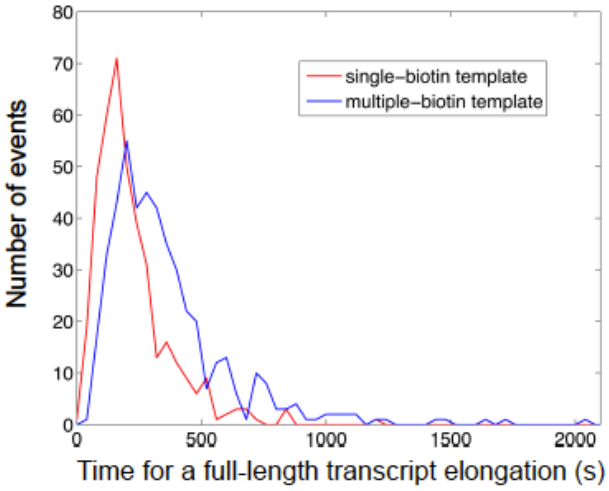

Figure 5.3 Histogram of T7 transcription elongation time.

The red curve shows the elongation time on the templates anchored with single biotin-streptavidin linkage and the blue curve shows that with multiple linkages. The average elongation time for the multiple-biotin template is 60% longer.

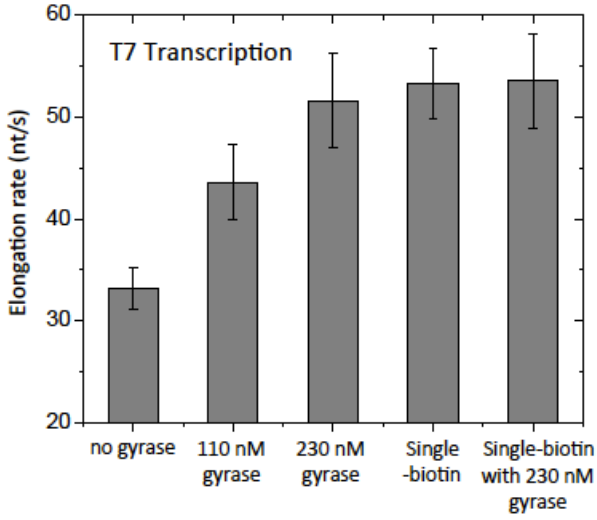

Figure 5.4 Titration of T7 transcription elongation rate with gyrase concentration.

The three bars on the left are the elongation rate on the multiple-biotin template at 23 °C. The elongation rate increases with the gyrase concentration till it gets as high as that on the single-biotin template (the 4th bar). The elongation rate on the single-biotin template does not change in the presence of a saturating concentration of gyrase (the bar on the right).

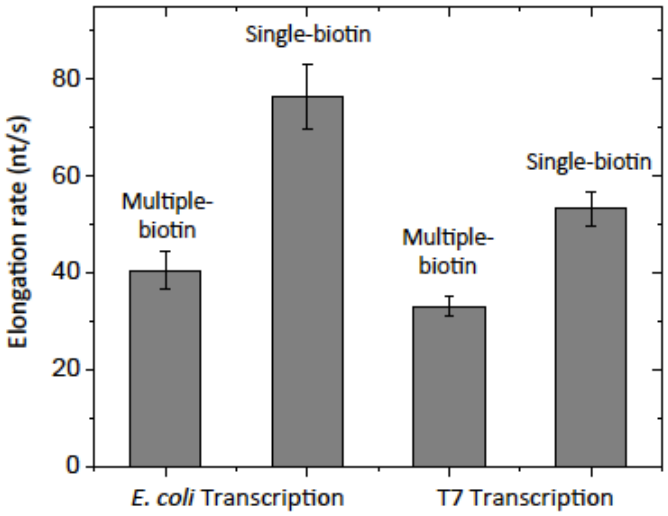

Figure 5.5 *E. coli* and T7 Transcription elongation rate.

E. coli transcription elongation rate (37 °C) and T7 transcription elongation rate (23 °C) on the multiple-biotin template are slower than on the single-biotin template.

5.2.2 K_d of gyrase-DNA complex is determined from gyrase concentration dependence of transcription elongation rates

Gyrase-DNA binding can be described by two steps (Gore et al., 2006). First, DNA and gyrase form a complex with limited protein-DNA-binding interface, which is prone to rapid dissociation. Second, a chiral DNA wrap is formed around gyrase, which in the presence of ATP generates negative DNA supercoils. Here we discuss the binding stability and kinetics of the DNA wrapping state, which are relevant to transcription dynamics.

By titrating the elongation rate on the multiple-biotin template with gyrase (Figure 5.4), we determined the gyrase-DNA dissociation constant K_d from the gyrase concentration at which the increase of the T7 transcription elongation rate reaches half of its saturation value, that is $K_d \approx$ 100 nM (Methods and Materials). This K_d is larger than previously reported 0.2~0.5 nM (Higgins and Cozzarelli, 1982; Maxwell and Gellert, 1984), where specific gyrase binding sequences were used (Morrison and Cozzarelli, 1981; Rau et al., 1987). Strong gyrase binding sites comparable to these sequences are sparsely distributed on the *E. coli* chromosome with a

frequency of only one per 100 kb (Snyder and Drlica, 1979). The *nuoB-N* DNA sequence (~12 kb) we used in our *in vitro* assay better represents a chromosomal DNA loop (~10 kb) that binds to gyrase at multiple weak binding sites (Franco and Drlica, 1988; Reece and Maxwell, 1991).

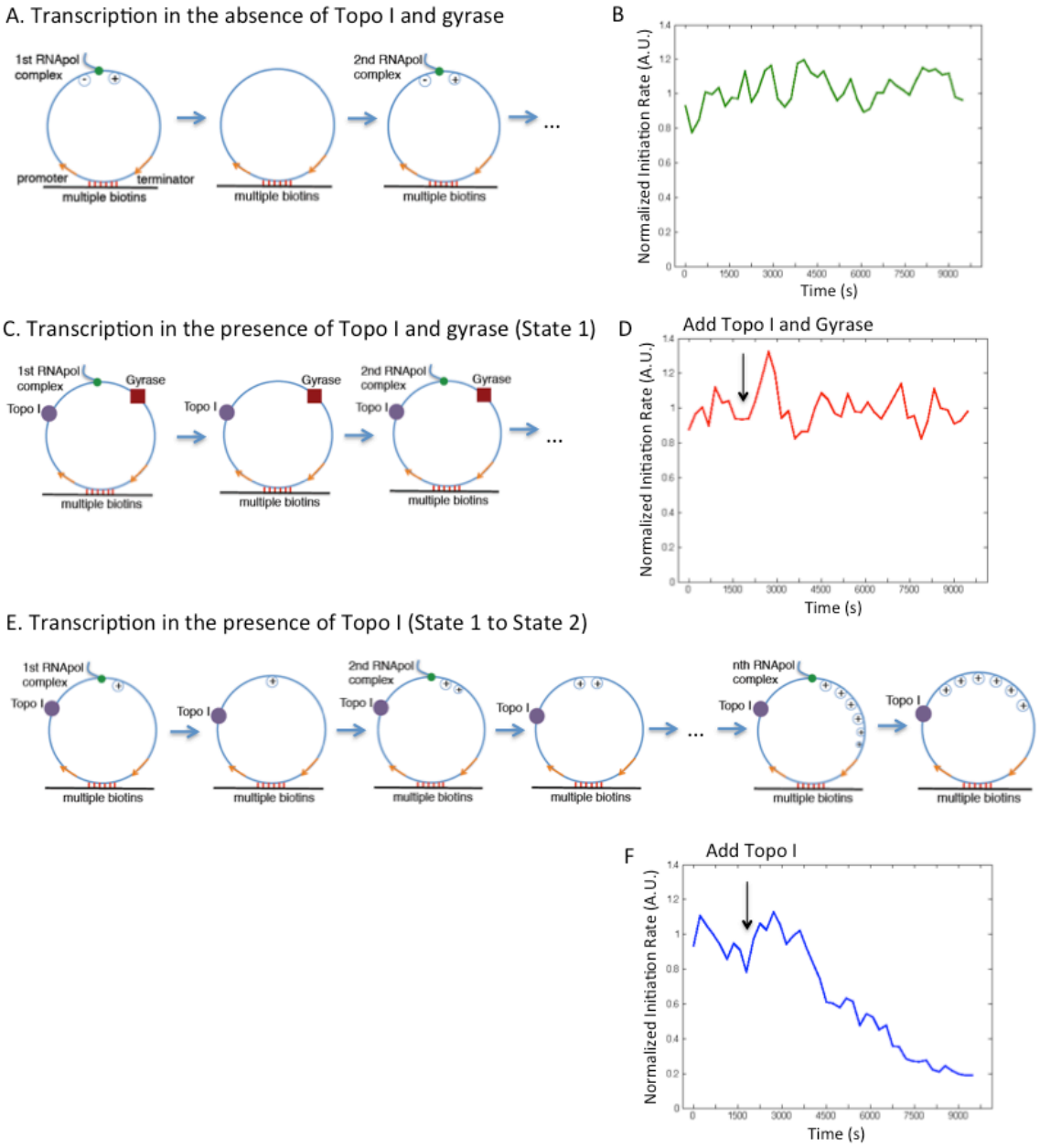

Figure 5.6 Supercoiling dependence of T7 transcription initiation rate.

(A) Schematic of transcription on a circular template in the absence of topoisomerases. Positive and negative supercoiling annihilate each other after RNApol completes transcription and dissociates from the template. (B) Time dependence of T7 transcription initiation rate under the condition of (A). (C) Schematic of transcription on the circular template in the presence of 41 nM Topo I and 0.1 μM gyrase (same as State 1 in Figure 5.15). (D) Time dependence of T7 transcription initiation rate under the condition of (C). The arrow shows the time when the topoisomerases were added into the system. (E) Schematic of transcription on the circular template in the presence of 41 nM Topo I and absence of gyrase. Positive supercoiling is built up as transcripts are produced. (F) Time dependence of T7 transcription initiation rate under the condition of (E). B, D&F are the total intensity versus time from 160 circular templates under respective conditions normalized to the same fluorescence intensity.

5.2.3 Positive supercoiling buildup by transcription stops transcription initiation

Next we examined the effect of positive supercoiling on transcription initiation. In order to mimic topologically isolated DNA loops in the bacterial chromosome, we designed a circular template (Figure 5.6A) and tethered it to the surface with multiple biotin-streptavidin linkages. The circular template consists of a T7 or *E. coli* promoter, a 12 kb-long transcribing sequence and a T7 or *E. coli* terminator. Due to the low circularization efficiency, a significant fraction of the purified DNAs remained to be linear, which are also tethered on the flow cell surface and transcribed. We picked the circular templates for analysis by staining the DNA molecules with SYTOX Orange and imaging them under flow after recording transcription movies (Methods and Materials).

For a single template under steady-state condition, transcription initiation rate is the number of initiation events over a fixed period of time (frequency of "spikes" in the intensity trajectory from a template, Figure 5.7). According to the ergodic principle, the initiation rate is the sum of initiated events from a population of templates at a specific time point. We measured the total intensity of the circular templates, which is proportional to the initiation rate.

We examined the first steady-state condition, in which T7 transcription occurs on the circular templates in the absence of Topo I and gyrase. A bulky elongation complex generates positive supercoiling ahead of it and negative supercoiling behind it, which annihilate each other when the elongation complex dissociates from the template upon transcription termination (Figure 5.6A). We found the initiation rate was indeed constant over time because of repetitive annihilation of supercoiling (Figure 5.6B).

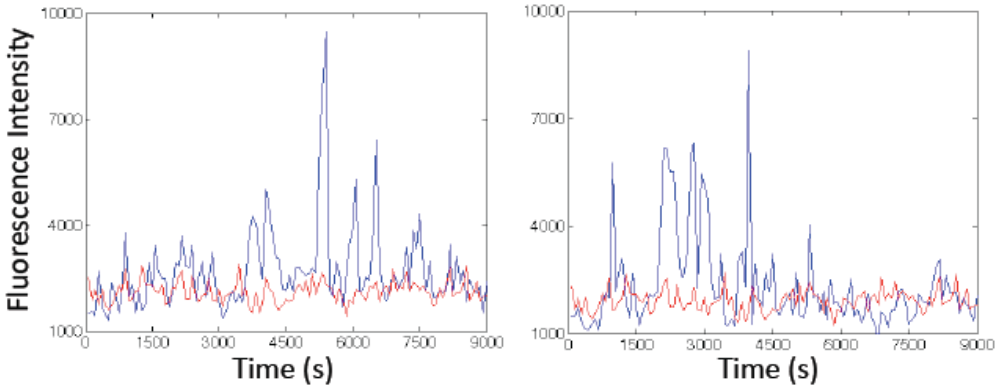

Figure 5.7 Two example fluorescence trajectories from individual circular DNA templates. The T7 RNApol concentration was 2.2 nM. A point was taken every 75 sec.

We then examined the second steady-state condition, in which T7 transcription occurs on the circular templates in the presence of both Topo I and gyrase (Figure 5.6C). Because both positive and negative supercoiling on the DNA template is continuously removed, the initiation rate remained constant over time under this condition (Figure 5.6D), which is the same as that in the first steady-state condition.

We now focus on the transition from the first steady state to a new steady state where positive supercoiling buildup would hinder further transcription initiation. Upon the introduction of Topo I, negative supercoiling should be rapidly removed, and positive supercoiling should accumulate on the circular template as multiple transcripts are made (Figure 5.6E). Indeed the initiation rate decreased over time (Figure 5.6F). Interestingly, the final intensity has dropped to under 20% of its initial value, indicating transcription initiation was essentially stopped by the buildup of positive supercoiling. This final state corresponds to the gene "off" state. We found that it takes ~9 rounds of T7 transcription to build up sufficient positive supercoiling that inhibits transcription initiation on a single template *in vitro* (Methods and Materials).

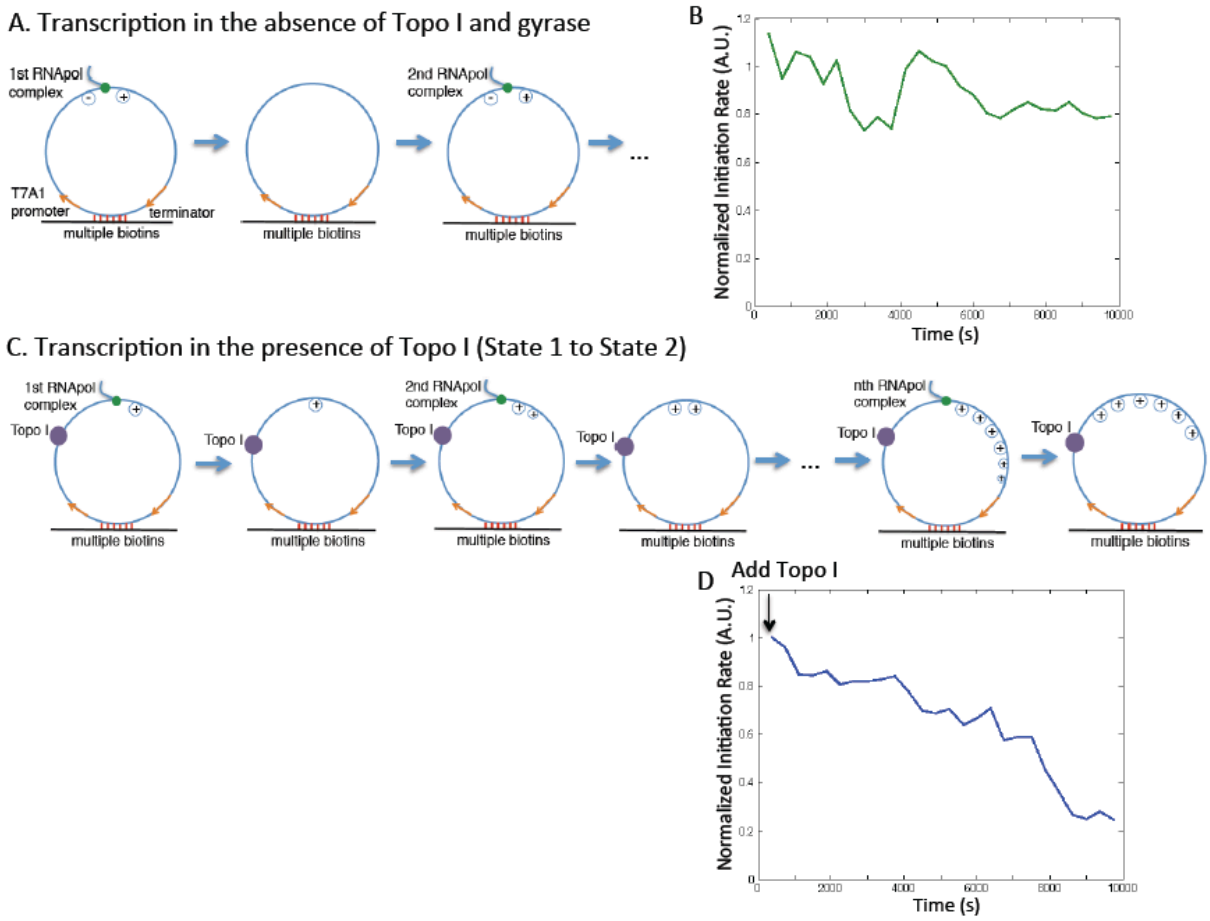

Figure 5.8 Supercoiling dependence of *E. coli* transcription initiation rate.

(A) Schematic of transcription on the circular template in the absence of topoisomerases. Positive and negative supercoiling are generated on the template as *E. coli* RNApol elongates, which annihilate each other after RNApol completes transcription and dissociates from the template. (B) *E. coli* transcription initiation rate was constant over time because of repetitive annihilation of supercoiling. The total intensity from 137 circular templates at each time point was normalized to that from 256 linear templates. (C) Schematic of transcription on the circular template in the presence of 62 nM Topo I and absence of gyrase. Positive supercoiling is built up as transcripts are produced. (D) Time dependence of *E. coli* transcription initiation rate under the condition of (C). This is the total intensity from 106 circular templates at each time point normalized to that from 209 linear templates.

Similar to T7 transcription, we found transcription initiation rate of *E. coli* RNApol dropped to ~25% after ~5 transcripts were produced from a circular template of the same length (12 kb) in the presence of Topo I (Figure 5.8). Five rounds of transcription with *E. coli* RNApol generate a frictional torque of 1 pN•nm (see Methods and Materials for the calculation), which supercoils the DNA from superhelical density $\sigma = 0$ to $\sigma_+ \approx 0.007$ (Liu and Wang, 1987). While

such frictional torque is not enough to stall the *E. coli* transcription elongation complex (Ma et al., 2013), such an increase of σ leads to significantly slower and less stable formation of *E. coli* RNApol-promoter open complex as suggested by previous report using magnetic tweezers (Revyakin et al., 2004). Therefore, the inhibition of transcription initiation is likely due to positive supercoiling that hinders the unwinding of promoter. We note that fewer than 5 rounds of transcription might be sufficient to generate the same level of supercoiling in a live cell, where the environment is more viscous and the elongation complex is more bulky due to transcription-translation coupling (Lynch and Wang, 1993).

5.2.4 Gyrase binding to positively supercoiled DNA restarts transcription

We now prove that gyrase binding on the positively supercoiled DNA restarts transcription. We started with T7 transcription on the circular templates in the presence of Topo I, generating the gene "off" state (Figure 5.9). Upon addition of gyrase into the system, transcription initiation rate started to increase and reached a plateau at the initial value of the relaxed templates (Figure 5.9), indicating that transcription initiation was fully recovered when positive supercoiling was released by gyrase.

The initiation rate versus time after the introduction of gyrase can be fitted well with a single exponential rise (Figure 5.9), suggesting a single step is rate-limiting for the transition. The rate constant is determined to be 0.78×10^{-3} s^{-1}, comparable to the pseudo-first-order gyrase-DNA binding rate constant~10^{-3} s^{-1}, which is the product between the bimolecular binding rate constant $k_{on} \approx 10^4$ M^{-1} s^{-1} under our salt concentration (Higgins and Cozzarelli, 1982) and the gyrase concentration used in our *in vitro* assay 0.1 μM. Such consistency suggests that gyrase binding to the DNA template is the rate-limiting step to restart transcription *in vitro*.

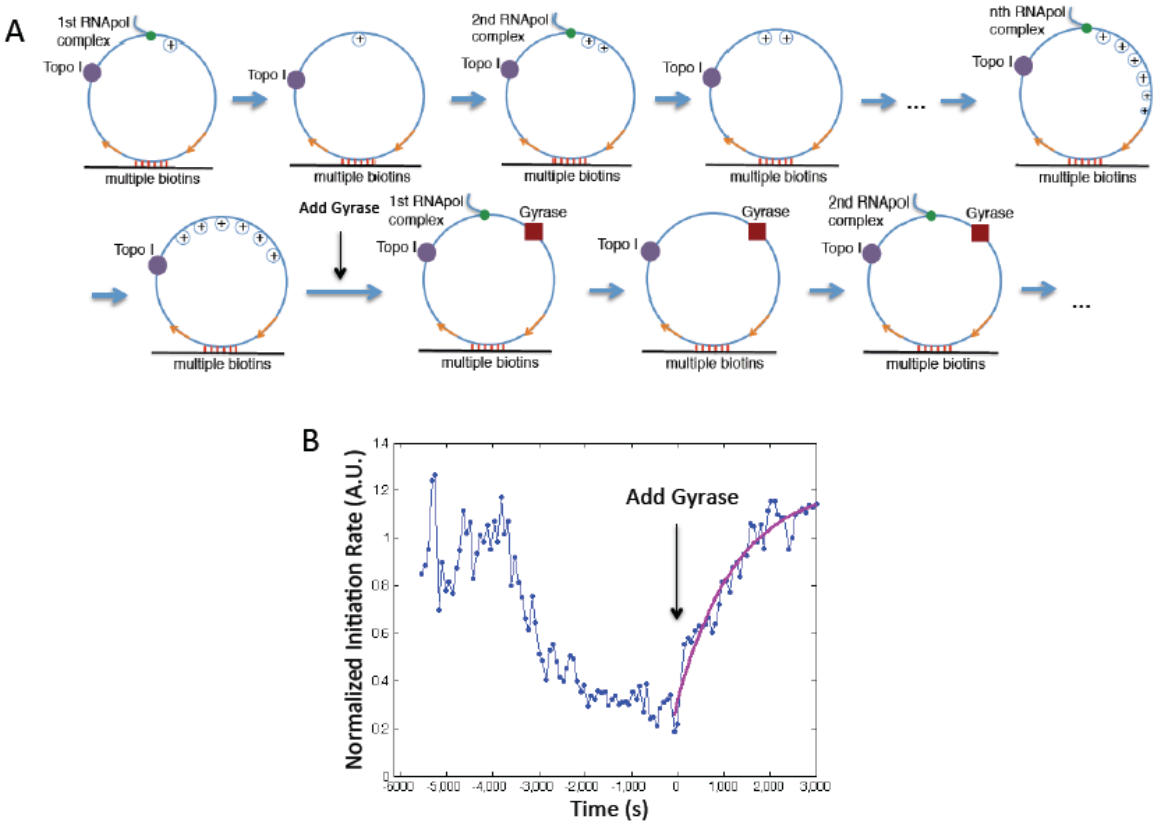

Figure 5.9 Transition from gene "off" to "on" state.

(A) Schematic of transcription on the circular template first in the presence of 41 nM Topo I only (same as Figure 5.6E), and then both 41 nM Topo I and 0.1 μM gyrase (same as Figure 5.6C). (B) Time dependence of T7 transcription initiation rate (blue) under the condition of (A). This is the total intensity from 160 circular templates at each time point normalized to that from 120 linear templates. Gyrase was added into the system at T = 0, when transcription initiation was essentially stopped by positive supercoiling accumulation. The trajectory after T = 0 is fitted with a single exponential function (magenta).

The K_d and k_{on} of gyrase-DNA binding determined *in vitro* allow us to estimate the time it takes gyrase to dissociate from and rebind to a specific chromosomal DNA loop in an *E. coli* cell. Since there are comparable number of gyrase molecules and chromosomal DNA loops per *E. coli* cell, many gyrase molecules are trapped on DNA loops. According to K_d, the intracellular concentration of unbound gyrase [G] is ~0.3 μM (see Methods and Materials for the calculation). Since k_{on} of gyrase-DNA binding is ~10^4 M^{-1} s^{-1} as determined *in vitro*, the *in vivo* pseudo-first-order rate constant for gyrase-DNA binding k_{on}•[G] is ~3×10^{-3} s^{-1}. Therefore

the average gyrase rebinding time is $1/(k_{on}\bullet[G]) \approx 6$ min. Since the dissociation rate constant of gyrase-DNA complex is $k_{off} = K_d \bullet k_{on} \approx 10^{-3}$ s^{-1}, the average gyrase dissociation time is $1/k_{off} \approx$ 17 min. The gyrase rebinding and dissociation time is in the same order of magnitude with the "off" and "on" periods of transcriptional bursting observed in live *E. coli* cells (Golding et al., 2005).

In summary, the *in vitro* experiments demonstrated that DNA positive supercoiling generated by transcription slows down both transcription initiation and elongation, and eventually stops initiation. Inhibited transcription initiation and elongation can be recovered upon gyrase binding to DNA. Therefore, accumulation and removal of positive supercoiling of a chromosomal DNA loop containing a highly expressed gene can switch the gene off and on. Next we performed live-cell experiments to further support this mechanism.

5.2.5 Positive supercoiling buildup slows down transcription elongation *in vivo*

We examined whether chromosomal supercoiling level affects transcription elongation in live *E. coli* cells. Using quantitative RT-PCR, we measured the steady-state abundance of different segments of fully induced *lac* operon mRNA under gyrase inhibition conditions. No difference in the abundance was observed throughout the transcript (Figure 5.10). This result suggests that the elongation complex does not stop or dissociate from the DNA template in the middle of one round of transcription more often when the DNA template is more positively supercoiled.

Next we measured transcription elongation rate in live *E. coli* cells using transcription initiation inhibitor rifampicin (Epshtein and Nudler, 2003) and quantitative RT-PCR (Chen, H., Shiroguchi, K., Ge, H. and Xie, X.S., unpublished data). We added rifampicin to the cell culture at time zero, and measured the mRNA abundance in multiple regions (Figure 5.11A) along the transcript at multiple time points afterwards. While the mRNA abundance at the 5' end

decreased immediately upon the addition of rifampicin, the mRNA abundance downstream started to decrease after a time delay (Figure 5.11B). The distance between the two probes on the transcript divided by the time delay was the elongation rate.

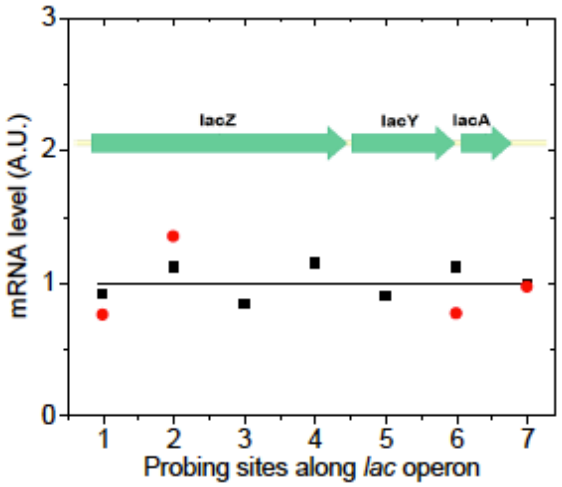

Figure 5.10 Quantitative RT-PCR measurement of the abundance of different parts of *lac* operon mRNA under fully induced condition.

x-axis: the position of probing sites along *lac* operon; y-axis: mRNA abundance. Black squares: gyrase partial inhibition by 50 ng/μL novobiocin; Red dots: gyrase complete inhibition by 10 ng/μL norfloxacin. The result indicates non-stop transcription elongation upon positive supercoiling buildup on the DNA. The abundance of each mRNA part is normalized to its abundance under wild type condition, which is plotted as the flat curve.

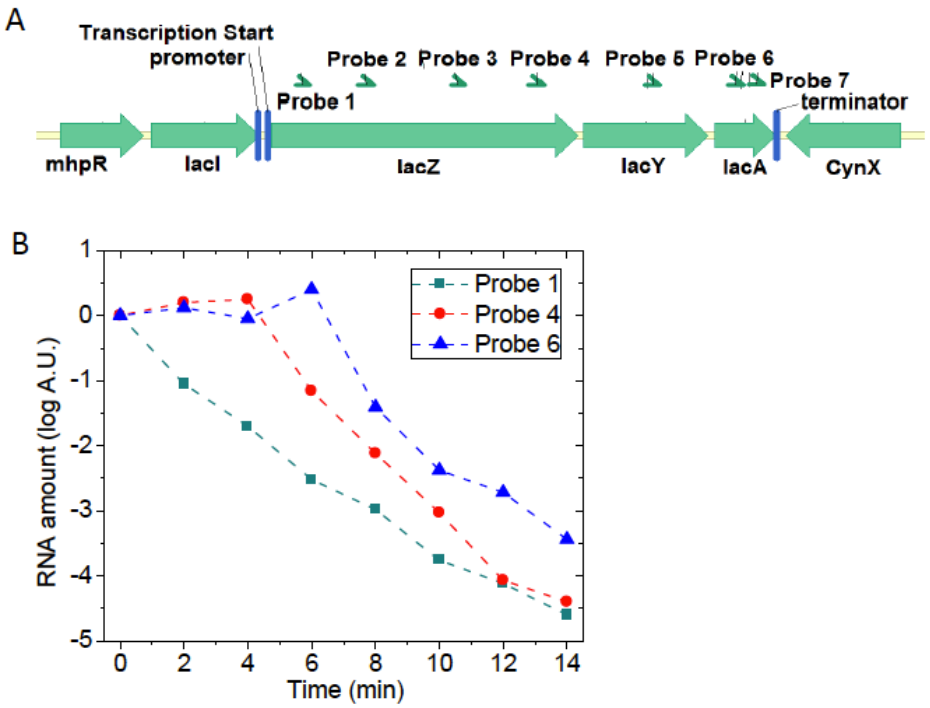

Figure 5.11 Rifampicin assay for measurement of transcription elongation rate.

(A) Seven sites on *lac* operon mRNA that were probed in the measurement of transcription elongation rate. (B) 500 ng/μL rifampicin was added into the cell culture at time zero to stop transcription initiation but not elongation. The abundance of different positions on the *lac* operon mRNA was probed by quantitative RT-PCR at multiple time points.

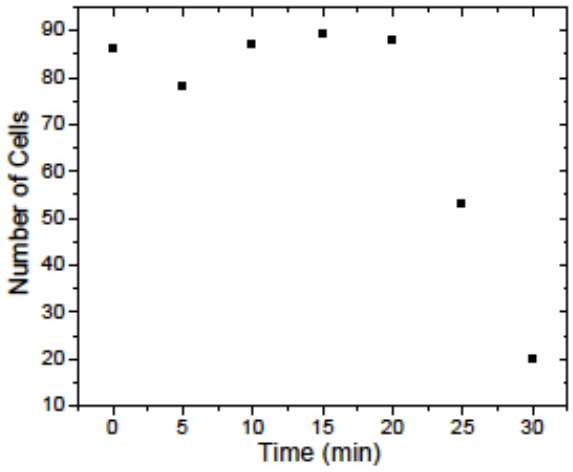

Figure 5.12 The number of *E. coli* cells (A.U.) versus time after norfloxacin treatment.

The concentration of norfloxacin was 10 ng/μL. The number of cells was measured by serial dilution, LB plating and colony counting after overnight incubation at 37°C.

Gyrase inhibition was achieved by norfloxacin treatment where most cells were viable through the 14-min long rifampicin assay (Figure 5.12). We found that the elongation rate of fully induced *lac* operon decreased by 46% upon gyrase inhibition (Figure 5.13), similar to the result previously reported by Higgins group on *Salmonella enterica* (Rovinskiy et al., 2012).

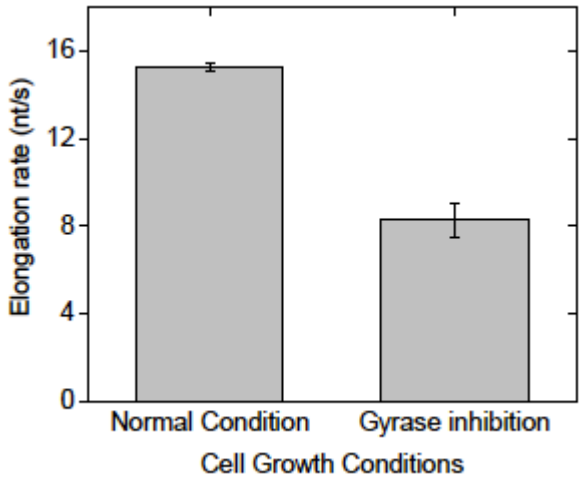

Figure 5.13 Transcription elongation rate decreased upon gyrase inhibition by 10 ng/μL norfloxacin in live *E. coli* cells.

5.2.6 A two-state model describes transcriptional bursting

Transcriptional bursting has been described with a two-state model, but the origin of the two states was not understood (Golding et al., 2005; Munsky et al., 2012; So et al., 2011). We now understand the mechanism of bacterial transcriptional bursting (Figure 5.14): the gene stochastically switches between on and off states due to release and accumulation of positive supercoiling. The "on" state (State 1) generates mRNAs with an average transcription rate k_1, and the mRNAs degrade with rate constant γ. The "off" state (State 2) does not generate any mRNA. The interconversion rate constants between the two states are α and β. α is the gene on-to-off transition rate constant due to gyrase dissociation from the DNA loop and positive supercoiling accumulation. For simplicity, we assume positive supercoiling accumulation is

fast, and gyrase dissociation is rate-limiting. β corresponds to the pseudo-first-order rate constant of gyrase-DNA binding, which is also rate-limiting in the gene off-to-on transition and proportional to the effective intracellular gyrase concentration. The lower the effective gyrase concentration is, the longer the gene stays in the "off" state and the smaller the on/off duty cycle ratio (β/α), which should result in a higher extent of bursting reflected by a larger Fano factor and a larger fraction of cells that contain zero copy of mRNA at a given time point.

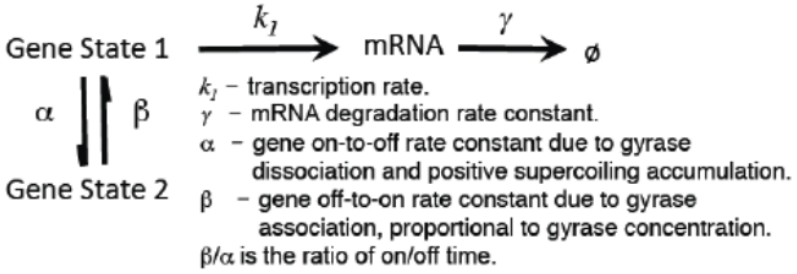

Figure 5.14 Kinetic scheme of the two-state model with relevant rate constants.

Transcription bursts of highly transcribed genes are reflected by the nonPoissonian mRNA copy number distribution. Under the condition that α and β are significantly smaller than k_1 and γ as previously observed (Golding et al., 2005), the steady-state mRNA copy number distribution for a population of cells is bimodal (Munsky et al., 2012), and can be approximated with a "Poisson with zero spike" distribution (Eq. 5.1). Based on the two-state model, the Fano factor (F) can be derived as Eq. 5.2 (Methods and Materials).

$$p(0) = \frac{\beta}{\alpha+\beta} e^{-\frac{k_1}{\gamma}} + \frac{\alpha}{\alpha+\beta};$$

$$p(n) = \frac{\beta}{\alpha+\beta} e^{-\frac{k_1}{\gamma}} \frac{\left(\frac{k_1}{\gamma}\right)^n}{n!}, n \geq 1. \qquad (5.1)$$

$$F = 1 + \frac{\alpha k_1}{(\alpha+\beta)\gamma}. \qquad (5.2)$$

We note these results hold only under the condition that gyrase dissociation and rebinding are rate-limiting, longer than the time scales of positive supercoiling accumulation and release. Although this is a simplified model, it captures the origin of transcriptional bursting, *i.e*., gyrase dissociation, and establishes the gyrase concentration dependence of β, which can now be subject to *in vivo* experimental tests.

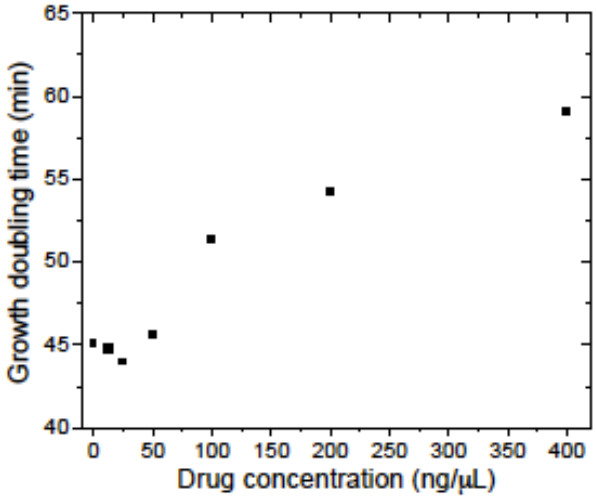

Figure 5.15 Cell growth doubling time versus various concentrations of novobiocin.
The cells were grown in M9 medium supplemented with 0.4% glucose, amino acids and vitamins at 37°C shaker. The doubling time was measured by the initial OD_{600nm} value, the final OD_{600nm} value and the time interval in between.

5.2.7 The extent of transcriptional bursting depends on intracellular gyrase concentration

We now experimentally verify this model by measuring the steady-state mRNA copy number distribution in a population of isogenic *E. coli* cells under gyrase inhibition and overexpression conditions. We performed mRNA FISH assay with single-molecule sensitivity, using a single Atto594-labeled 20-oligomer nucleotide probing the *yfp* sequence in an *E. coli* strain with the target gene fused to *yfp* sequence endogenously. By measuring the intensity of each fluorescent spot and counting the number of spots per cell, we determined cellular mRNA copy number for

thousands of *E. coli* cells. The efficiency of our single-molecule mRNA FISH assay is ~90% (Taniguchi et al., 2010).

We measured the cellular mRNA copy number distribution of the fully induced *lac* operon and 18 highly transcribed genes from the YFP library that our group has constructed (Taniguchi et al., 2010). Partial gyrase inhibition was achieved by novobiocin treatment at low concentration without affecting normal bacterial growth and morphology (Figure 5.15). We found that the cellular mRNA copy number distribution can be fitted well by the "Poisson with zero spike" distribution for the 19 genes with excellent coefficients of determination (Figure 5.16, Table 5.1). The fitting allows estimation of the on/off duty cycle ratio of transcriptional bursting (β/α), with an error bar obtained by the bootstrapping method (Brad Efron, 1993).

For fully induced *lac* operon, β/α was 1.20 for wild type, decreased to 0.73 upon gyrase inhibition, increased to 2.16 upon gyrase overexpression, and increased to 3.83 when a strong gyrase site (SGS) was inserted next to the *lac* operon (Figure 5.17). This result indicates that transcriptional bursting is sensitively dependent on the availability of gyrase to remove positive supercoiling accumulated during active transcription.

If *lac* operon is on a plasmid that lacks topological constraint, positive and negative supercoiling generated by transcription could diffuse along the circular DNA in opposite directions and annihilate each other (Figure 5.17A). As a critical control experiment, a plasmid-borne system in *E. coli* indeed showed an even higher β/α than that of gyrase overexpression, indicating minimal bursting (Figure 5.17B).

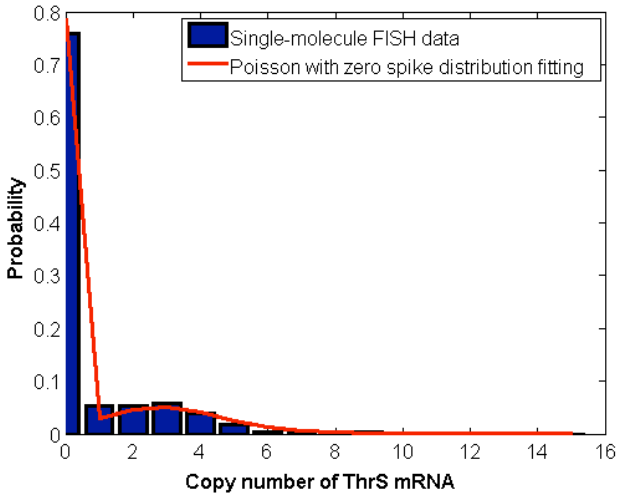

Figure 5.16 Fitting of cellular ThrS mRNA copy number distribution with "Poisson with zero spike" distribution.

Table 5.1 Coefficients of determination for the fitting of measured intracellular mRNA copy number distribution with Poisson with zero spike distribution for 18 highly expressed *E. coli* genes and fully induced *lac* operon.

Gene	Wild type	Gyrase Inhibition	Gyrase Overexpression	Strong Gyrase Site inserted
aceE	0.9750	0.9736	-	
cydA	0.9811	0.8869	-	
fabZ	0.9486	0.9994	-	
atpH	0.9939	0.9884	-	
CspE	0.9483	0.9384	-	
DnaK	0.9716	0.9806	-	
PflB	0.9914	0.9966	-	
rpoZ	0.9917	0.9986	-	
csrA	0.9073	0.8721	-	
fusA	0.9763	0.9938	-	
thdF	0.9795	0.9977	-	
fklB	0.9815	0.9949	-	
glyA	0.8274	0.8769	-	
yfiA	0.9864	0.9858	-	
hns	0.9607	0.9870	-	
sspA	0.9950	0.9999	-	
ThrS	0.9969	0.9893	-	
tufA	0.8390	0.9692	-	
lacY	0.9380	0.9804	0.9381	0.9370
plasmid-borne *lacY*	0.9634	0.9612	0.9604	

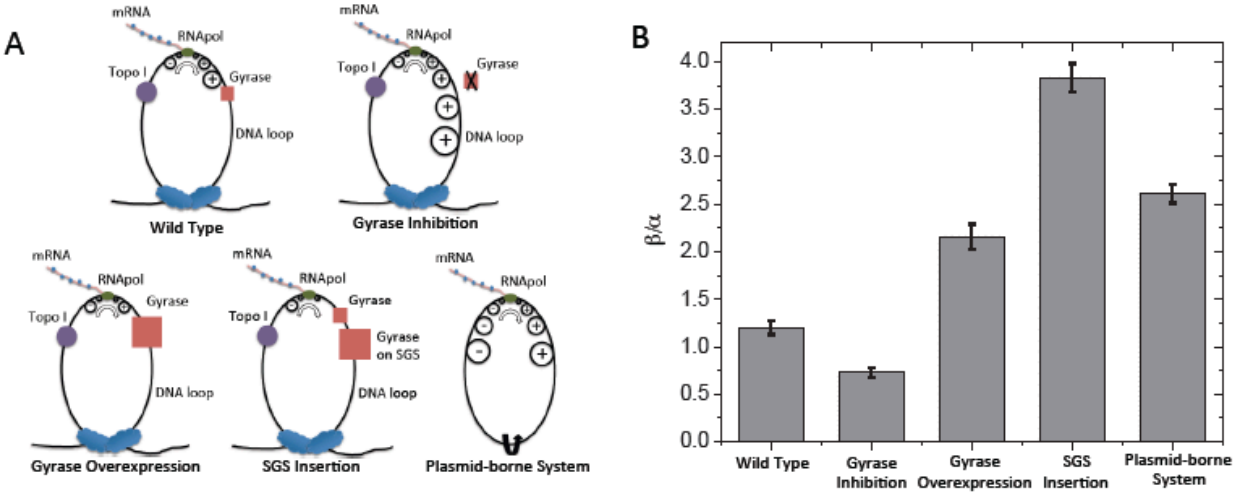

Figure 5.17 β/α changes with intracellular gyrase concentration.

(A) Schematics of interactions between effective gyrase concentration and DNA supercoiling generated by transcription under different conditions. Upon gyrase inhibition, positive supercoiling accumulates on the chromosomal DNA loop to a higher extent than wild type. Gyrase overexpression or SGS insertion is the opposite. In a plasmid-borne expression module, positive and negative supercoiling annihilate each other due to the lack of topological barriers. (B) β/α of fully induced *lac* operon decreases upon gyrase partial inhibition by 50 ng/μL novobiocin treatment, increases upon gyrase overexpression, SGS insertion, and in a plasmid-borne system.

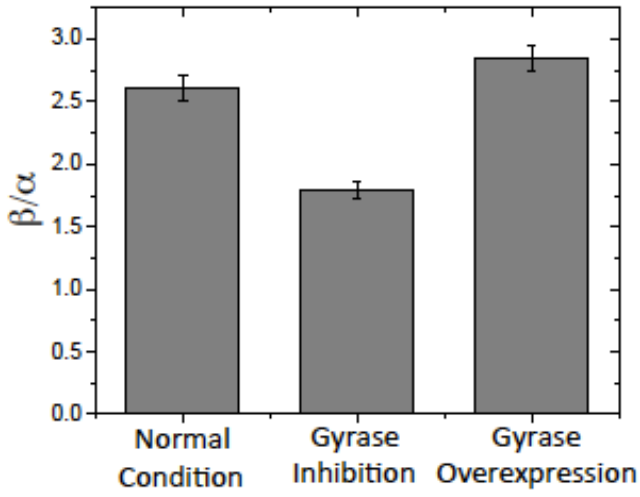

Figure 5.18 β/α decreased upon gyrase inhibition and increased upon gyrase overexpression.

Under the same conditions, β/α of the plasmid-borne system was always higher than its chromosomal counterpart (Figure 5.17B).

One would expect β/α to be infinitely large if the gene is always "on" in the complete absence of positive supercoiling accumulation. Yet it was not the case for the plasmid-borne system since there could be weak and transient topological barriers on the plasmid DNA due to transient protein binding (Leng et al., 2011). To confirm this point, we performed control experiments on the same plasmid-borne system under gyrase inhibition and overexpression conditions. We found that β/α changed in the same direction as the chromosomal gene, but to a smaller extent. Under the same conditions, β/α of the plasmid-borne system was always higher than the chromosomal counterpart, since the plasmid has much lower topological barriers and thus more efficient removal of positive supercoiling during active transcription (Figure 5.18).

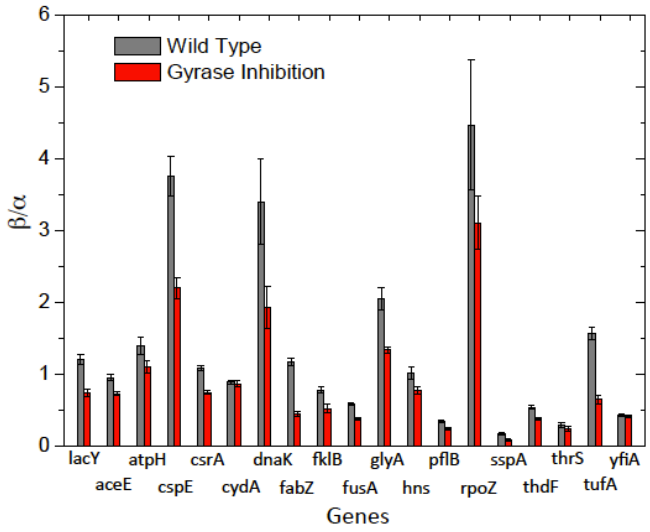

Figure 5.19 β/α of fully induced *lac* operon and other 18 highly transcribed *E. coli* genes.
β/α of all the 19 genes decrease upon gyrase partial inhibition by 50 ng/μL novobiocin treatment.

Intriguingly, similar to the scenario of fully induced *lac operon*, all the other 18 genes showed a decreased β/α (Figure 5.19) upon gyrase inhibition. In addition, most of the genes showed an increased Fano factor (Figure 5.20A) and an increased fraction of cells containing zero copy of mRNA (Figure 5.20B) upon gyrase inhibition. These findings are consistent with

the prediction based on our model and demonstrate the ubiquitous effect of gyrase concentration on transcriptional bursting.

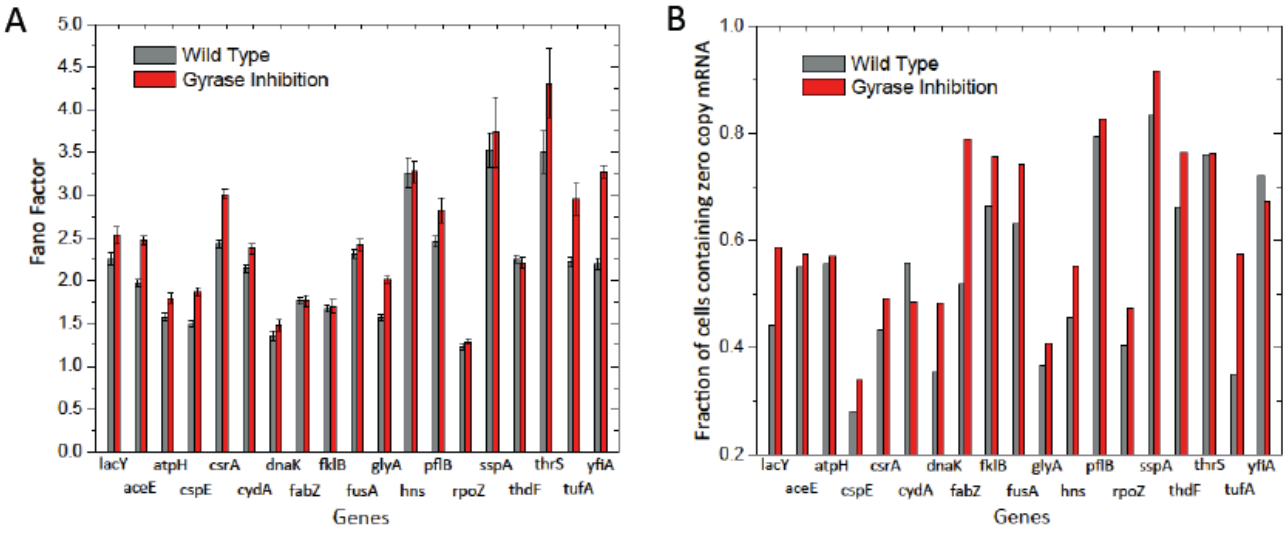

Figure 5.20 Fano factor and the fraction of cells containing zero copy mRNA both increase upon gyrase inhibition.

(A) Fano factors of steady-state intracellular mRNA copy number distribution and (B) the fraction of cells containing zero copy mRNA for fully induced *lac* operon and 18 other highly transcribed *E. coli* genes.

5.3 Discussion

5.3.1 Mechanism of transcriptional bursting under induced condition revealed

Pertinent to the fact that there is only one (or two) copy of the gene in a cell, gene expression is stochastic. In recent years, stochastic gene expression has stimulated wide interest (Blake et al., 2003; Elowitz and Leibler, 2000; Elowitz et al., 2002; Ozbudak et al., 2002; Pedraza and Paulsson, 2008). Such stochasticity, or noise, causes phenotypic variability among genetically identical cells and organisms despite identical histories of environmental exposure (Choi et al., 2008; Maamar et al., 2007), and arises from the fact that DNA, mRNA and gene regulatory proteins can be present and active at only a few copies per cell. Due to the small copy numbers and the fact that stochastic gene expression cannot be synchronized among different cells,

quantitative studies of gene expression at the single-cell level necessitates single-molecule sensitivity for mRNA and protein detection.

The stochastic gene expression dynamics of repressed genes have already been well studied and understood to date (Li and Xie, 2011). For highly expressed genes in both prokaryotic and eukaryotic organisms, bursting transcription has been demonstrated by a number of techniques, including single-molecule FISH assay that counts cellular mRNA copy number (Raj et al., 2006; Raj et al., 2010; Taniguchi et al., 2010; Zong et al., 2010), MS2 or PP7 technique that visualizes single mRNA production in real time(Chubb et al., 2006; Golding et al., 2005; Hocine et al., 2013; Larson et al., 2011; Lionnet et al., 2011; Muramoto et al., 2012), and fluorescent protein (Singh et al., 2010) or luciferase (Suter et al., 2011) as gene expression reporter in live cells. Nevertheless, the mechanism of this ubiquitous phenomenon under induced condition is not understood.

We note that the transcriptional bursting phenomenon studied in this paper is different from transcriptional pausing in prokaryotic and eukaryotic cells (Core et al., 2008; Landick, 2006; Weixlbaumer et al., 2013), which has been studied by recent single-molecule manipulation (Davenport et al., 2000; Herbert et al., 2006; Hodges et al., 2009; Ma et al., 2013; Shundrovsky et al., 2004) and RNA sequencing experiments (Churchman and Weissman, 2011; Core et al., 2008). While pausing describes intermittent elongation of a transcript, bursting describes discontinuous production of many transcripts over a much longer time scale and involves inhibition of both transcription initiation and elongation.

We have revealed the origin of stochastic transcriptional bursts in bacteria under induced conditions by conducting a series of *in vitro* and live-cell experiments, and demonstrated that reversible switching between different chromosomal supercoiling levels via gyrase dissociation

from and rebinding to a DNA loop gives rise to bursting transcription. We note this is a fundamental mechanism pertinent to the chromosome structure and should be applicable to all the highly expressed genes in prokaryotic cells and even eukaryotic cells. However, the situation of eukaryotic cells is more complex than that of bacteria due to more complicated transcription regulation and the existence of nucleosomes (Raser and O'Shea, 2004).

5.3.2 A new role of DNA supercoiling in gene expression regulation

The interaction between DNA supercoiling and gene expression in bacteria has been investigated for decades. Our knowledge comes primarily from ensemble studies on the relationship between the global DNA supercoiling level and the gene expression level. On one hand, bacterial DNA supercoiling level affects the expression of a few *E. coli* genes called supercoiling-sensitive genes (Peter et al., 2004), as well as transcription elongation rate (Rovinskiy et al., 2012) due to a combined effect of torsional and bending stress sustained by the supercoiled DNA at the transcription site (Lionberger and Meyhofer, 2010; ten Heggeler-Bordier et al., 1992). On the other hand, local DNA supercoiling level is generated by transcription, according to the "twin-domain model" developed by Wang group in late 1980s (Deng et al., 2005; Leng et al., 2011; Lim et al., 2003; Liu and Wang, 1987; Samul and Leng, 2007; Tsao et al., 1989; Wu et al., 1988). Here we report a new role of DNA supercoiling in gene expression regulation that can only be revealed by single-molecule and single-cell approaches: transient DNA supercoiling generated locally during active transcription gives rise to transcriptional bursting, which is a major source of gene expression noise that causes cell-to-cell variability in an isogenic population. Although earlier work proposed DNA supercoiling can be involved in bursting transcription (Mitarai et al., 2008; So et al., 2011), we have

experimentally proved that supercoiling dynamics is the primary origin of transcriptional bursting.

5.3.3 Other possible mechanisms of transcriptional bursting

The current report proves that stochastic changes of supercoiling level in DNA segments due to gyrase dissociation and rebinding is a main mechanism that gives rise to bursting transcription of highly expressed genes in bacteria. However, we note there could be other possible causes of bacterial transcriptional bursting, such as the change of chromosomal looping structure due to the dissociation and rebinding of nucleoid-associated proteins, as well as facilitated transcription reinitiation due to dynamical gene looping, where an operon DNA places its promoter and terminator in spatial proximity (Hebenstreit, 2013). Although they might cause transcription rate fluctuations in addition to the supercoiling effect that we observed, none of these alternative mechanisms have been experimentally proved to switch genes on and off.

5.4 Materials and Methods

5.4.1 Construction of *in vitro* transcription templates

T7 promoter sequence was placed at the 5' end of a 12 kb DNA sequence (*E. coli* operon *nuoB-N*) by PCR. *E. coli* RNApol T7A1 promoter was placed at the 5' end of a 12 kb DNA sequence (*E. coli* operon ftsL-murC) by PCR. The linear T7 or *E. coli* transcription template containing a single biotinylated nucleotide was made by PCR with 5'-end biotinylated primer (Integrated DNA Technologies, Inc.). We made a DNA fragment with multiple biotinylated nucleotides by performing PCR using a 200 bp template with arbitrary sequence, corresponding primers at both ends and dNTP mix with equal concentration of regular dTTP and biotin-16-dUTP (Biotium, Inc., Hayward, CA) (Revyakin et al., 2005). The linear transcription template with multiple biotinylated nucleotides on both strands at the 3' end was made through ligation between a 12

kb transcribing sequence and the 200 bp biotinylated fragment, followed by purification using AmPure beads (Agencourt, Beckman Coulter, Inc., Pasadena, CA).

In order to make the circular transcription templates, a linear T7 or *E. coli* transcription unit was first made by PCR, which consists of a 5'-end T7 or T7A1 promoter, a 12 kb-long transcribing sequence and a 3'-end T7 or *E. coli* rrnD terminator adapted from pET30a expression plasmid (Addgene) or *E. coli* chromosome, respectively. The termination efficiency of T7 and rrnD terminator is both >90% (Cambray et al., 2013; Telesnitsky and Chamberlin, 1989). The final circular template was made by two sequential ligation steps. The first ligation was between the linear transcription unit and the 200 bp biotinylated fragment, and the second was an intramolecular circularization. The final self-looping product was purified using λ exonuclease (New England Biolabs) and AmPure beads.

5.4.2 DNA staining assay

In order to locate the linear and circular templates in the field of view, 100 nM SYTOX Orange (Life Technologies) in 50 mM Tris-HCl buffer (pH 8.0) was used to stain the immobilized DNAs after transcription movies were recorded. Fluorescent movies were recorded under excitation of a 532 nm diode laser (UGA-250; LambdaPro, Beijing) with a power density at the focal plane above 4 W/cm^2 and an image acquisition time of 0.3 second.

The imaging buffer was kept flowing at 8 mL/hr by a syringe pump (PhD 2000, Harvard Apparatus, Holliston, MA) during the movie recording. Circular and linear DNAs with the same length were stretched to different extents under flow. With the sufficiently high laser power, the stained DNAs underwent stepwise photocleavage. A circular DNA was cut to become two linear ones that were subsequently shortened, whereas a linear DNA was shortened from the beginning (Figure 5.21).

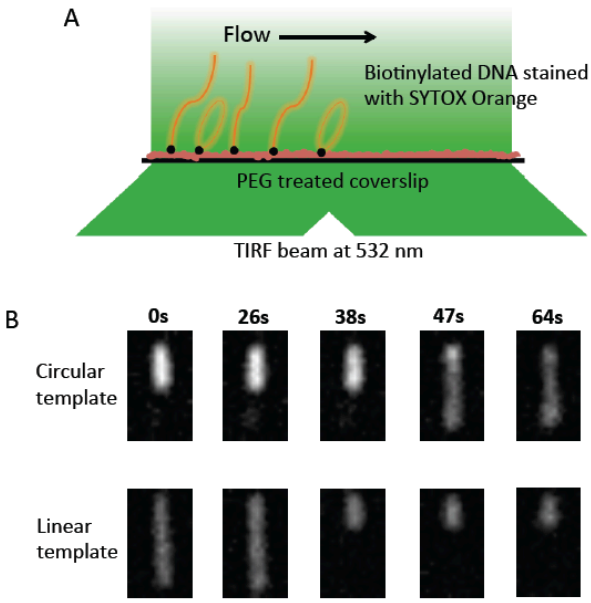

Figure 5.21 DNA staining assay for identifying circular DNA templates.

(A) Schematic representation of the experimental arrangement for the DNA staining assay (not drawn to scale). (B) Flow-stretched circular and linear DNAs behaved differently when they underwent double-strand photocleavage in the presence of SYTOX Orange. Because double-strand breaks occurred one at a time, a circular DNA appeared to "grow" first because it was cut to become two linear DNAs, one long and one short, which were shortened subsequently. However, a linear DNA could only be cut shorter and shorter.

5.4.3 Analysis of the *in vitro* single-molecule data

By overlaying an RNA movie with its corresponding DNA movie, the positions of effective DNA templates were identified in the RNA movie. For each DNA template, the fluorescence intensity in an RNA image was integrated over a 5-pixel-by-5-pixel area surrounding the DNA position. By plotting the intensity against the time when the RNA image was acquired, we generated the intensity trajectory for the template.

The intensity versus time trajectory of a template is composed of multiple peaks, each corresponding to one transcript. Under the conditions of transcription elongation rate measurements, peaks are far separated from each other in time. The elongation rate equals to the known length of a transcript divided by the elongation time, that is, the time it takes the

intensity of a transcript to rise from bottom to peak. The elongation rate under each condition was averaged from measurements of over 300 individual transcripts, with an error bar obtained by the bootstrapping method (Brad Efron, 1993).

Under steady-state conditions, transcription initiation rate at a specific time point is proportional to the sum of RNA intensity produced from a population of templates. Plotting the total RNA intensity as a function of time under a given condition includes three steps. First, we picked all the effective templates in a field of view and extracted the intensity trajectory for each of them. In order to get enough number of effective templates (>100), we performed each time-lapse measurement for multiple times. Second, we subtracted the background, i.e. the average intensity outside "peaks", from the trajectory. The background intensity is contributed from free dye in the solution and the immobilized DNA that is weakly fluorescent (Figure 4.1). After the subtraction, the remaining intensity is only from nascent RNA. Finally, we plotted the sum of intensity from all the background-free trajectories as a function of time. For T7 and *E. coli* transcription, the bin size of time was 225 s and 375 s, respectively.

There were always a mixture of linear and circular templates immobilized on the flow cell surface in our measurement of transcription initiation rates. While circular templates were used to study the effect of supercoiling accumulation on transcription initiation, linear templates served as probes of transcription initiation rate when supercoiling accumulation did not play a role. The time-dependent total intensity of linear templates reflected intrinsic variation of initiation rate during the *in vitro* measurement due to temperature, effective RNApol concentration, NTPs and pyrophosphate concentrations, degradation of the functionalized surface, etc. While the intrinsic variation of initiation rate over 9000 s was small for T7 transcription, the variation was significant for *E. coli* transcription. Therefore we normalized the

intensity from circular templates to that from linear templates in order to study the effect of positive supercoiling accumulation on *E. coli* transcription initiation rate.

In order to depict the time dependence of *E. coli* transcription initiation rate (Figure 5.8), we first got the average intensity versus time from one circular and linear template by dividing the total intensity at each time point by the number of templates, respectively. Then we normalized the average intensity from one circular template at each time point to that from one linear template. The number of circular and linear templates measured for each condition is noted in the corresponding figure caption.

To depict time dependence of T7 transcription initiation rate (Figure 5.6B, D&F), we normalized the total RNA intensity from 160 circular templates to constant fluorescence intensity 1.2×10^6. Yet in order to accurately measure the recovery rate constant of T7 transcription initiation due to supercoiling release, we normalized the average intensity from circular templates to that from linear templates (Figure 5.9).

5.4.4 Number of transcripts leading to stop of transcription initiation on a DNA template

In order to measure the fluorescence intensity generated by one transcript, we performed *in vitro* single-molecule transcription assay under the same conditions as for measurements of T7 or *E. coli* transcription initiation rates in the absence of topoisomerases, except that the T7 and *E. coli* RNApol concentration was reduced to 2.2 nM and 22 nM, respectively. With the low concentration of RNApol, transcription events on a circular DNA template were well separated temporally. Figure 5.7 shows examples of fluorescence intensity versus time trajectories of T7 transcription. One round of T7 transcription appears as a "spike" in the trajectory, and it takes 1.9 points on average for the fluorescence intensity to increase from bottom to top, according to

analysis of 226 spikes from 56 trajectories. The sum of intensity from all the points in a spike is the fluorescence intensity generated by one full transcript.

Averaging from the 226 individual transcripts, the fluorescence intensity of one full transcript was determined to be $(13.5\pm1.49)\times10^3$. The error bar was obtained by the bootstrapping method (Brad Efron, 1993). Since the total intensity generated from 160 circular templates between the moments of Topo I addition and transcription initiation inhibition (~20% of initial value) was 2.04×10^7 (Figure 5.22C), the average number of transcripts leading to the inhibition of transcription initiation on a single template was 9.44±1.05.

Averaging from 142 individual transcripts produced by *E. coli* transcription, the fluorescence intensity of one full transcript was determined to be $(16.1\pm3.24)\times10^4$. The transcript intensity was higher than that generated by T7 transcription, because of a lower *E. coli* transcription elongation rate and a lower termination rate under our *in vitro* condition, leading to a longer imaging time of a nascent transcript. The total intensity generated from 106 circular templates between the moments of Topo I addition and transcription initiation inhibition (~25% of initial value) was 9.13×10^7. Thus the average number of transcripts leading to the inhibition of initiation on a single template was 5.33±1.07.

5.4.5 Frictional torque generated during transcription elongation

The rotational frictional coefficient f_{DNA} of a DNA can be approximated to that of a cylinder (Liu and Wang, 1987; Meselson, 1972) with a radius r = 10 Å:

$$f_{DNA} = 4\pi r^2 L\eta$$

where r is the cylinder radius, L the length, η the solvent viscosity. Under our experimental condition, the T7 transcription elongation rate at room temperature is 53 nucleotides per second, equivalent to an angular velocity ω of 5 turns per second, or 10π rad•sec^{-1}.

If the transcription elongation complex does not rotate around the DNA, the DNA needs to be turned with a frictional torque τ_1:

$$\tau_1 = \omega f_{DNA} = 40\pi^2 r^2 L\eta$$

The DNA template in our experiment is 12kb long. In the aqueous solution containing 8% glycerol, $\eta = 0.012$ dyne•sec•cm^{-2}. Therefore

$$\tau_1 \approx 2\times10^{-17}\text{dyne}\cdot\text{cm}$$

If the transcription elongation complex rotates around the DNA, both T7 RNApol and the nascent RNA generate torque. According to the crystal structure data (Sousa et al., 1993), a T7 RNApol elongating on the DNA can be approximated by a sphere with a radius R_{RNApol} of 25 Å rotating around the DNA with an angular velocity ω of 10π rad•sec^{-1}. Its translational friction coefficient f_{RNApol} is:

$$f_{RNApol} = 6\pi\eta R_{RNApol}$$

The frictional force is:

$$F_{RNApol} = \omega\left(r + R_{RNApol}\right)f_{RNApol}$$

Its frictional torque is

$$\tau_2 = \left(r + R_{RNApol}\right)F_{RNApol} = 60\pi^2\eta R_{RNApol}\left(r + R_{RNApol}\right)^2 \approx 2\times10^{-19}\text{dyne}\cdot\text{cm}$$
$$\tau_2 < \tau_1$$

Therefore, T7 RNApol rotates around the DNA at the beginning of transcription.

However, as the RNApol moves along the DNA template, elongating nascent RNA rotates together with the RNApol and generates an increasing friction torque. It is reported that the radius of gyration (R_g) of a 1523 nt RNA molecule is 206 Å at a salt concentration comparable to what was used in our assay (Gopal et al., 2012). R_g scales with N^{ν}, where N is the number of nucleotides (Yoffe et al., 2008). ν is between 0.34 and 0.40, depending on polymer-solvent

interactions. Therefore the radius of a 250 nt RNA is $R_g \approx 106$ Å. The RNA can be approximated as a sphere locating $r+2R_{RNApol}+R_g$ from the center of the DNA.

$$r + 2R_{RNApol} + R_g = 166 \text{ Å}$$

The translational friction coefficient of the RNA molecule f_{RNA} is:

$$f_{RNA} = 6\pi\eta R_g$$

The frictional force is:

$$F_{RNA} = \omega\left(r + 2R_{RNApol} + R_g\right)f_{RNA}$$

Its frictional torque is

$$\tau_3 = \left(r + 2R_{RNApol} + R_g\right)F_{RNA} \approx 2\times10^{-17}\text{dyne}\cdot\text{cm}$$

$$\tau_3 \approx \tau_1$$

Therefore, the frictional torque of the transcription elongation complex exceeds that of the DNA when the nascent RNA is longer than 250 nucleotides. It is easier to rotate the DNA around its helical axis than to rotate the elongation complex around the DNA. Thus as the elongation complex further advances, the DNA downstream becomes positively supercoiled.

As the positive supercoiling builds up, however, it becomes increasingly difficult to further rotate the DNA. When the supercoiling torque equals to the frictional torque of the transcription elongation complex, the system reached a balanced point. As the elongation complex further advances, the DNA and the complex rotate in opposite directions, and the supercoiling torque grows together with the frictional torque of the elongation complex. When a full-length RNA of 12k nucleotides is synthesized by T7 transcription, the torque in the system reaches maximum $\tau_3 \approx 10^{-15}$dyne•cm = 0.1 pN•nm.

Supercoiling leads to formation of plectonemes or toroids besides twisting the DNA, which generate high bending stress near the RNApol activity site and reduces transcription elongation

rate (Lionberger and Meyhofer, 2010; ten Heggeler-Bordier et al., 1992). As a result, the elongation slowdown we observed can be attributed to a combined effect of torsional and bending stress sustained by the positively supercoiled DNA at the transcription site.

Based on the same principles, the frictional torques generated in *E. coli* transcription can be calculated. The *E. coli* transcription elongation rate at 37 °C is 76 nucleotides per second, equivalent to an angular velocity of 15π rad•sec^{-1}. When the transcription elongation complex does not rotate around the DNA, DNA needs to be turned with a frictional torque τ_1':

$$\tau_1' = 60\pi^2 r^2 L\eta \approx 3\times10^{-17}\text{dyne}\cdot\text{cm}$$

According to the cryo-electron microscopy data (Finn et al., 2000), an *E. coli* RNApol holoenzyme elongating on the DNA can be approximated by a sphere with a radius R_{RNApol}' of 75 Å. The frictional torque against its rotation around the DNA is

$$\tau_2' = 90\pi^2\eta R_{RNApol}'\left(r + R_{RNApol}'\right)^2 \approx 6\times10^{-18}\text{dyne}\cdot\text{cm}$$
$$\tau_2' < \tau_1'$$

Therefore, *E. coli* RNApol rotates around the DNA at the beginning of transcription.

As the nascent transcript elongates, the frictional torque against the rotation of an RNA molecule with radius R_g is

$$\tau_3' = 90\pi^2\eta R_g'\left(r + 2R_{RNApol}' + R_g'\right)^2$$

The radius of a 52 nt RNA is $R_g \approx$ 59 Å, the frictional torque of the corresponding elongation complex is

$$\tau_3' \approx 3\times10^{-17}\text{dyne}\cdot\text{cm}$$
$$\tau_3' \approx \tau_1'$$

As the elongation complex further advances, the DNA downstream becomes positively supercoiled. When a full-length RNA of 12k nucleotides is synthesized by *E. coli* transcription, the torque in the system reaches maximum $\tau_3' \approx 2\times10^{-15}$dyne•cm = 0.2 pN•nm. 5 transcripts

that lead to inhibition of *E. coli* transcription initiation on a circular template generate a frictional torque of 1 pN•nm, which can supercoil the DNA from relaxed state ($\sigma = 0$) to a superhelical density $\sigma_+ \approx 0.007$ (Liu and Wang, 1987).

We can estimate the frictional torque generated during transcription of an *E. coli* gene with an average gene length (1 kb) *in vivo* (Xu et al., 2006). The viscosity of *E. coli* cytoplasm η' is ~0.1 dyne•sec•cm^{-2} (Mullineaux et al., 2006). A 70S *E. coli* ribosome can be approximated as a sphere with a radius of ~110Å and a volume of ~5600 nm^3 (Stark et al., 1995), and a 1000 nt RNA molecule can be approximated as a sphere with a radius of 177 Å and a volume of ~23200 nm^3. We approximate the nascent transcript with a ribosome bound as a sphere with a volume of 28800 nm^3. Such a sphere has a radius $R_{complex}$ of ~190Å. Assuming the elongation rate is the same as measured *in vitro*, the frictional torque generated by the nascent transcript is

$$\tau = 90\pi^2\eta' R_{complex}(r + 2R'_{RNApol} + R_{complex})^2 = 2.1\times10^{-15}\ \text{dyne}\cdot\text{cm}.$$

The frictional torque generated by a 1000 nt-long transcript bound with only one ribosome *in vivo* is comparable to the frictional torque generated by a 12k nt-long naked transcript under our *in vitro* condition. If a gene is longer than 1 kb and translated faster with multiple ribosomes bound on its nascent transcript, the total frictional torque generated during transcription will be even larger. Therefore our *in vitro* assay is performed under conservative conditions, which well represent the live-cell scenario.

5.4.6 Number of T7 transcripts simultaneously elongating on a DNA template *in vitro*

We can estimate the number of T7 transcripts simultaneously elongating on a DNA template by comparing the average interval between transcription initiation events on a single template with the average elongation time of a transcript. If the former is significantly larger than the latter, then most of the time there is zero or one transcript elongating on a template.

As calculated previously, 9.44 transcripts generated from a single DNA template lead to enough positive supercoiling accumulation that inhibits T7 transcription initiation. According to Figure 5.22C, it takes 5850 sec to generate these transcripts. Therefore the average interval between transcription initiation events on a single template is

$$\frac{5850}{9.44} = 620 \text{ sec}$$

In the absence of topoisomerases (steady state 1), the total fluorescence intensity generated from 160 circular templates during 5850 sec was 3.23×10^7 (Figure 5.22A), the number of T7 transcripts per template is 15.0, and the average transcription initiation interval on a single template is 390 sec. In the presence of both Topo I and gyrase (steady state 2), the total intensity from 160 circular templates during 5850 sec was 3.14×10^7 (Figure 5.22B), the number of T7 transcripts per template is 14.6, and the average transcription initiation interval on a single template is 401 sec.

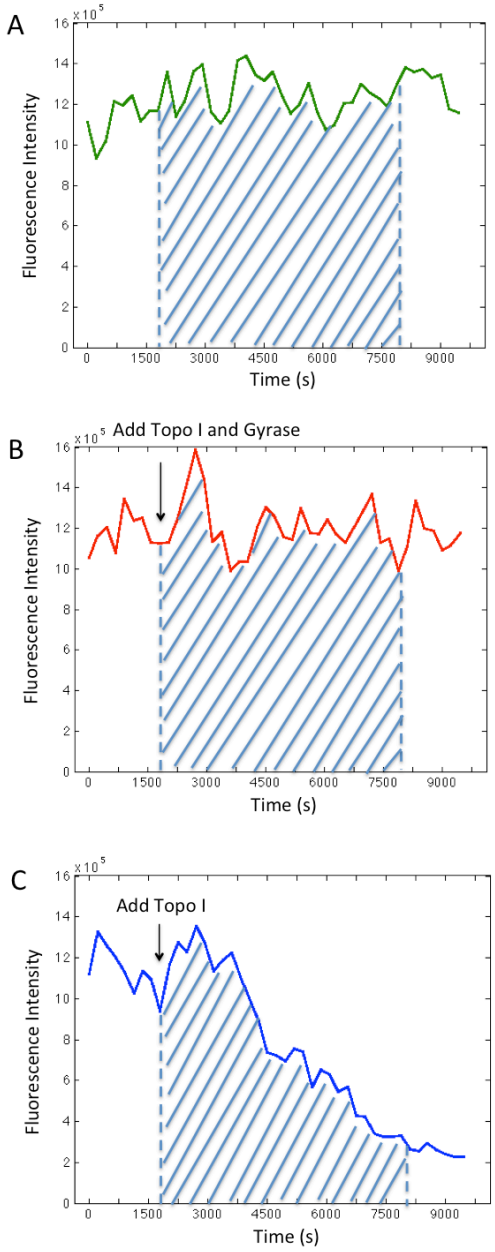

Figure 5.22 Calculation of the number of transcripts generated from an individual template under three conditions.

(A) Total intensity versus time from 160 circular templates during *in vitro* T7 transcription in the absence of topoisomerases, same as Figure 5.6A. (B) Total intensity versus time from 160 circular templates during *in vitro* transcription in the presence of 41 nM *E. coli* Topo I and 0.1 μM *E. coli* gyrase, same as Figure 5.6C. (C) Total intensity versus time from 160 circular templates during *in vitro* T7 transcription in the presence of 41 nM *E. coli* Topo I, same as Figure 5.6E. The shaded region corresponds to the total number of transcripts generated by the 160 templates between the moments of Topo I addition and transcription initiation inhibition (~20% of initial value), which covers a period of 5850 sec. The shaded regions in A and B correspond to the total number of transcripts generated by the 160 templates during 5850 sec under respective conditions.

We note that the initiation rates of steady state 1 and 2 were the same because with such a combination of T7 RNApol, Topo I and gyrase concentrations in steady state 2, positive supercoiling was generated as fast as it was released. The circular templates remained to be relaxed during the measurement. We have used 33 nM or 66 nM gyrase in the initiation rate measurement with both Topo I and gyrase, besides 100 nM gyrase as shown in Figure 5.6D&5.22B. With a lower gyrase concentration, positive supercoiling was generated faster than it was released and circular templates remained to be slightly positively supercoiled. The steady state initiation rate with 33 nM or 66 nM gyrase (data not shown) was higher than the final state in Figure 5.22C and lower than that of steady state 1 (Figure 5.22A) or steady state 2 (Figure 5.22B).

The fluorescent movies for transcription initiation rate measurements were recorded with a low temporal resolution (one frame every 75 sec), which does not allow accurate measurement of transcription elongation rates. However, the number of points it takes for fluorescence intensity to increase from bottom to top within a "spike" on the single-molecule trace provides an estimation of the total elongation time of a transcript. Since the average number of points is 1.9, the average elongation time of a T7 transcript is <150 sec, much smaller than the T7 transcription initiation interval on a single template under all three conditions as calculated above. In conclusion, most of the time there is zero or only one T7 transcript elongating on a DNA template under our *in vitro* experimental conditions.

5.4.7 K_d of gyrase-DNA complex

In the presence of gyrase, the observed T7 transcription elongation rate R_{obs} on multiple-biotin templates (Figure 5.4) is an average from a subpopulation of DNA templates with effective gyrase binding and a subpopulation of free DNA templates, which differ in elongation rates. We

assign the elongation rate on a free multiple-biotin DNA template to be R_D and the elongation rate on a gyrase-bound multiple-biotin DNA template to be R_{DG}. If the percentage of gyrase-bound DNA is x, then the average elongation rate R_{obs} is

$$R_{obs} = (1 - x)R_D + xR_{DG}.$$

Accordingly, when R_{obs} reaches half of the plateau value in the titration experiment, that is

$$R_{obs} = 0.5(R_D + R_{DG}),$$

50% of all the DNAs are gyrase-bound, the corresponding gyrase concentration equals to K_d. From Figure 5.4, K_d of gyrase-DNA complex is approximately 100 nM.

In a live *E. coli* cell, there are comparable number of gyrase molecules and chromosomal DNA loops (400~500) in a cell volume V, where V is ~0.6 μm^3 (Kubitschek, 1990). For simplicity, we take 450 as the intracellular number of both molecules. Many gyrase molecules are trapped on chromosomal DNA loops. Assuming a DNA loop has one gyrase molecule binding at a time, there are the same number (X) of unbound gyrase molecules and unbound DNA loops. Based on the definition of dissociation constant of gyrase-DNA complex, we have

$$K_d = \frac{(X / N_A / V)^2}{(450 - X) / N_A / V} \qquad (5.3)$$

where N_A is the Avogadro constant. By solving Eq. 5.3, we get X equals to 111, which corresponds to an intracellular concentration of 0.3 μM. This is 25% of the total gyrase concentration. For a specific DNA loop, the fraction of time when it is unbound to gyrase is 25%.

5.4.8 Bacterial genetic constructs

The *lac* operon of *E. coli* strain BW25993 was fused endogenously to *yfp* (*venus)* gene (Nagai et al., 2002) at the 3' end of *lacY* gene via λ-red recombination (Datsenko and Wanner, 2000). The kanamycin resistant gene used for screening was subsequently removed via FRT

recombination (Datsenko and Wanner, 2000). A strong gyrase site (SGS) nuB1 sequence (Pato et al., 1990) was inserted upstream of the *lac* operon also via λ-red recombination, where the *lacY* gene was already tagged with *venus* gene. The 18 library strains with *venus* fused to the 3' end of each target gene were obtained from our YFP library from previous work (Taniguchi et al., 2010).

The plasmid-borne *lac* operon expression system was made by inserting the whole *lac* operon sequence (including the *lacI*gene and *venus* fusion with *lacY*) into a single-copy plasmid backbone pVS133 based on the *parABC* partitioning system. The plasmid was then electroporated into *Δlac* BW25993 bacterial cells and maintained by carbernicillin resistance. We note that even with the partition system, there might be cells with 2 plasmids occasionally. This gene dosage variation may slightly contribute to the nonPoissonian mRNA distribution.

The gyrase overexpression plasmid was made based on a pBAD expression system with kanamycin resistance. *E. coli* genes *gyrA* and *gyrB* were placed in a polycistronic manner, using their original ribosome binding sites to maintain physiological stoichiometry of the two subunits. A final 0.2% L-arabinose (Sigma-Aldrich) was used to induce gyrase overexpression from the plasmid.

5.4.9 Rifampicin Assay (Adapted from Chen, H., Shiroguchi, K., Ge, H. and Xie, X.S., unpublished protocol)

At time zero, 500 ng/μL rifampicin was added to stop transcription initiation but not on-going elongation. 10 ng/μL norfloxacin was added simultaneously to inhibit gyrase activity in the cell. 8 cell samples were taken out and immediately fixed for later mRNA quantification analysis at multiple time points with 2-minute interval, at 0, 2, 4, 6, 8, 10, 12, 14 minutes following the drug treatment, respectively. The mRNA abundance of the 7 probes along *lac* operon from 5'

end to 3' end was measured for all 8 samples, as shown in log scale in Figure 5.11B. A final result of the transcription elongation rate measurement was shown in Figure 5.13.

5.4.10 Bacterial mRNA Extraction and Quantitative RT-PCR

Upon harvest, 1/10 volume of ice-cold 90:10 ethanol:phenol mixture was added to the cells followed by centrifuge and PBS wash. The cells were then lysed by lysozyme treatment and supplemented with spike-in RNA for absolute quantification. RNA was purified from the cell lysis by phenol:chloroform extraction, isopropanol precipitation and 70% ethanol wash for several times. Following DNA removal by DNase I treatment, RNA product was purified with a purification column (R1015, Zymo Research), quantified (Nanodrop 2000, Thermo Fisher Scientific Inc., Waltham, MA) and converted to cDNA by M-MuLV reverse transcription (New England Biolabs). Quantitative RT-PCR was performed to determine the mRNA amount using SYBR qPCR Master Mix and ROX dye (Finnzymes, Thermo Fisher Scientific Inc.).

5.4.11 Killing curve measurement upon drug treatment

LB plating and colony counting following serial dilution in LB medium was used to measure the *E. coli* cell killing curve upon 10 ng/μL norfloxacin treatment (Figure 5.12), which was the same condition as the rifampicin assay for live-cell transcription elongation rate measurement. Figure 5.12 shows that the cell number was almost constant within the first 20 minutes after drug treatment, and decreased afterwards. Since our rifampicin assay was performed within the first 14 minutes after norfloxacin treatment, cell death was not a major issue and would not affect final results.

5.4.12 Growth rate measurement upon drug treatment

OD_{600nm} was measured to monitor the growth rate upon novobiocin treatment at various concentrations, and the doubling time was calculated from the initial OD value, the final OD

value and the incubation time in between. Cells were grown at 37°C in M9 medium with 0.4% glucose supplemented with amino acids and vitamins, the same condition as that for the mRNA FISH assay. Figure 5.15 shows that the growth rate starts to decrease in the presence of ~100 ng/μL novobiocin (Sigma-Aldrich), and keeps dropping as the drug concentration further increases. Our gyrase inhibition condition for mRNA FISH assay was 50 ng/μL novobiocin, under which the cells maintained the same growth rate as that without drug treatment. In addition, there was no cell morphology change upon 50 ng/μL novobiocin treatment for several hours as observed under microscope (data not shown). From the growth rate measurements and cell morphology observations, we conclude that gyrase partial inhibition under our mRNA FISH assay condition did not affect normal physiology of *E. coli* cells, yet allowed us to study the role of gyrase activity in transcriptional bursting.

5.4.13 mRNA single-molecule FISH assay

The BW25993 *E. coli* cells were grown in M9 medium with 0.4% glycerol supplemented with amino acids and vitamins, together with antibiotics and 1 mM IPTG if necessary. The cells were subsequently inoculated 1:500 into the same medium and incubated for ~7 hrs at 37°C with 250 rpm shaking till OD_{600nm} reached 0.2~0.3. 50 ng/μL novobiocin was added into the medium and incubated for another 2 hrs before harvest. 2 hrs was long enough (several cell cycles) to allow all the cells to enter steady state, and thus minimized potential cell-to-cell variation due to different transition kinetics in response to the drug treatment.

The YFP library strains were grown in LB medium with chloramphenicol at 30 °C. The cells were subsequently inoculated 1:400 into M9 medium with 0.4% glucose supplemented with amino acids and vitamins and incubated for 11 hrs at 30°C with 250 rpm shaking till

OD_{600nm} reached 0.2~0.3. 50 ng/μL novobiocin was added and incubated for another 2 hrs before harvest.

Upon harvest, the cell culture was mixed with the same volume of ice-cold 2X fixation buffer followed by brief vigorous shaking and 15-min incubation on ice. The 2X fixation buffer consists of 2X RNase-free PBS (Ambion, Life Technologies, Carlsbad, CA) and 6.4% formaldehyde (Electron Microscopy Sciences, Hatfield, PA) in RNase-free water (Ambion). After fixation, the cells were pelleted down by 4700 rpm spinning for 3 min and washed twice in 1 mL ice-cold PBS (Ambion). After the final wash, the cells were first resuspended in ~20 μL PBS and then mixed with 1 mL 70% ethanol for 1-hr incubation at room temperature. After that, the cells were pelleted down by 7000 rpm spinning for 1 min.

The pelleted cells were then washed in 1 mL wash buffer and resuspended in ~20 μL wash buffer. 10 μL of pelleted cells were added to 51.5 μL hybridization mixture described below, and mixed well via tapping and inverting without introducing bubbles. The final hybridization assay was incubated in the dark at 30°C for 9 to 12 hrs. After the incubation, the cells were washed twice with 100 μL wash buffer and incubated in the dark at 30°C for 1 hr. The cells were then washed once with 100 μL wash buffer, twice with 100 μL PBS, and finally resuspended in 15 to 20 μL PBS.

In the FISH assay, the hybridization buffer consists of 2X SSC solution (Ambion), 0.2 mg/mL BSA (New England Biolabs), 2 mM RVC (Ribonucleoside Vanadyl Complex; Sigma-Aldrich), 10% dextran sulfate (MW > 500,000; Sigma-Aldrich), 0.1% *E. coli* transfer RNA (Sigma-Aldrich), and 22.1% formamide (Applied Biosystems, Life Technologies). The wash buffer consists of 22.1% formamide and 2X SSC solution in RNase-free water. The FISH probe is a 20-mer oligodeoxynucleotide (Venus495r, 5' – TCCTCGATGTTGTGGCGGAT – 3') with

a dye molecule Atto 594 covalently linked on the 5' end through NHS ester reaction followed by RNase-free HPLC purification (custom made by Sigma-Aldrich). A 50 nM FISH probe solution was made by mixing 1 μL 5 μM FISH probe solution, 10 μL 2 mg/mL BSA (New England Biolabs) and 90 μL RNase-free water (Ambion). The hybridization mixture was made by mixing 50 μL hybridization buffer with 1.5 μL 50 nM FISH probe solution.

5.4.14 mRNA FISH imaging sample preparation, microscopy and data analysis

The 35 mm petri dishes (with 14 mm microwell and No. 1.0 coverglass; MatTek Inc., Ashland, MA) were cleaned with the following procedure: 30-min sonication in 1 M potassium hydroxide, 30-min sonication in purified water, blow-dry with nitrogen gas, 10-min cleaning in plasma cleaner, and rinse with purified water. Then the petri dishes were incubated for 1 hr at room temperature with 2 mL 0.033% poly-l-lysine (Sigma-Aldrich) filtered by 0.2 μm syringe filters (Pall Corporation, Northborough, MA). The residual poly-l-lysine solution on the dish was removed completely by rinse with purified water and blow-dry with nitrogen gas. 15 to 20 μL cell culture was applied to the coverglass region of the dish and incubated at room temperature for 1 to 1.5 hrs in the dark while covered to prevent evaporation, allowing cell attachment to the poly-l-lysine coated coverslip surface. After the incubation, we gently applied PBS solution to rinse the coverslip surface and wash away the unattached cells. After several times of wash, 2 mL of PBS with 140 mM 2-mercaptoethanol was applied to the dish. By then, the sample was ready for imaging.

An Olympus IX81 microscope with a 100X NA 1.35 phase-contrast objective and an EMCCD (Evolve, Photometrics, Tucson, AZ) was used. For imaging of Atto 594, a 580 nm fiber laser (VFL-P-Series, MPB Communications Inc., Canada) was used. The fluorescence filter set includes an excitation filter (HQ575/50X, Chroma Technology Corp), a dichroic mirror

(z594rdc, Chroma), and an emission filter (D635/55M, Chroma). The laser intensity at the focal plane was ~100 W/cm^2. The acquisition time of each image was 1000 ms. For phase contrast imaging of cell morphology, the same filter set and a build-in lamp in the microscope were used. The acquisition time of each image was 100 ms. Phase contrast and Atto 594 images were acquired for multiple fields of view for each strain. The total number of cells imaged for each condition is ~4000 on average after cell size filtering. Images without laser excitation were recorded as the offset level, and fluorescent images of diluted dye solutions were recorded to correct for slight illumination inhomogeneity across the field of view.

Fluorescent spots corresponding to localized mRNA molecules were identified with a peak-searching algorithm written in Matlab. The algorithm searches for pixels that have both (i) intensity above a pre-defined threshold and (ii) image curvature above a pre-defined threshold. The thresholds were determined by eyeballing, such that all the identified peaks correspond to actual fluorescent spots. For each fluorescent spot, the fluorescence intensity above background was integrated over a 5-pixel-by-5-pixel area (corresponding to 800×800 nm) surrounding the peak. If more than one peak were identified within the 5-pixel-by-5-pixel area in the same cell, the masks were merged so that each pixel is counted only once. To compensate for gene dosage and cell cycle difference between cells, only a small subset of cells within a certain range of cell size (1.92 μm^2 to 2.30 μm^2) were used for mRNA copy number counting. The calibration of single-molecule fluorescence and the quality control of single-molecule FISH false-positive and false-negative rates were performed as previously described (Taniguchi et al., 2010).

5.4.15 Gyrase inhibition and overexpression effects on transcriptional bursting of plasmid-borne fully induced *lac* operon

For the gyrase inhibition assay, *E. coli* cells containing a plasmid-borne *lac* operon expression module were grown in M9 medium supplemented with 0.4% glycerol plus amino acids and vitamins. 50 ng/μL carbernicillin and 1 mM IPTG were added to maintain the plasmid and fully induce *lac* operon expression, respectively. When the OD_{600nm} value of the cell culture reaches 0.2 to 0.3, 50 ng/μL novobiocin was added into the mixture, which was incubated for 2 hrs before cell harvest.

For the gyrase overexpression assay, *E. coli* cells containing a plasmid with *lac* operon expression module and a plasmid with gyrase overexpression module were grown in M9 medium supplemented with 0.4% glycerol, amino acids and vitamins, in the presence of 50 ng/μL carbernicillin, 35 ng/μL kanamycin and 1 mM IPTG. When the OD_{600nm} value of the cell culture reaches 0.2 to 0.3, 0.2% L-arabinose was added into the mixture to induce gyrase overexpression, which was incubated for 2 hrs before cell harvest. The mRNA FISH results are shown in Figure 5.18.

5.4.16 "Poisson with zero spike" distribution for cellular mRNA copy number

The transcriptional bursting phenomenon can be described by a two-state model:

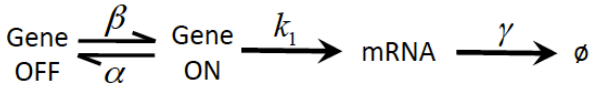

,

where k_1 is average transcription rate; γ is mRNA degradation rate constant; α is the transition rate constant from gene "on" to "off" state, limited by gyrase dissociation rate; and β is the transition rate constant from gene "off" to "on" state, limited by gyrase association rate.

Each state of the system can be described by both the gene state and the copy number of mRNA. The transition between different states of the system can be illustrated by the following diagram:

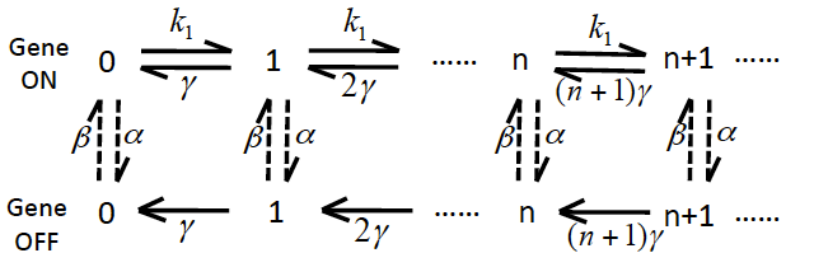

where *n* represents the state with *n* copies of mRNA.

The corresponding Chemical Master Equations are

$$\frac{dp_1(n)}{dt} = \beta p_2(n) - \alpha p_1(n) + k_1 p_1(n-1) - k_1 p_1(n) + (n+1)\gamma p_1(n+1) - n\gamma p_1(n);$$
$$\frac{dp_2(n)}{dt} = \alpha p_1(n) - \beta p_2(n) + (n+1)\gamma p_2(n+1) - n\gamma p_2(n),$$

Where $p_1(n)$ is the probability of the "on" gene to occupy state *n*, and $p_2(n)$ is the probability of the "off" gene to occupy state *n*.

At steady state, we just set the right-hand-side of the Chemical Master Equations to be zero. Then we denote p_1 as the probability for the gene to be "on", and $p_2$as the probability for the gene to be "off". We have

$$p_1 + p_2 = \sum_{n=0} (p_1(n) + p_2(n)) = 1,$$

and $\alpha p_1 = \beta p_2$, hence at steady state, we have

$$p_1 = \sum_{n=0} p_1(n) = \frac{\beta}{\alpha+\beta}$$
$$p_2 = \sum_{n=0} p_2(n) = \frac{\alpha}{\alpha+\beta}$$

Assuming α and β are much smaller than k_1 and γ, the cells separate into distinct On and Off populations. For the On population, cellular mRNA copy number follows Poisson distribution, that is

$$p_1(n) \approx p_1 e^{-\frac{k_1}{\gamma}} \frac{\left(\frac{k_1}{\gamma}\right)^n}{n!} = \frac{\beta}{\alpha+\beta} e^{-\frac{k_1}{\gamma}} \frac{\left(\frac{k_1}{\gamma}\right)^n}{n!}$$

For the Off population, cellular mRNA copy number is always zero, i.e.

$$p_2(0) \approx p_2 = \frac{\alpha}{\alpha+\beta}, p_2(n) = 0, n \geq 1$$

The overall distribution is "Poisson with zero spike", i.e.

$$p(0) = p_1(0) + p_2(0) = \frac{\beta}{\alpha+\beta} e^{-\frac{k_1}{\gamma}} + \frac{\alpha}{\alpha+\beta};$$

$$p(n) = p_1(n) + p_2(n) = \frac{\beta}{\alpha+\beta} e^{-\frac{k_1}{\gamma}} \frac{\left(\frac{k_1}{\gamma}\right)^n}{n!}, n \geq 1.$$

For a more rigorous derivation, refer to (Shi and Qian, 2011).

Next we derive the equation of Fano factor based on the "Poisson with zero spike" distribution. The steady-state mean cellular mRNA copy number is

$$\langle n \rangle = \sum_{n=0} n p(n) = \frac{\beta k_1}{(\alpha+\beta)\gamma}.$$

The steady-state variance is

$$\operatorname{var} n = \sum_{n=0} n^2 p(n) - \langle n \rangle^2 = \frac{\beta k_1 \gamma(\alpha+\beta) + \alpha\beta k_1^2}{(\alpha+\beta)^2 \gamma^2}.$$

Therefore the Fano factor is

$$F = \frac{\operatorname{var} n}{\langle n \rangle} = 1 + \frac{\alpha k_1}{(\alpha+\beta)\gamma}.$$

In our two-state model, the average gene "on" state transcription rate k_1 is gene-specific and affected by factors like the global chromosomal supercoiling level via supercoiling-sensitive protein-DNA binding dynamics. As a result, gyrase concentration correlates well with the extent of transcriptional bursting (reflected by β/α), but not necessarily with the average mRNA abundance (k_1/γ) in live *E. coli* cells.

References

Baker, T.A., Funnell, B.E., and Kornberg, A. (1987). Helicase action of dnaB protein during replication from the Escherichia coli chromosomal origin in vitro. J Biol Chem *262*, 6877-6885.

Blake, W.J., M, K.A., Cantor, C.R., and Collins, J.J. (2003). Noise in eukaryotic gene expression. Nature *422*, 633-637.

Brad Efron, R.T. (1993). An Introduction to the Bootstrap (CRC Press).

Cambray, G., Guimaraes, J.C., Mutalik, V.K., Lam, C., Mai, Q.A., Thimmaiah, T., Carothers, J.M., Arkin, A.P., and Endy, D. (2013). Measurement and modeling of intrinsic transcription terminators. Nucleic Acids Res *41*, 5139-5148.

Cheng, B.K., Zhu, C.X., Ji, C.L., Ahumada, A., and Tse-Dinh, Y.C. (2003). Direct interaction between Escherichia coli RNA polymerase and the zinc ribbon domains of DNA topoisomerase I. J Biol Chem *278*, 30705-30710.

Choi, P.J., Cai, L., Frieda, K., and Xie, X.S. (2008). A stochastic single-molecule event triggers phenotype switching of a bacterial cell. Science *322*, 442-446.

Chubb, J.R., Trcek, T., Shenoy, S.M., and Singer, R.H. (2006). Transcriptional pulsing of a developmental gene. Curr Biol *16*, 1018-1025.

Churchman, L.S., and Weissman, J.S. (2011). Nascent transcript sequencing visualizes transcription at nucleotide resolution. Nature *469*, 368-373.

Core, L.J., Waterfall, J.J., and Lis, J.T. (2008). Nascent RNA sequencing reveals widespread pausing and divergent initiation at human promoters. Science *322*, 1845-1848.

Datsenko, K.A., and Wanner, B.L. (2000). One-step inactivation of chromosomal genes in Escherichia coli K-12 using PCR products. Proc Natl Acad Sci USA *97*, 6640-6645.

Davenport, R.J., Wuite, G.J., Landick, R., and Bustamante, C. (2000). Single-molecule study of transcriptional pausing and arrest by E. coli RNA polymerase. Science *287*, 2497-2500.

Deng, S., Stein, R.A., and Higgins, N.P. (2004). Transcription-induced barriers to supercoil diffusion in the Salmonella typhimurium chromosome. Proc Natl Acad Sci USA *101*, 3398-3403.

Deng, S., Stein, R.A., and Higgins, N.P. (2005). Organization of supercoil domains and their reorganization by transcription. Mol Microbiol *57*, 1511-1521.

Drlica, K. (1992). Control of bacterial DNA supercoiling. Mol Microbiol *6*, 425-433.

Drolet, M. (2006). Growth inhibition mediated by excess negative supercoiling: the interplay between transcription elongation, R-loop formation and DNA topology. Mol Microbiol *59*, 723-730.

El Hanafi, D., and Bossi, L. (2000). Activation and silencing of leu-500 promoter by transcription-induced DNA supercoiling in the Salmonella chromosome. Mol Microbiol *37*, 583-594.

Elowitz, M.B., and Leibler, S. (2000). A synthetic oscillatory network of transcriptional regulators. Nature *403*, 335-338.

Elowitz, M.B., Levine, A.J., Siggia, E.D., and Swain, P.S. (2002). Stochastic gene expression in a single cell. Science *297*, 1183-1186.

Epshtein, V., and Nudler, E. (2003). Cooperation between RNA polymerase molecules in transcription elongation. Science *300*, 801-805.

Finn, R.D., Orlova, E.V., Gowen, B., Buck, M., and van Heel, M. (2000). Escherichia coli RNA polymerase core and holoenzyme structures. Embo J *19*, 6833-6844.

Franco, R.J., and Drlica, K. (1988). DNA Gyrase on the Bacterial Chromosome - Oxolinic Acid-Induced DNA Cleavage in the Dnaa-Gyrb Region. J Mol Biol *201*, 229-233.

Golding, I., Paulsson, J., Zawilski, S.M., and Cox, E.C. (2005). Real-time kinetics of gene activity in individual bacteria. Cell *123*, 1025-1036.

Gopal, A., Zhou, Z.H., Knobler, C.M., and Gelbart, W.M. (2012). Visualizing large RNA molecules in solution. Rna *18*, 284-299.

Gore, J., Bryant, Z., Stone, M.D., Nollmann, M., Cozzarelli, N.R., and Bustamante, C. (2006). Mechanochemical analysis of DNA gyrase using rotor bead tracking. Nature *439*, 100-104.

Guptasarma, P. (1996). Cooperative relaxation of supercoils and periodic transcriptional initiation within polymerase batteries. Bioessays *18*, 325-332.

Hardy, C.D., and Cozzarelli, N.R. (2005). A genetic selection for supercoiling mutants of Escherichia coli reveals proteins implicated in chromosome structure. Mol Microbiol *57*, 1636-1652.

Hebenstreit, D. (2013). Are gene loops the cause of transcriptional noise? Trends Genet *29*, 333-338.

Herbert, K.M., La Porta, A., Wong, B.J., Mooney, R.A., Neuman, K.C., Landick, R., and Block, S.M. (2006). Sequence-resolved detection of pausing by single RNA polymerase molecules. Cell *125*, 1083-1094.

Higgins, N.P., and Cozzarelli, N.R. (1982). The binding of gyrase to DNA: analysis by retention by nitrocellulose filters. Nucleic Acids Res *10*, 6833-6847.

Higgins, N.P., Peebles, C.L., Sugino, A., and Cozzarelli, N.R. (1978). Purification of subunits of Escherichia coli DNA gyrase and reconstitution of enzymatic activity. Proc Natl Acad Sci U S A *75*, 1773-1777.

Hocine, S., Raymond, P., Zenklusen, D., Chao, J.A., and Singer, R.H. (2013). Single-molecule analysis of gene expression using two-color RNA labeling in live yeast. Nat Methods *10*, 119-121.

Hodges, C., Bintu, L., Lubkowska, L., Kashlev, M., and Bustamante, C. (2009). Nucleosomal fluctuations govern the transcription dynamics of RNA polymerase II. Science *325*, 626-628.

Kubitschek, H.E. (1990). Cell volume increase in Escherichia coli after shifts to richer media. J Bacteriol *172*, 94-101.

Kussell, E., and Leibler, S. (2005). Phenotypic diversity, population growth, and information in fluctuating environments. Science *309*, 2075-2078.

Landick, R. (2006). The regulatory roles and mechanism of transcriptional pausing. Biochemical Society transactions *34*, 1062-1066.

Larson, D.R., Zenklusen, D., Wu, B., Chao, J.A., and Singer, R.H. (2011). Real-time observation of transcription initiation and elongation on an endogenous yeast gene. Science *332*, 475-478.

Leng, F., Chen, B., and Dunlap, D.D. (2011). Dividing a supercoiled DNA molecule into two independent topological domains. Proc Natl Acad Sci USA *108*, 19973-19978.

Li, G.W., and Xie, X.S. (2011). Central dogma at the single-molecule level in living cells. Nature *475*, 308-315.

Lim, H.M., Lewis, D.E., Lee, H.J., Liu, M., and Adhya, S. (2003). Effect of varying the supercoiling of DNA on transcription and its regulation. Biochemistry *42*, 10718-10725.

Lionberger, T.A., and Meyhofer, E. (2010). Bending the rules of transcriptional repression: tightly looped DNA directly represses T7 RNA polymerase. Biophys J *99*, 1139-1148.

Lionnet, T., Czaplinski, K., Darzacq, X., Shav-Tal, Y., Wells, A.L., Chao, J.A., Park, H.Y., de Turris, V., Lopez-Jones, M., and Singer, R.H. (2011). A transgenic mouse for in vivo detection of endogenous labeled mRNA. Nat Methods *8*, 165-170.

Liu, L.F., and Wang, J.C. (1987). Supercoiling of the DNA template during transcription. Proc Natl Acad Sci USA *84*, 7024-7027.

Lynch, A.S., and Wang, J.C. (1993). Anchoring of DNA to the bacterial cytoplasmic membrane through cotranscriptional synthesis of polypeptides encoding membrane proteins or proteins for export: a mechanism of plasmid hypernegative supercoiling in mutants deficient in DNA topoisomerase I. J Bacteriol *175*, 1645-1655.

Ma, J., Bai, L., and Wang, M.D. (2013). Transcription under torsion. Science *340*, 1580-1583.
Maamar, H., Raj, A., and Dubnau, D. (2007). Noise in gene expression determines cell fate in Bacillus subtilis. Science *317*, 526-529.

Maxwell, A., and Gellert, M. (1984). The DNA Dependence of the Atpase Activity of DNA Gyrase. J Biol Chem *259*, 4472-4480.

Meselson, M. (1972). Formation of hybrid DNA by rotary diffusion during genetic recombination. J Mol Biol *71*, 795-798.

Mitarai, N., Dodd, I.B., Crooks, M.T., and Sneppen, K. (2008). The Generation of Promoter-Mediated Transcriptional Noise in Bacteria. PLoS Comput Biol *4*, e1000109.

Morrison, A., and Cozzarelli, N.R. (1981). Contacts between DNA Gyrase and Its Binding-Site on DNA - Features of Symmetry and Asymmetry Revealed by Protection from Nucleases. Proc Natl Acad Sci USA *78*, 1416-1420.

Mullineaux, C.W., Nenninger, A., Ray, N., and Robinson, C. (2006). Diffusion of green fluorescent protein in three cell environments in Escherichia coli. J Bacteriol *188*, 3442-3448.

Munsky, B., Neuert, G., and van Oudenaarden, A. (2012). Using Gene Expression Noise to Understand Gene Regulation. Science *336*, 183-187.

Muramoto, T., Cannon, D., Gierlinski, M., Corrigan, A., Barton, G.J., and Chubb, J.R. (2012). Live imaging of nascent RNA dynamics reveals distinct types of transcriptional pulse regulation. Proc Natl Acad Sci U S A *109*, 7350-7355.

Nagai, T., Ibata, K., Park, E.S., Kubota, M., Mikoshiba, K., and Miyawaki, A. (2002). A variant of yellow fluorescent protein with fast and efficient maturation for cell-biological applications. Nat Biotechnol *20*, 87-90.

Ozbudak, E.M., Thattai, M., Kurtser, I., Grossman, A.D., and van Oudenaarden, A. (2002). Regulation of noise in the expression of a single gene. Nat Genet *31*, 69-73.

Pato, M.L., Howe, M.M., and Higgins, N.P. (1990). A DNA Gyrase-Binding Site at the Center of the Bacteriophage Mu Genome Is Required for Efficient Replicative Transposition. Proc Natl Acad Sci USA *87*, 8716-8720.

Pedraza, J.M., and Paulsson, J. (2008). Effects of molecular memory and bursting on fluctuations in gene expression. Science *319*, 339-343.

Peter, B.J., Arsuaga, J., Breier, A.M., Khodursky, A.B., Brown, P.O., and Cozzarelli, N.R. (2004). Genomic transcriptional response to loss of chromosomal supercoiling in Escherichia coli. Genome Biol *5*, R87.

Postow, L., Hardy, C.D., Arsuaga, J., and Cozzarelli, N.R. (2004). Topological domain structure of the Escherichia coli chromosome. Gene Dev *18*, 1766-1779.

Raj, A., Peskin, C.S., Tranchina, D., Vargas, D.Y., and Tyagi, S. (2006). Stochastic mRNA synthesis in mammalian cells. PLoS Biol *4*, e309.

Raj, A., Rifkin, S.A., Andersen, E., and van Oudenaarden, A. (2010). Variability in gene expression underlies incomplete penetrance. Nature *463*, 913-918.

Raser, J.M., and O'Shea, E.K. (2004). Control of stochasticity in eukaryotic gene expression. Science *304*, 1811-1814.

Rau, D.C., Gellert, M., Thoma, F., and Maxwell, A. (1987). Structure of the DNA Gyrase DNA Complex as Revealed by Transient Electric Dichroism. J Mol Biol *193*, 555-569.

Reece, R.J., and Maxwell, A. (1991). DNA Gyrase - Structure and Function. Crit Rev Biochem Mol *26*, 335-375.

Revyakin, A., Ebright, R.H., and Strick, T.R. (2004). Promoter unwinding and promoter clearance by RNA polymerase: detection by single-molecule DNA nanomanipulation. Proc Natl Acad Sci USA *101*, 4776-4780.

Revyakin, A., Ebright, R.H., and Strick, T.R. (2005). Single-molecule DNA nanomanipulation: improved resolution through use of shorter DNA fragments. Nat Methods *2*, 127-138.

Rovinskiy, N., Agbleke, A.A., Chesnokova, O., Pang, Z., and Higgins, N.P. (2012). Rates of gyrase supercoiling and transcription elongation control supercoil density in a bacterial chromosome. PLoS Genet *8*, e1002845.

Samul, R., and Leng, F. (2007). Transcription-coupled hypernegative supercoiling of plasmid DNA by T7 RNA polymerase in Escherichia coli topoisomerase I-deficient strains. J Mol Biol *374*, 925-935.

Shi, P.Z., and Qian, H. (2011). A perturbation analysis of rate theory of self-regulating genes and signaling networks. J Chem Phys *134*, 065104.

Shundrovsky, A., Santangelo, T.J., Roberts, J.W., and Wang, M.D. (2004). A single-molecule technique to study sequence-dependent transcription pausing. Biophys J *87*, 3945-3953.

Singh, A., Razooky, B., Cox, C.D., Simpson, M.L., and Weinberger, L.S. (2010). Transcriptional bursting from the HIV-1 promoter is a significant source of stochastic noise in HIV-1 gene expression. Biophys J *98*, L32-34.

Skinner, G.M., Baumann, C.G., Quinn, D.M., Molloy, J.E., and Hoggett, J.G. (2004). Promoter binding, initiation, and elongation by bacteriophage T7 RNA polymerase. A single-molecule view of the transcription cycle. J Biol Chem *279*, 3239-3244.

Snyder, M., and Drlica, K. (1979). DNA Gyrase on the Bacterial Chromosome - DNA Cleavage Induced by Oxolinic Acid. J Mol Biol *131*, 287-302.

So, L.H., Ghosh, A., Zong, C., Sepulveda, L.A., Segev, R., and Golding, I. (2011). General properties of transcriptional time series in Escherichia coli. Nat Genet *43*, 554-560.

Sousa, R., Chung, Y.J., Rose, J.P., and Wang, B.C. (1993). Crystal-Structure of Bacteriophage-T7 Rna-Polymerase at 3.3-Angstrom Resolution. Nature *364*, 593-599.

Stark, H., Mueller, F., Orlova, E.V., Schatz, M., Dube, P., Erdemir, T., Zemlin, F., Brimacombe, R., and Vanheel, M. (1995). The 70s Escherichia-Coli Ribosome at 23 Angstrom Resolution - Fitting the Ribosomal-Rna. Structure *3*, 815-821.

Suter, D.M., Molina, N., Gatfield, D., Schneider, K., Schibler, U., and Naef, F. (2011). Mammalian genes are transcribed with widely different bursting kinetics. Science *332*, 472-474.

Taniguchi, Y., Choi, P.J., Li, G.W., Chen, H., Babu, M., Hearn, J., Emili, A., and Xie, X.S. (2010). Quantifying E. coli proteome and transcriptome with single-molecule sensitivity in single cells. Science *329*, 533-538.

Telesnitsky, A., and Chamberlin, M.J. (1989). Terminator-distal sequences determine the in vitro efficiency of the early terminators of bacteriophages T3 and T7. Biochemistry *28*, 5210-5218.

ten Heggeler-Bordier, B., Wahli, W., Adrian, M., Stasiak, A., and Dubochet, J. (1992). The apical localization of transcribing RNA polymerases on supercoiled DNA prevents their rotation around the template. Embo J *11*, 667-672.

Thattai, M., and van Oudenaarden, A. (2004). Stochastic gene expression in fluctuating environments. Genetics *167*, 523-530.

Tsao, Y.P., Wu, H.Y., and Liu, L.F. (1989). Transcription-driven supercoiling of DNA: direct biochemical evidence from in vitro studies. Cell *56*, 111-118.

Wang, W., Li, G.W., Chen, C., Xie, X.S., and Zhuang, X. (2011). Chromosome organization by a nucleoid-associated protein in live bacteria. Science *333*, 1445-1449.

Weixlbaumer, A., Leon, K., Landick, R., and Darst, S.A. (2013). Structural basis of transcriptional pausing in bacteria. Cell *152*, 431-441.

Wolf, D.M., Vazirani, V.V., and Arkin, A.P. (2005). Diversity in times of adversity: probabilistic strategies in microbial survival games. J Theor Biol *234*, 227-253.

Wu, H.Y., Shyy, S.H., Wang, J.C., and Liu, L.F. (1988). Transcription generates positively and negatively supercoiled domains in the template. Cell *53*, 433-440.

Xu, L., Chen, H., Hu, X.H., Zhang, R.M., Zhang, Z., and Luo, Z.W. (2006). Average gene length is highly conserved in prokaryotes and eukaryotes and diverges only between the two kingdoms. Mol Biol Evol *23*, 1107-1108.

Yoffe, A.M., Prinsen, P., Gopal, A., Knobler, C.M., Gelbart, W.M., and Ben-Shaul, A. (2008). Predicting the sizes of large RNA molecules. Proc Natl Acad Sci U S A *105*, 16153-16158.

Zong, C., So, L.H., Sepulveda, L.A., Skinner, S.O., and Golding, I. (2010). Lysogen stability is determined by the frequency of activity bursts from the fate-determining gene. Mol Syst Biol *6*, 440.

List of Figures